Shining Light on Interstellar Matter

A laboratory study

Daniel Paardekooper

Shining Light on Interstellar Matter, A laboratory study, Thesis, Leiden University.

130 pages; illustrated, with bibliographic references and summary in Dutch.

ISBN/EAN: 978-94-028-0233-7

Printed by Ipskamp Drukkers.

Cover design by Daan Boltje, image of The Horsehead Nebula from José Jimenez Priego.

This work has been financially supported by the Nederlandse Organisatie voor Wetenschappelijk Onderzoek.

Shining Light on Interstellar Matter

A laboratory study

Proefschrift

ter verkrijging van
de graad van doctor aan de Universiteit Leiden
op gezag van de Rector Magnificus prof. mr. C. J. J. M. Stolker,
volgens besluit van het College voor Promoties
te verdedigen op dinsdag 5 Juli 2016
klokke 16.15 uur

door

Daniël Mathijs Paardekooper
geboren te Schiedam
in 1986

Promotiecommissie

Promotor	Prof. dr. H. V. J. Linnartz	
Overige leden	Prof. dr. H. J. A. Röttgering	
	Prof. dr. A. G. G. M. Tielens	
	Prof. dr. W. A. Brown	Sussex University
	Dr. M. S. Gudipati	NASA's Jet Propulsion Laboratory
	Dr. S. Ioppolo	The Open University, Milton Keynes

CONTENTS

1

INTRODUCTION

The conditions in the space between the stars, the so-called interstellar medium (ISM), vary strongly from the conditions we are familiar with on the planet Earth. Temperatures range from 10^6 down to 10 K, while densities can range from 10^{-4} up to 10^8 particles cm^{-3} (van Dishoeck, 2014). Compare these conditions to an exceptional summer day in the Netherlands at sea level with a temperature of 20° (293 K) and density of $2.7x10^{19}$ particles cm^{-3}! The density in the ISM is *eleven* to *twenty-three* orders of magnitude lower. On Earth, the high density and temperature stimulate chemical reactions; reaction barriers can be overcome and excess reaction energy is removed by surrounding particles acting as a third body. In the ISM however, due to the low density the probability of two species colliding is small. The probability of species reacting is even more unlikely, since usually no third body is present to remove the excess reaction energy. Therefore, the chemical network in the gas phase is mainly driven by (exothermic) ion-molecule reactions. Next to these extreme physical conditions, cosmic rays are continuously penetrating the ISM that is also affected by the interstellar radiation field containing high energy photons (Tielens, 2005). Both of these are capable of effectively ionising or fragmentating species. Considering the harsh environment described above, the molecular complexity actually found in the ISM is astonishing. Up to date, over 185 different species (not including isotopes) have been detected in interstellar and circumstellar environments.[1]

The ISM consists of 99% of gas and 1% of dust, with an inhomogenous distribution of the mass. The gas consists of hydrogen (89%), helium (9%) and heavier elements (2%). Gas and dust gather in molecular clouds in the ISM, and within these clouds, dense and diffuse regions exist with number densities of $10^4 - 10^5$ cm^{-3} and 10^2 cm^{-3}, respectively (van Dishoeck et al., 2013). Typical temperatures in dense regions range from 10 to 20 K. Visible light is unable to penetrate these regions, which are therefore referred to as 'dark clouds'. The dense regions are fed from diffuse regions upon gravitational attractions or external shocks (Shu et al., 1987). Photons from the interstellar radiation field can penetrate the diffuse regions, leading to the photodestruction of species present. In the dense regions of the molecular clouds, photons are absorbed by the edges, effectively protecting the inner parts of the clouds. When the density in these molecular clouds reaches a critical point, the cloud can gravitationally collapse and a star can form. Conservation of momentum leads to a disk surrounding the star, in which planets are thought to be formed (Armitage, 2011).

It has become clear that the dust present in the molecular clouds plays an essential role in the cosmochemical evolution from diffuse clouds to planets and stars, since gas phase chemistry only cannot explain the observed abundance of species. The cold (10 to 20 K) dust grains, with a typical dimension of up to 0.1 μm in size acts as a small cryostat. Atoms and molecules collide and stick, over time an ice can be formed. It provides a meeting place, where atoms and molecules can accrete, meet and react. The grain and ice act as a third body, effectively facilitating chemical reactions. The accretion of species depends on the gas composition, carbon is locked in CO and oxygen atoms are present. Hydrogen is abundant and on top of the grain still mobile at these temperatures. CO and oxygen atoms, undergo several hydrogenation reactions forming CH_3OH and H_2O, respectively.

1 https://www.astro.uni-koeln.de/cdms/molecules

For many ice components, only efficient surface formation routes are known (Linnartz et al., 2015). Inside dark clouds, the dust grains act as molecular reservoirs, which are continuously energetically processed by an internal radiation field driven by the interaction of penetrating cosmic rays with molecular hydrogen (H_2). This processing can leads to an increase of molecular complexity, resulting in the formation of so-called Complex Organic Molecules (COMs).

As mentioned before, shortly after a star is formed, the conservation of momentum results in a disk surrounding the star. This protoplanetary disk consists of the remnants of the molecular cloud, including the (icy) dust grains. Planets like Earth are thought to form in these disks. It has been hypothesised that water and prebiotic species in this stage can be delivered to planets by cometary bodies, hereby effectively kickstarting life. Therefore, it is key to understand the fundamental processes occurring in interstellar ices and into what degree of molecular complexity this can result. This is the topic of the present thesis.

1.1 ICE COMPOSITION

Infrared (IR) observations from the ground are limited to spectral windows, due to obscuring effects of the Earth's atmosphere. This has posed the requirement of space based observations to derive the composition of interstellar ice. These observations have been mainly performed using the Interstellar Space Observatory (ISO) and the Spitzer Space Telescope (SST) (Gibb et al., 2000; Boogert et al., 2004, 2008). Figure 1.1 presents spectra of line of sight infrared observations from different protostars towards background stars. Via these observations the main composition of interstellar ices has been obtained. These mainly consist of H_2O, CO, CO_2, CH_4, CH_3OH, H_2CO, HCOOH and NH_3. Also other constituents like OCN^- and $NH_4{}^+$ have been detected. Both telescopes (ISO and SST) have become inactive after running out of helium, and currently there is no space based telescope active in the IR range. Late 2018, the James Webb Space Telescope (JWST) will be launched and will have IR-spectroscopic instruments to perform observations of interstellar ices with unprecedented sensitivity and spatial resolution.

Most components of these ices can be explained by non-energetic atom addition processes (Tielens & Hagen, 1982; Linnartz et al., 2015), while the presence of OCN^- is an indication that interstellar ice undergoes energetic processing (Bernstein et al., 1995; Palumbo et al., 2000). The interaction of penetrating cosmic rays with matter can in turn produce secondary particles, such as VUV photons (Prasad & Tarafdar, 1983; Shen et al., 2004), electrons and low-energy cosmic rays. The secondary particles are capable of energetically processing the ice, which can lead to an increase of molecular complexity. Next to these effects, the temperature increase in different stages of the star formation sequence can facilitate thermal reactions in interstellar ice (Theulé et al., 2013).

Direct IR observational evidence for molecular complexity is however lacking. Ice spectra are dominated by the abundant ice components; weak features of minor ice components are bound to overlap since the cold environment results in line broadening. Additionally, the abundance of these species is low, since it decreases with increasing molecular complexity. However, in later stages during the star formation sequence, the temperature of the grains increases. This leads to the thermal desorption of (volatile) species present in the ice, after which they can then be observed in gas phase. Moreover, icy bodies may impact on planets delivering H_2O and COMs.

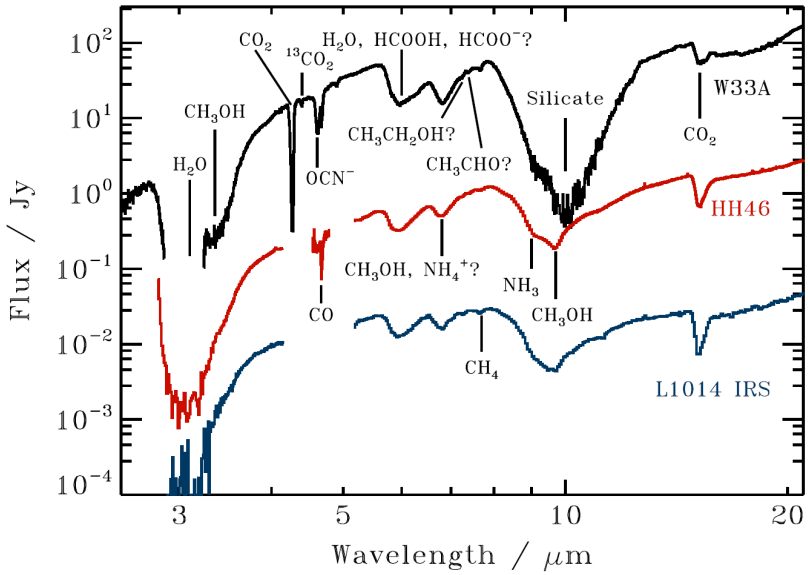

Figure 1.1: Ice spectra toward the protostars W334A ($10^5 L_\odot$), HH46 ($12 L_\odot$), and L1014 IRS ($0.09 L_\odot$) (Gibb et al., 2000; Boogert et al., 2004, 2008). The 3 μm portions of the spectra have been binned to increase the signal-to-noise ratio. Figure from Öberg et al. (2011).

Cometary bodies contain a wealth of information, they preserve the earliest record of material about dust grains and ice, from the molecular cloud out of which our Sun and Earth have been formed. Recently, after a 10 year journey Rosetta has visited the comet 67P/Churyumov-Gerasimenko. Rossetta's lander Philea has achieved the first-ever landing on a comet. Philea detected organic compounds (Goesmann et al., 2015), of which some can play an important role in the prebiotic synthesis of amino acids, sugars and ribonucleic acid (RNA). Interstellar ice cannot directly be compared to cometary ice, but this detection does support the presented hypothesis about the origin of life on Earth, i.e., that COMs were delivered from space.

1.2 ICE EVOLUTION THROUGH DIFFERENT STAGES OF STAR FORMATION

In the cartoon presented in figure 1.2 (Herbst & van Dishoeck, 2009), the evolution of ice through different stages of star formation is depicted. During the precollapse stage (dense regions, dark cloud), the continuous hydrogenation of oxygen atoms on the surface leads to a water rich layer. With increasing density ($10^4 - 10^5$ cm^{-3}), CO starts freezing out. The hydrogenation of CO leads to the formation of CH_3OH (Hiraoka et al., 2002; Watanabe & Kouchi, 2002; Fuchs et al., 2009). Cosmic rays interacting with matter, produce secondary particles such as electrons, low energy cosmic rays and VUV photons. These secondary particles can induce (photo)desorption or bond cleavages of ice species. Desorption effectively influences the molecular reservoirs in the gas and solid phase while highly reactive radicals can recombine reforming the original species, or move around the ice to eventually meet a different reaction partner (Öberg et al., 2009). This can result in an increase of molecular complexity, forming COMs. During the core collapse, the temperature increases and volatile species will move from the grains into the gas phase.

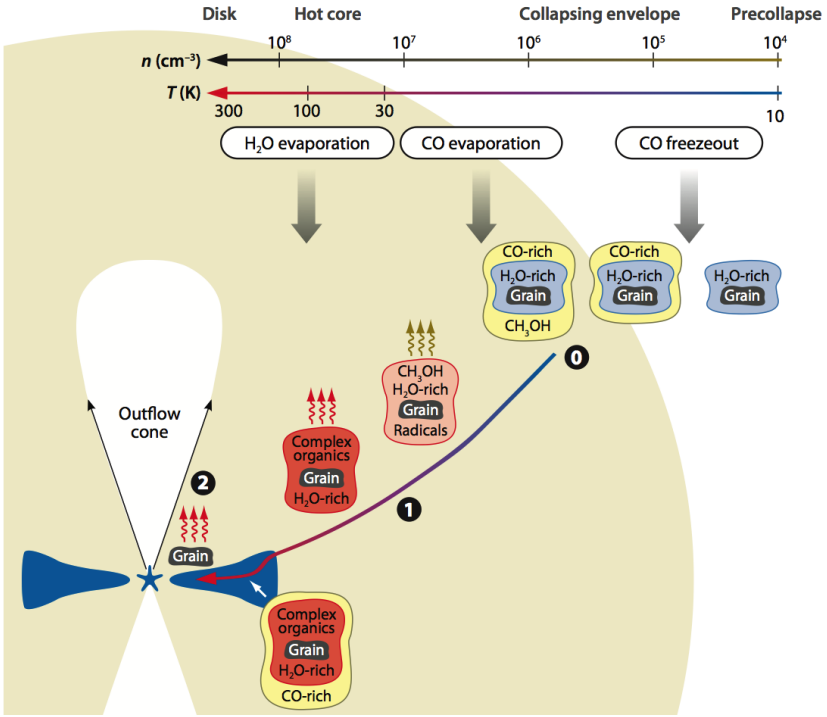

Figure 1.2: Cartoon representation of the evolution of material from the prestellar core stage through the collapsing envelope into a protoplanetary disk. The dust grains are typically 0.1 µm and are not drawn to scale. Figure by E.F. van Dishoeck and R. Visser. Figure from Herbst & van Dishoeck (2009).

Apart from directly detecting species through IR obervations in the ice, it is also possible to indirectly detect gas phase species which have been evaporated from the dust grains. A large variety of complex organic molecules have been detected in the gas phase in a number of astronomical environments (see Fig. 1.3, Jørgensen et al., 2012). Gas phase chemistry fails to explain the observed abundances while astrochemical models indicate that the majority of complex organic species must have its origin in the solid state, i.e., on icy surfaces (Garrod & Herbst, 2006; Garrod et al., 2008; Balucani et al., 2015).

Recent results from the Atacama Large Millimeter/submillimeter Array (ALMA) have shown the presence of the simplest sugar glycolaldehyde in the protostars IRAS 16293A and B (Jørgensen et al., 2012). The detected glycolaldehyde is thought to form on top of dust grains either by photochemistry of solid methanol (see Öberg et al. (2009) and Chapter 5) or by surface hydrogenation of CO (Fedoseev et al., 2015; Chuang et al., 2016). Glycolaldehyde is an ingredient for the chemical reactions that can create ribonucleic acid (RNA), a molecule which is essential for all known forms of life. The position where these molecules have been found is located near the position where planets are thought to form (Jørgensen et al., 2012).

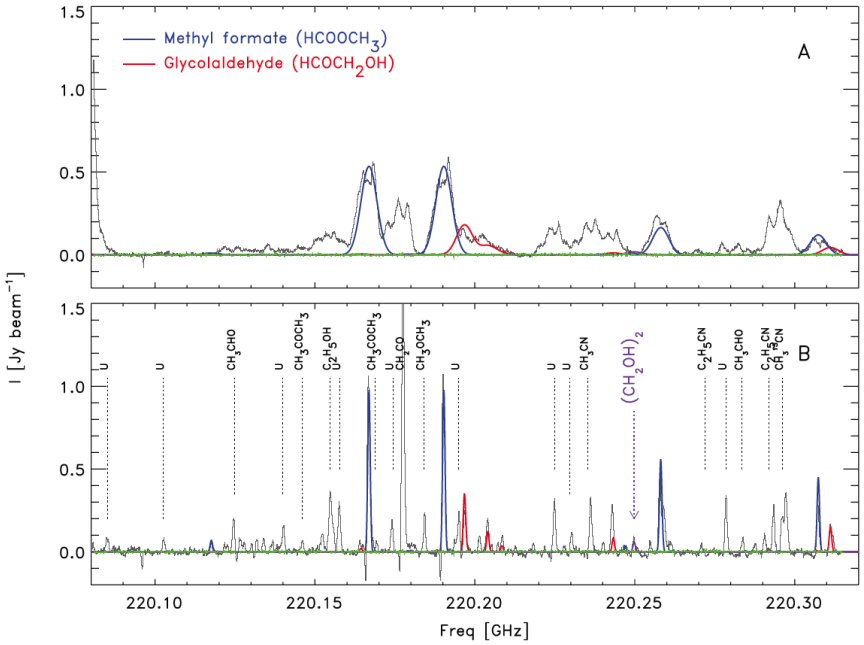

Figure 1.3: Spectra in the central beams toward the continuum peaks of IRAS16293A (upper) and IRAS16293B (lower). The X-axis represents the frequencies in the rest frame of the system. Note the much narrower lines toward IRAS16293B which facilitate identification of individual feature. Figure from Jørgensen et al. (2012).

1.3 LABORATORY ASTROCHEMISTRY

Solid state laboratory experiments aim at increasing our understanding of the fundamental processes occurring in ices, containing molecules of astrochemical interest. Over the years a large variety of experimental techniques and detection schemes have been developed and applied. It started with fundamental studies using IR spectroscopy[2] in a high vacuum (10^{-7} mbar) environment (Hudgins et al., 1993). This has led to the detection of molecules condensed on top of small dust grains in molecular clouds (see Fig. 1.1). Since the main constituent of interstellar ices is now known, pure ices containing these molecules have been processed using vacuum ultraviolet (VUV) photons produced by a hydrogen microwave discharge lamp (Gerakines et al., 1996), resembling the radiation field in such environments.

In a later stage, an interstellar ice mixture of H_2O:CH_3OH:NH_3:CO:CO_2 (2:1:1:1:1) has been irradiated for 24 hour using a hydrogen microwave discharge lamp (Muñoz Caro et al., 2002). This has been performed at 12 K in a high vacuum environment. The sample was warmed to room temperature and the residuals have been analysed using a gas chromatograph mass spectrometer (GC-MS). This was the first *ex situ* detection of the formation of amino acids from photoprocessing such an interstellar ice mixture, demonstrating that under these conditions prebiotic species can be formed from energetically processing the basic interstellar ice ingredients (Fig. 1.4). It remains however unclear if these molecules have been formed at low temperature or during a later stage in the analysis. Technological

2 http://home.strw.leidenuniv.nl/ linnartz/leiden-ice-database.html

improvements have provided more details about the residual (de Marcellus et al., 2015). Recent efforts have been made in order to improve on such techniques by performing the analysis *in situ* (Mrad et al., 2016), minimizing possible chemical alternations during the analysis. All these methods, however, need the heating of the ice sample and thermal effects cannot be fully excluded.

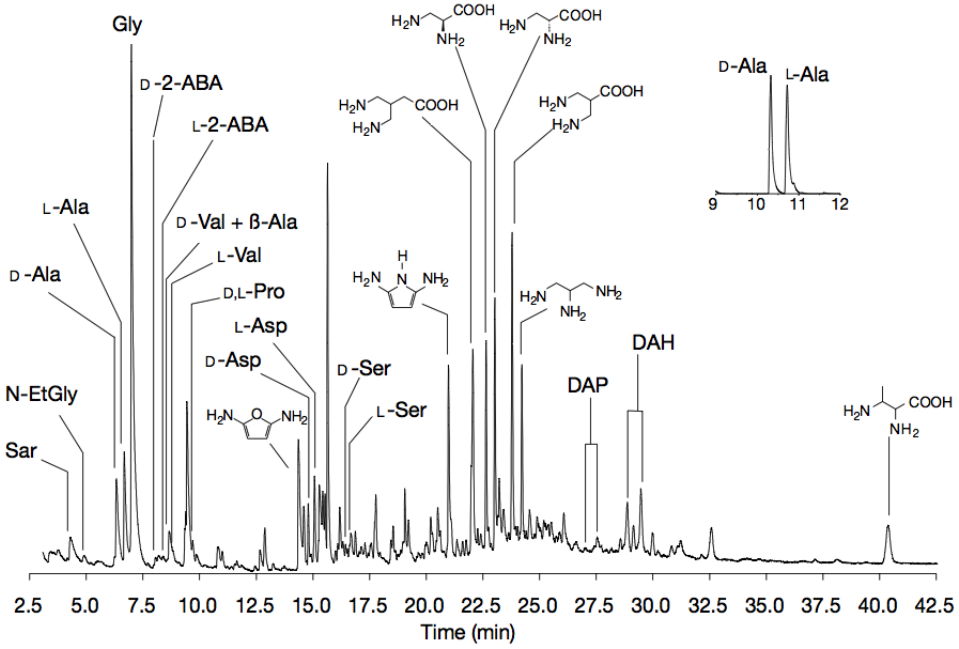

Figure 1.4: Mass spectrum recorded by GC of a VUV photoprocessed interstellar ice analogue. Figure from Muñoz Caro et al. (2002).

In the ISM in dense cores, at low temperatures the dust grains are covered with an ice mantle consisting primarily of H_2O. A typical 0.1 µm sized dust grain is surrounded by about 100 monolayers of water ice (1 ML = 10^{15} molecules/cm^2) (van Dishoeck, 2014). Combined with the importance of surface reactions, this has posed requirements on the vacuum conditions of solid state laboratory experiments simulating these environments. In a high vacuum (10^{-7} mbar) environment, every 25 seconds a cold substrate will be coated with a ML, while in an UltraHigh Vacuum (UHV) environment (10^{-10} mbar) this will require almost 7 hours. This has substantially improved the experimental conditions for which interstellar ices can be studied. *In situ* diagnostics such as InfraRed (IR) spectroscopy (reflection or transmission) are used in conjunction with Quadruple Mass Spectrometry (QMS) and Temperature Programmed Desorption (TPD). Although powerful and versatile, both methods come with disadvantages. Only molecules with a dipole moment can be monitored using IR spectroscopy. It traces functional groups, and can suffer from overlapping bands. TPD can accommodate thermal reactions during the warm up phase, which can result in chemical changes in the ice (Öberg, 2009; Ioppolo, 2010).

Recently, Jones & Kaiser (2013) have implemented a different detection scheme. After processing an ice at low temperature, the sample is slowly warmed to high temperature by performing a TPD. Species will sublimate, and the gas phase species desorbing from the ice are ionised using Single Photon Ionisation (SPI, 10.49 eV). Subsequent detection

is performed using a time-of-flight mass spectrometer. Since the energy of the photon is chosen slightly above the ionisation potential of the species, this mainly leads to ionisation without fragmentation. An update of the system allows to distinguish between isomers by using tunable SPI (Abplanalp et al., 2016).

So far, the composition of ice is measured either by *in situ* IR spectroscopy, or by detecting the species moving into the gas phase using either QMS or SPI ReTOF. The next step forward is inducing desorption using alternative methods. Using an IR laser pulse (~ 3 μm), Gudipati & Yang (2012) and Henderson & Gudipati (2015) induce desorption, transferring species from an ice into the gas phase. Species are ionised using a focused UV laser, and detected by time-of-flight mass spectrometry.

In the Sackler Laboratory for Astrophysics in Leiden an experimental setup has been developed, aiming at measuring the composition of ices; MATRI^{2}CES (Mass-Analytical Tool for Reactions in Interstellar ICES, Fig. 1.5). Desorption of the ice is induced using an unfocused UV laser. Gas phase species are subsequently ionised using electrons with a mean energy of 70 eV, after which the ions are extracted and measured by time-of-flight mass spectrometry (Paardekooper et al., 2014; Bossa et al., 2015). The ice can be photo-processed using a hydrogen discharge lamp; at different fluences the ice constituents can be tracked. It has an improved sensitivity compared to IR spectroscopy, and compared to TPD/QMS the advantage that all ice constituents can be desorbed and traced *at low temperature*.

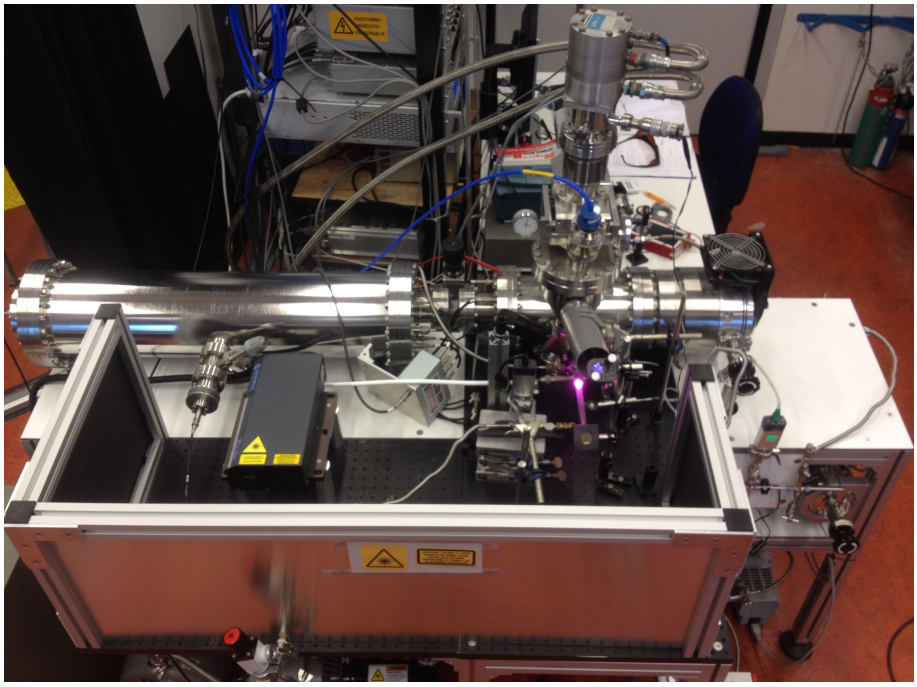

Figure 1.5: Picture of MATRI^{2}CES, the system is described in detail in Paardekooper et al. (2014) and Chapter 2.

1.4 THIS THESIS

This thesis is dedicated to studying the interaction of photons with matter of astrochemical interest. For the field of astrochemistry, a new *in situ* experimental technique, Laser Desorption Post-Ionization Time-Of-Flight Mass spectrometry (LDPI TOF-MS) is applied to study the photochemistry in ice (Chapter 2, 4 and 5) containing molecules of astrochemical interest. Apart from the chemistry occurring upon absorption of photons and photodissociation, photons can induce desorption of molecules in ice, so called photodesorption. We have applied a novel approach to accurately derive the photodesorption rate (Chapter 6) for CO ice. Since light plays an essential role throughout the different chapters of this thesis, a chapter has been dedicated to characterize a commonly used light source in laboratory astrochemistry, the hydrogen microwave discharge lamp (Chapter 3). As molecular complexity is the leading topic in this thesis, the last chapter focusses on the influence of light on a large Poly Aromatic Hydrocarbon (PAH). The data are recorded with a different setup, also using TOF methodology. The photo-fragmentation of the hexa-benzo-coronene (HBC) cation, a large PAH cation of potential astrophysical interest is presented in Chapter 7.

Chapter 2 introduces a new experimental technique to study the formation of complex organic molecules (COMs) in (interstellar) ice analogous. Species of astrophysical interest are deposited on top of a cold substrate (20 K) and subsequently photo-processed using a hydrogen microwave discharge lamp. The composition of the ice is traced using LDPI TOF-MS. Briefly, desorption is induced using a laser pulse, species in the desorption plume are then ionised using electrons, after which they are extracted into a field-free time-of-flight tube. Subsequent detection of the ions is realised using a Multi Channel Plate (MCP) detector. Based on their time of arrival, the m/z is determined. Detailed description and calibration of the system are provided, and the system capabilities are demonstrated on the example of photo-processed methane (CH_4) ice at 20 K.

Chapter 3 describes the spectral characterisation of the hydrogen microwave discharge lamp, commonly used to simulate interstellar radiation fields in laboratory experiments. Recent discrepancies between identical measurements in different laboratories, as well as clear wavelength dependent results obtained in monochromatic (synchrotron) experiments, hint at a more elaborate dependence on the exact discharge settings than assumed so far. A sophisticated plasma lamp calibration set-up has been used to record the vacuum ultraviolet (VUV) emission spectra. Spectra are compared with the output of a calibrated D_2 -lamp which allows a derivation of absolute radiance. The direct influence of using two lamp spectra on the CO photodepletion rate is presented.

Chapter 4 presents the ice photochemistry of pure methane (CH_4), studied at 20 K. VUV processing is performed using photons produced by a hydrogen microwave discharge lamp. LDPI TOF-MS is used for the first time to determine branching ratios of primary reactions leading to CH_3, CH_2, and CH radicals, typically for fluences as expected in space. The study is based on a stable end-products analysis and the mass spectra are interpreted using an appropriate set of coupled reactions and rate constants, yielding clear differences compared to previous gas phase studies. The matrix environment as well as the higher efficiency of reverse reactions in the ice favor CH_3 radical formation as the main first generation photoproduct.

Chapter 5 describes a study of the photoprocessing of pure methanol (CH_3OH) ice at 20 K. Condensed methanol is observed in molecular clouds. Its solid formation route is

well studied in the laboratory through subsequent hydrogenation events of CO. In the past, the ice photochemistry of methanol has been studied with various techniques, it is a known precursor for the formation of various COMs. Using LDPI TOF-MS, we study the formation of COMs as function of VUV fluence, and for the first time the formation of $(CO)_3H_x$ species is detected *in situ* after the VUV photoprocessing of methanol ice.

Chapter 6 presents a novel approach to study the photodesorption rate of molecules of astrochemical interest, on the example of CO ice. Complete desorption of the ice is induced using a laser pulse. The desorption profile is sampled at different extraction times relative to the laser pulse. Using this approach we track the composition and surface coverages of species of the ice as function of VUV fluence. Accurate surface coverages and flux calibration have been performed using HeNe interferometry and *in situ* NIST photodiode measurements.

Chapter 7 describes a study of the photo-fragmentation of the hexa-peri-hexabenzocoronene HBC cation -$C_{42}H_{18}{}^+$ - a large PAH cation of potential astrophysical interest. HBC cation photo-fragment patterns are measured upon irradiation by an unfocused Nd:YAG laser (532 nm) for different experimental conditions, using quadrupole ion trap, time- of-flight mass spectrometry. Both stepwise dehydrogenation of $C_{42}H_{18}{}^+$ and C_2/C_2H_2 loss pathways are identified as relevant photodissociation routes. Whereas the majority of the experiments presented focuses onto COM formation in bottom-up approaches, the research presented here follow an opposite route, namely top-down, starting from large complex precursor species.

BIBLIOGRAPHY

Abplanalp, M. J., Förstel, M., & Kaiser, R. I. 2016, Chem. Phys. Lett., 644, 79
Armitage, P. J. 2011, Ann. Rev. Astron. Astrophys., 49, 195
Balucani, N., Ceccarelli, C., & Taquet, V. 2015, Mon. Not. R. Astron. Soc., 449, L16
Bernstein, M. P., Sandford, S. A., Allamandola, L. J., Chang, S., & Scharberg, M. A. 1995, Astrophys. J., 454, 327
Boogert, A. C. A., Pontoppidan, K. M., Knez, C., et al. 2008, Astrophys. J., 678, 985
Boogert, A. C. A., Pontoppidan, K. M., Lahuis, F., et al. 2004, Astrophys. J. Suppl. Ser., 154, 359
Bossa, J.-B., Paardekooper, D. M., Isokoski, K., & Linnartz, H. 2015, Phys. Chem. Chem. Phys., 17, 17346
Chuang, K.-J., Fedoseev, G., Ioppolo, S., van Dishoeck, E. F., & Linnartz, H. 2016, Mon. Not. R. Astron. Soc., 455, 1702
de Marcellus, P., Meinert, C., Myrgorodska, I., et al. 2015, Proc. Natl. Acad. Sci., 112, 965
Fedoseev, G., Cuppen, H. M., Ioppolo, S., Lamberts, T., & Linnartz, H. 2015, Mon. Not. R. Astron. Soc., 448, 1288
Fuchs, G. W., Cuppen, H. M., Ioppolo, S., et al. 2009, Astron. Astrophys., 505, 629
Garrod, R. T. & Herbst, E. 2006, Astron. Astrophys., 457, 927
Garrod, R. T., Weaver, S. L. W., & Herbst, E. 2008, Astrophys. J., 682, 283
Gerakines, P. A., Schutte, W. A., & Ehrenfreund, P. 1996, Astron. Astrophys., 312, 289
Gibb, E., Nummelin, A., Irvine, W. M., Whittet, D. C. B., & Bergman, P. 2000, Astrophys. J., 545, 309
Goesmann, F., Rosenbauer, H., Bredehöft, J. H., et al. 2015, Science, 349
Gudipati, M. S. & Yang, R. 2012, Astrophys. J. Lett., 756, L24
Henderson, B. L. & Gudipati, M. S. 2015, Astrophys. J., 800, 66
Herbst, E. & van Dishoeck, E. F. 2009, Ann. Rev. Astron. Astrophys., 47, 427
Hiraoka, K., Sato, T., Sato, S., et al. 2002, Astrophys. J., 577, 265
Hudgins, D. M., Sandford, S. A., Allamandola, L. J., & Tielens, A. G. G. M. 1993, Astrophys. J. Suppl. Ser., 86, 713
Ioppolo, S. 2010, PhD thesis, University of Leiden
Jones, B. M. & Kaiser, R. I. 2013, J. Phys. Chem. Lett., 4, 1965
Jørgensen, J. K., Favre, C., Bisschop, S. E., et al. 2012, Astrophys. J. Lett., 757, L4
Linnartz, H., Ioppolo, S., & Fedoseev, G. 2015, Int. Rev. Phys. Chem., 34, 205
Mrad, N. A., Duvernay, F., Chiavassa, T., & Danger, G. 2016, Mon. Not. R. Astron. Soc., DOI: 10.1093/mnras/stw346
Muñoz Caro, G. M., Meierhenrich, U. J., Schutte, W. A., et al. 2002, Nature, 416, 403
Öberg, K. I. 2009, PhD thesis, University of Leiden
Öberg, K. I., Boogert, A. C. A., Pontoppidan, K. M., et al. 2011, Astrophys. J., 740, 109
Öberg, K. I., Garrod, R. T., van Dishoeck, E. F., & Linnartz, H. 2009, Astron. Astrophys., 504, 891
Paardekooper, D. M., Bossa, J.-B., Isokoski, K., & Linnartz, H. 2014, Rev. Sci. Instrum., 85, 104501
Palumbo, M. E., Pendleton, Y. J., & Strazzulla, G. 2000, Astrophys. J., 542, 890
Prasad, S. S. & Tarafdar, S. P. 1983, Astrophys. J., 267, 603
Shen, C. J., Greenberg, J. M., Schutte, W. A., & van Dishoeck, E. F. 2004, Astron. Astrophys., 415, 203
Shu, F. H., Adams, F. C., & Lizano, S. 1987, Ann. Rev. Astron. Astrophys., 25, 23
Theulé, P., Duvernay, F., Danger, G., et al. 2013, Adv. Space Res., 52, 1567
Tielens, A. G. G. M. 2005, The Physics and Chemistry of the Interstellar Medium (Cambridge University Press)
Tielens, A. G. G. M. & Hagen, W. 1982, Astron. Astrophys., 114, 245
van Dishoeck, E. F. 2014, Farad. Discuss., 168, 9
van Dishoeck, E. F., Herbst, E., & Neufeld, D. A. 2013, Chem. Rev., 113, 9043
Watanabe, N. & Kouchi, A. 2002, Astrophys. J., 567, 651

2

LASER DESORPTION TIME-OF-FLIGHT MASS SPECTROMETRY OF VUV PHOTO-PROCESSED ICES

A new ultra-high vacuum experiment is described that allows studying photo-induced chemical processes in interstellar ice analogues. MATRI^{2}CES - a Mass Analytical Tool to study Reactions in Interstellar ICES - applies a new concept by combining laser desorption and time-of-flight mass spectrometry with the ultimate goal to characterize *in situ* and in real time the solid state evolution of organic compounds upon UV photolysis for astronomically relevant ice mixtures and temperatures. The performance of the experimental setup is demonstrated by the kinetic analysis of the different photoproducts of pure methane (CH_4) ice at 20 K. A quantitative approach provides formation yields of several new species with up to four carbon atoms. Convincing evidence is found for the formation of even larger species. Typical mass resolutions obtained range from $M/\Delta M \sim 320$ to ~ 400 for CH_4 and Argon, respectively. Additional tests show that the typical detection limit (in monolayers) is $\leqslant 0.02$ ML, substantially more sensitive than the regular techniques used to investigate chemical processes in interstellar ices.

D. M. Paardekooper, J.-B. Bossa, K. Isokoski and H. Linnartz, *Laser desorption time-of-flight mass spectrometry of ultraviolet photo-processed ices*, Rev. Sci. Instrum., 85, (2014) 104501.

2.1 INTRODUCTION

The astronomical flagship facility ALMA (Atacama Large Millimeter/sub-millimeter Array) has started to produce data with a spectral and spatial resolution that is setting new standards. It is expected that the large number of molecules - ions, radicals, small and complex species - already observed in the ISCM (inter- and circumstellar medium) - 180 so far - will increase rapidly. This further highlights the rich chemistry occurring in star and planet forming regions. However, detailed knowledge of the exact formation pathways of many of the observed species is limited. Decades of astronomical observations, laboratory studies and astrochemical modelling point towards a complex interplay between the gas phase and the solid state (Herbst & van Dishoeck, 2009). Particularly, many of the saturated species - for example, dimethyl ether or glycolaldehyde, but also water - are expected to form on icy dust grains, as present in dark interstellar clouds, upon thermal processing, vacuum UV irradiation, atom bombardment, or interaction with cosmic rays or free electrons (Garrod & Herbst, 2006; Öberg et al., 2009). Whereas gas phase reactions of astronomical interest have been simulated under fully controlled experimental conditions for decades, this is not the case for reactions taking place in interstellar ice analogues, where separate solid state reactions can be studied in the laboratory roughly since 2000. On the contrary, since tens of years it is known that complex organic material, including amino acids, forms from energetically processing of bulk ices composed of astrochemical relevant constituents upon ultraviolet irradiation (Muñoz Caro et al., 2002; Bernstein et al., 2002; Briggs et al., 1992; Nuevo et al., 2006, 2007; Elsila et al., 2007; Nuevo et al., 2008; Chen et al., 2008; de Marcellus et al., 2011) and proton irradiation (Kobayashi et al., 1995; Hudson et al., 2008), but the physical-chemical processes at play are not well understood. Moreover, the interpretation of this data is difficult, since the measurements were performed *ex situ*; residues were heated and exposed to air before analysis in a gas chromatograph became possible. More recently, *in situ* analysis of energetically processed ices have focused on the formation of the smallest amino acid glycine (Lafosse et al., 2006; Holtom et al., 2005; Bossa et al., 2009). In order to fully understand the complex solid-state astrochemical network responsible for molecular complexity in space, dedicated *in situ* laboratory experiments are needed, and this is the topic of the present paper (see also Linnartz et al., 2011, for a recent overview).

The traditionally used analytical methods in solid-state laboratory astrophysics are Fourier Transform InfraRed (FTIR) spectroscopy and Temperature Programmed Desorption (TPD) combined with Quadrupole Mass Spectrometry (QMS). Although sensitive, these techniques are inherently prone to uncertainty. Infrared reflection (RAIRS) or transmission spectroscopy enables remote analysis of the sample composition without chemical alteration. However, depending on the specific ice mixture at hand and the absorption band strength of its constituents the detection limit is $\sim 1\%$. Molecules without a dipole moment will stay concealed, since they lack IR active modes (e.g., N_2 and O_2). For species with IR active modes, even a qualitative interpretation of the acquired spectra can be limited, due to spectral overlap, specifically as with increasing level of complexity the number of vibrational modes increases (Öberg et al., 2009). TPD combined with QMS is more sensitive than FTIR, but comes inherently with the destruction of the ice. Moreover, the increase in temperature may induce thermally activated reactions (Theulé et al., 2013) and can change ice morphology (Isokoski, 2013; Isokoski et al., 2014). For these reasons it is common to combine RAIRS and TPD (Öberg et al., 2009).

It is clear; to realize progress, technological advances are needed. Indeed, recently a number of new developments have been reported (Jones & Kaiser, 2013; Maity et al., 2014; Gudipati & Yang, 2012; Yang & Gudipati, 2014; Belov et al., 1995; Berkenkamp et al., 1996; Ellegaard & Schou, 1998; Georgiou & Koubenakis, 2003; Mihesan et al., 2005a,b;

Pirkl et al., 2012). Successful experiments have been reported in which TPD has been combined with vacuum UV (VUV) single photo-ionisation time-of-flight mass spectrometry (TOF-MS), measuring the mass from desorbing species from the ice (Jones & Kaiser, 2013; Maity et al., 2014). Diagnostic techniques such as Substrate/Matrix Assisted Laser Desorption Ionisation Time-of-Flight Mass Spectrometry ((S/M)ALDI-TOF-MS) have been introduced (Belov et al., 1995; Berkenkamp et al., 1996; Mihesan et al., 2005a). In the case of the MALDI-technique, a laser is used to desorb large molecules by exciting vibrational modes of the matrix molecules in which the molecules of interest are embedded. A similar approach was recently applied in astrochemistry, to investigate radiation-induced processes of Polycyclic Aromatic Hydrocarbons (PAHs), embedded in interstellar ice analogous, using Resonant Enhanced Multi Photon Ionisation (REMPI) as ionisation source (Gudipati & Yang, 2012; Yang & Gudipati, 2014).

Alternatively, the laser energy can be coupled into the substrate to induce the thermal desorption of ice constituents (Nelson et al., 1989; Schieltz et al., 1992; Ellegaard & Schou, 1998; Focsa & Destombes, 2001; Georgiou & Koubenakis, 2003; Ikeda et al., 2013). The desorbed ice constituents are subsequently ionised for example using electron impact ionisation, and analysed with TOF-MS.

Here we describe a new experimental setup, recently constructed and now producing its first data, utilising this sensitive technique: a Mass-Analytical Tool for Reactions in Interstellar ICES. MATRI^{2}CES is an ultrahigh vacuum (UHV) system aimed at simulating conditions in dark interstellar clouds. Low temperature solid state (ice)chemistry is initiated by a microwave powered H_2 discharge lamp that mimics the radiation field that is dominated by Lyman-α radiation and originates in space from cosmic rays excited hydrogen molecules. Such lamps have been used to study the photo-desorption, photo-dissociation and photo-chemistry in interstellar ice analogues (Öberg et al., 2007, 2009). Also, the initial irradiation experiments by Muñoz Caro et al. (2002); Bernstein et al. (2002); Briggs et al. (1992) already mentioned here, were performed with this type of lamps. The performance of MATRI^{2}CES is demonstrated by the vacuum UV photo-processing of solid methane. CH_4, a molecule that has been shown to be present in interstellar (Lacy et al., 1991; Boogert et al., 1996; Gibb et al., 2004; Öberg et al., 2008) (diluted) and planetary ('pure') ices; likely forms upon hydrogenation of C-atoms, and is considered a starting point in the formation of larger hydrocarbons.

2.2 SYSTEM DESCRIPTION

MATRI^{2}CES, shown schematically in figure 2.1, consists of two UHV chambers: the main chamber (A) in which ices are grown and VUV irradiated, and a reflectron time-of-flight tube (B) that is used to monitor laser desorbed species mass spectrometrically. In the main chamber, ices can be deposited under fully controlled conditions at temperatures as low as 20 K. Resistive heating allows to study ices at different temperatures, up to 300 K. A microwave powered H_2 discharge lamp is used to irradiate the ice sample with primarily Lyman-α photons ($\lambda = 121.6$ nm). This lamp (beam path, (L)) has been characterized in much detail recently by Chen et al. (2014).

Typically, the desorption of photo-processed ice constituents is induced by using the unfocused beam of a Nd:YAG laser (Polaris II, New Wave Research, 355 nm, 3-4 ns, beam path, (J)). Additionally, we have the opportunity to work with the fundamental or second harmonic of a Nd:YAG laser. The desorbed molecules are ionised using electron impact ionisation (K) and detected using a reflectron time-of-flight mass spectrometer (Jordan TOF Products, Inc.).

In this section the experimental details are described, time-of-flight to mass and ice-thickness calibrations are presented, and the measurement concept is described in detail.

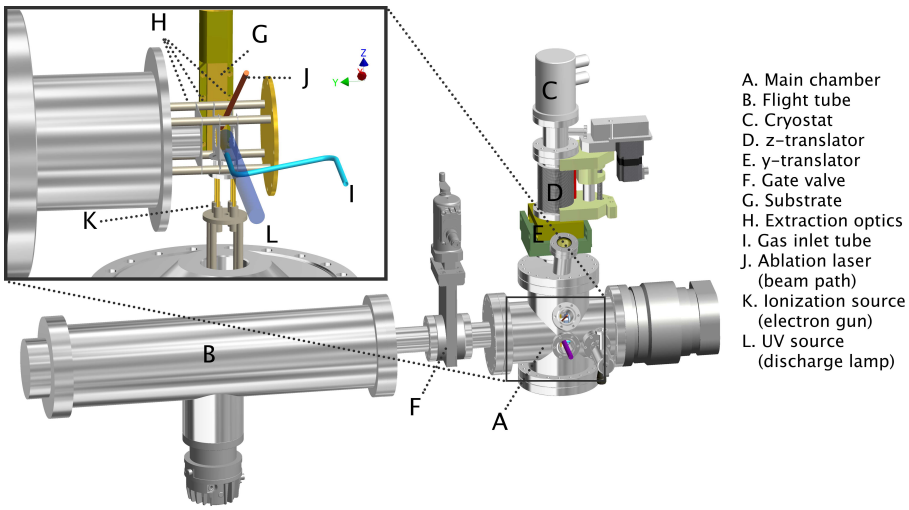

Figure 2.1: Schematic drawing of MATRI^{2}CES (autodesk inventor), in the inset the inside of the main chamber is shown. Prevacuum pump and deposition line are not shown for clarity.

2.2.1 *Main chamber*

The base pressure in the stainless steel main chamber (modified C-685 chamber, Jordan TOF Products, Inc.) is $\sim 10^{-10}$ mbar at room temperature. It is evacuated by a 550 l/s (pumping capacity for N_2) turbo molecular pump (Varian TV551) backed up by a scroll pump (Varian TS600). On top of this chamber all ice cryogenics are mounted. An off-centred gold-coated copper cylinder ($250 \times 12.5^2 \times \pi$ mm^3) rectangular flat sampling surface (15×50 mm^2, (G)) is in thermal contact with the cold finger of a helium closed-cycle cryostat (Advanced Research Systems, DE 202). Although gold is not representative for interstellar dust grains, it has several favourable properties. It is chemically inert, an effective heat conductor and effectively absorbs light in the UV range. Moreover, the ices studied here are thick and as a consequence the influence of the surface is negligible, as has been shown in studies where also other substrates were used. An indium gasket is used to obtain optimal thermal contact between the substrate and the cold finger. The substrate temperature is controlled between 20 to 300 K with a relative precision of 0.5 K, using a cryogenic temperature controller (LakeShore model 331) combined with a chromel–gold/iron alloy thermocouple and a heating element. The thermocouple is inserted below the substrate and the resistive heating element is attached to the cold finger of the cryostat. A gold-coated copper thermal shield (~ 77 K) surrounds 3/4 of the substrate cylinder in order to reach temperatures as low as 20 K.

The cryostat (C) is positioned on top of two bellows with two linear shift mechanisms (z- and y-direction). A motorised translation stage (UHV design, LSM64 − 50, McLennan, 23HT18C stepper motor with a SimStep single axis stepper system) allows to control the vertical motion (z-axis) of the substrate (±25 mm (D)) with variable speeds. A manual translation stage (UHV design, LDM64/64, y-axis, (E)) allows to control the horizontal motion of the substrate (±7.5 mm). The translational stage in the vertical direction (z-axis) is necessary to improve signal-to-noise ratios by accumulating 220 mass spectra, moving the sample and realizing a 'fresh' spot for the laser. The y-axis translation stage enables us to perform a kinetic study on a processed ice sample.

The gas phase precursor species are admitted into the main chamber with an aperture adjusted leak valve (Hositrad, (I)), through a high-vacuum stainless steel gas mixing line connected to a gas reservoir (~ 0.35 liter). The reservoir is then filled up to 40 mbar with CH_4 (Praxair, purity 99.9995%) - as an astronomically relevant ice constituent - or with Ar (Praxair, purity 99.999%) to further characterize the performance of MATRI^{2}CES. Deposition proceeds either under an angle of ~ 85° with a front deposition gas inlet tube, or following a background deposition procedure. In the latter case, a second gas inlet tube, located behind and directed away from the substrate is used which allows the gas phase species to impinge the sampling surface with random trajectories, ensuring an uniform, porous ice growth (Bossa et al., 2012). During front deposition, the substrate translates up and down to obtain a quasi-uniform ice distribution following the z-axis of the sampling area.

The main chamber houses part of the orthogonal reflectron time-of-flight mass spectrometer assembly, which includes the ion extraction region (repeller plate, extraction grid and acceleration grid, H), an electron ionisation source (K), and the ion focusing and horizontal steering plates. The sampling surface is located in the vicinity (~ 4 mm) of both the ion extraction region and the electron ionisation source, in order to minimise the distance neutrals have to travel. This configuration is the most compact that can be realised in this setting and offers the advantage of a high ion transmission, increasing the detection limit.

An ultra-high vacuum magnesium fluoride (MgF_2) viewport is mounted on a DN40 flange, directly facing the sampling area, and allows to measure the ice thickness through optical laser interference (Hudgins et al., 1993; Westley et al., 1998) or is used as input window of the H_2 discharge lamp that is located 14 cm from the substrate surface. Other DN40 and DN160 flanges are used as current and gas inlets and for pressure monitoring that is realized by both a Varian IMG-300 inverted magnetron gauge (1.33×10^{-3} to 6.65×10^{-11} mbar) and a Varian Agilent ConvecTorr Convection-Type Tube Sensor (atmosphere to 1.33×10^{-3} mbar). There is a 30° diagonal DN40 conflat flange available as inlet for the Nd:YAG laser beam, which is used for the ice ablation (J). An ultra-high vacuum gate valve (DN63 conflat flange connections, VAT, (F)) separates the ion source mounting flange from the flight tube and allows to keep UHV in the flight tube during main chamber maintenance.

2.2.2 *Flight tube*

The stainless steel electric field-free flight tube (Jordan TOF Products, Inc.) has a base pressure better than $\sim 10^{-10}$ mbar. This pressure is monitored using a second Varian IMG-300 inverted magnetron gauge. The flight tube is evacuated by a 250 l/s (pumping capacity for N_2) turbo molecular pump (Varian TV301) backed up by a scroll pump (Varian TS600). The tube is 812.8 mm long and can be used in both linear and reflected mode operation. The drift tube houses the remaining part of the orthogonal reflectron time-of-flight mass spectrometer assembly. Namely, a single stage reflectron, and two Multi Channel Plates (MCP): a 40 mm diameter MCP reflected mode detector, and a 18 mm diameter MCP linear mode detector, situated behind the single stage reflectron. Both MCPs have a sub-nanosecond rise time, allowing fast ion pulse handling.

The reflectron time-of-flight mass spectrometer assembly has a D-850 angular reflectron configuration. Mass resolution of 1500 and even 4000 when used with a supersonic jet can be obtained. This is for a configuration containing the shroud, skimmer, pulsed valve and electron gun. In the original design of system (see Isokoski, 2013), the system was used in such a configuration, however due to limited transmission - from ice to ionized reaction products - we have chosen to modify the system to the current version. The

shroud, skimmer and pulsed valve have been removed, limiting the mass resolution (M/ΔM typically ~ 400) but increasing the overall transmission of the system.

2.2.3 *Analytical tools*

A virtual grid of 220×9 non-overlapping desorption spots is set on the ice surface prior to the analysis. For one ice sample, a maximum of 9 mass spectra can be acquired at different irradiation times, each of them averaging over 220 laser shots directed toward different fresh spots along the z-axis of the ice sample. During a mass scan, ice constituents are ablated from the sampling surface with an unfocused, frequency-tripled pulsed (355 nm, 3-4 ns) Nd:YAG laser (Polaris II, New Wave Research), running at 10 Hz repetition rate. The typical laser fluence used for ablation is in the order of ~ 8-9 mJ cm^{-2}. Four fixed mirrors (UV fused silica) and an iris (1 mm aperture) are used to steer and skim each ultraviolet laser pulse with a 30° incidence angle toward a fresh spot on the z-translating ice sample. Subsequent scans can be performed once the base pressure after the previous scan reaches an asymptotic minimum value and once the sampling surface is manually shifted toward the y-axis, i.e., toward the next column of the virtual grid. There is no time delay between the desorption and the ionisation since we use a continuous 70 eV electron ionisation source. The latter is located below the desorption plume, where an orthogonal beam of electrons intercepts the desorbing neutral gas phase species.

The main process occurring during electron impact ionisation can be written as:

$$M + e^- \rightarrow M^{+\bullet} + 2e^-, \quad (1)$$

where M is the neutral species and $M^{+\bullet}$ is the corresponding radical cation. Only positive ions are analysed. At around 70 eV the kinetic energy transferred to the neutral molecules yields a large number of ions. It should be noted that $M^{+\bullet}$ typically has enough internal energy to initiate fragmentation; upon electron impact ionization, more than only the molecular ion peak is expected in the time-of-flight mass spectrum. This may be helpful for structure determination but also comes with the disadvantage that different species may fragment along identical masses. The main concern of electron impact ionization therefore is that the resulting fragmentation can give ambiguous results, even when the unique fragmentation patterns for a large set of astrophysically relevant molecules is available from the NIST Standard Reference Database (Stein, 2014). This is a well known restriction when applying electron impact ionisation.

Ions are generated between the repeller plate and the extraction grid, which are perpendicular to the sampling surface plane. During the ionisation process, these two elements carry the same voltage (1050 V), after which the extraction grid potential is lowered by 100 V (4 μs), thus orthogonally extracting the generated ions to the electric field-free flight tube. The latter allows ions to drift and to separate based on their mass/charge (m/z) ratios. At the end of the flight tube, the ions are back-reflected for improved mass resolution before detection using the 40 mm MCP detector. The reflectron actually compensates the initial kinetic energy distribution by sharpening ion packets of same m/z ratio. The ion signal is then recorded by a PCIe digitizer card (8 bit, 3 GS/s, Gage CobraMax CS13G8).

The timing sequence of the laser pulse, the ion extraction pulse, and the data acquisition trigger is controlled by a delay/pulse generator (DG535, GPIB interface, Stanford Research System). Instrument control, data acquisition and data processing are performed using LabVIEW 8.6 (National Instruments). A typical timing sequence for a separate analysis run is shown in figure 2.2; the flash lamp and Q-switch of the laser are triggered, and after a variable time (typically on the order of μs) the extraction pulse extracts ions into the time-of-flight tube. Depending on the exact difference between the laser pulse and the ion extraction pulse, spatially different parts of the desorption plume can be probed.

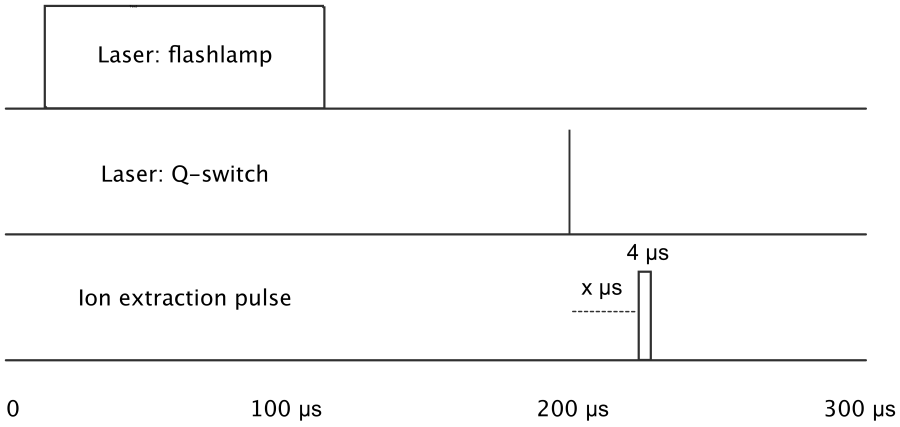

Figure 2.2: Typical time sequence for a diagnostic run.

2.2.4 *Calibration experiments*

The time-of-flight mass (section 2.2.4.1) and ice thickness (section 2.2.4.2) calibration follow standard procedures that are mentioned here for completeness.

2.2.4.1 *Mass calibration*

A 3-point internal calibration is performed for each time-of-flight spectrum using the fragment ion peaks and/or the molecular ion peaks corresponding to the initial ice sample constituents, and by solving the following equation (Håkansson et al., 1998):

$$\mathrm{TOF} = A + B \times \sqrt{m/z} + C \times m/z, \tag{2}$$

with A, B, and C the three parameters to find. The first two terms correspond to the conventional time-of-flight equation and the last term is introduced to improve the mass accuracy over the whole m/z range. The mass coverage used in our experiments extends from 0 to 300 m/z, here the focus is on masses up to 100 m/z and a typical mass resolution with $M/\Delta M$ ~320 to ~ 400.

2.2.4.2 *Thickness Calibration*

During deposition, the ice thickness can be monitored by optical laser interference (Hudgins et al., 1993; Westley et al., 1998) using an intensity stabilised helium neon (He-Ne) laser (Thorlabs HRS015). The laser beam strikes the sampling surface at an incident angle $\theta \simeq 88.5°$. The reflected light is thereafter collected and converted to a digital signal by a photodiode (Thorlabs PDA36A). The ice thickness d can be expressed as a function of interference fringes (m):

$$d = \frac{m\lambda}{2\, n_1 / n_0 \cos\theta_f}, \tag{3}$$

where λ corresponds to the wavelength of the He-Ne laser (632.8 nm), n_0 and n_1 are the refractive indices of vacuum and growing ice, and θ_f is the angle of refraction. A quantitative characterisation of the ice thickness during deposition is possible by correlating the interference fringe pattern of subsequent minima and maxima (m) and the corresponding deposition time. A linear fit to this data provides the best representation of the deposition rate as depicted in figure 2.3.

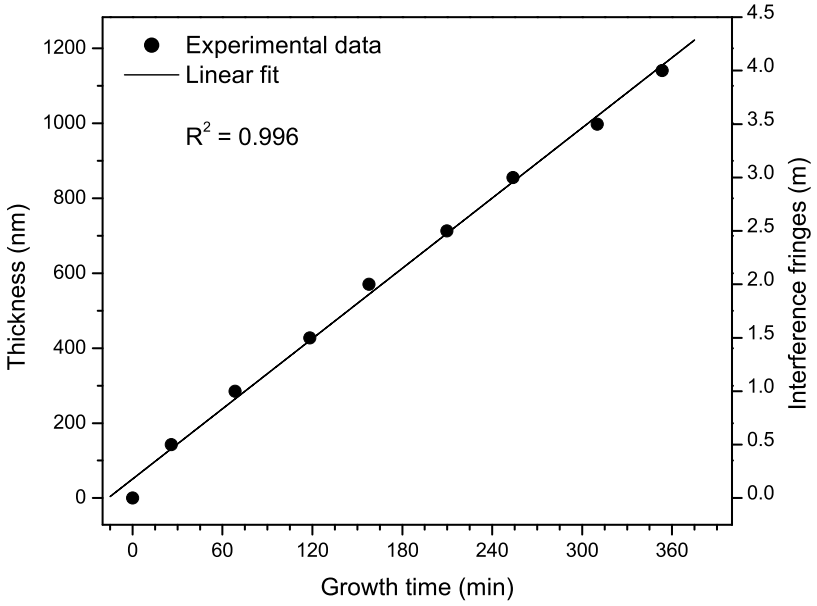

Figure 2.3: Linear fit to subsequent interference fringes minima and maxima (m) and the corresponding thickness vs. deposition time.

In the case of Argon (n=1.29 at 20 K, Sinnock & Smith, 1968) the deposition rate is determined as 3.12 ± 0.08 nm per minute. Icy layers of dust grains in the ISM typical range up to ~ 100 monolayers, assuming that a monolayer has a thickness of 3 Å, relevant ice-thickness would range up to 30 nm. The obtained growth rates can then be adapted to astronomically relevant ice thicknesses.

A similar growth rate has been realized for methane during deposition. In the methane experiments the z-translator cycles up and down to ensure homogenous ice growth along that coordinate. A slight tilt of the sample, combined with surface roughness, did not allow to perform a laser interference calibration. Therefore we have estimated the z-direction coverage of the deposition tube. The previously determined deposition rate for argon ice has been used for ice growth without cycling the z-translator. Combining this estimate with the known deposition rate, we have estimated the ice thickness of our typically deposited ice to be 15 ± 1 nm.

2.2.5 *Experimental Concept*

Methane is let into the mixing line up to a typical pressure of 40 mbar. In order to ensure homogeneous ice growth in the z-direction, the translator cycles up and down during this stage. The y-translator is fixed in the middle. Subsequently, the needle valve is opened up to the calibrated setting aperture, slowly leaking CH_4 into the chamber. Methane molecules will strike the cold substrate, stick, growing a multilayer ice on top. At a sample temperature of 20 K, pressure reading during deposition is typically 2×10^{-8} mbar. The deposition is stopped after about 15 minutes, and the typical ice thickness reached is ~ 15 nm (~ 50 ML).

After deposition, the sample is moved using the y-translator towards the first column of the virtual grid, as described in section 2.2.3. A total of 220 mass spectra are averaged at a 10 Hz repetition rate, without UV irradiation, to record a mass spectrum for the unprocessed ice. The constant vertical speed of the substrate allows the fixed laser beam to hit different 'fresh' spots on the ice sample. The first averaged mass spectrum corresponds to the reference, i.e., pure methane mass spectrum and serves at validating the different settings of MATRI^{2}CES (e.g., alignments, timing and applied potentials). Every single laser shot induces desorption of the ice constituents that are ionised and detected mass spectrometrically. After obtaining the mass spectra, the sample is re-positioned in the starting position.

VUV ice photolysis is started by igniting the H_2 discharge lamp. A wide range of emission spectra and fluxes is accessible by mixing the residual gases with quenching species like noble gases, by adjusting the partial pressure of molecular hydrogen inside the lamp, and by adjusting the microwave power. In order to further control the emission spectrum and fluxes during ice processing, settings as analysed by Chen et al. (2014) (0.7 mbar H_2, Linde 99.999%, 80W, F-type quartz-lamp geometries) are used (Chen et al., 2014). The VUV emission spectrum of the lamp is in the 115-170 nm range, and peaks at 121.6 nm (Lyman-α). Moreover, there is a clear emission band around 160 nm. For the moment we will not focus on the exact lamp settings too much, as the goal of this work is to present a new analysis method for the resulting solid state photoproducts. The photon flux in this range is generally estimated to be $\sim 5 \times 10^{13}$ photons s^{-1} cm^{-2}, which corresponds to a fluence in dense molecular clouds over a period of 10 million of years (Prasad & Tarafdar, 1983). Solid methane absorbs VUV in the range below ~ 130 nm (Wu et al., 2012). Since these photons have a significantly higher energy than the bond dissociation energy of methane, radicals will be formed in the ice. Radical/radical recombination and radical/neutral reactions will result in more complex species such as for example ethane (C_2H_6) (Gerakines et al., 1996; Baratta et al., 2002; Bennett et al., 2006). At different predefined irradiation times, 0.5, 1, 2, 4, 8, 16, 32 and 64 minutes, the VUV emission is stopped and a time-of-flight spectrum is recorded. In this way, the formation of complex species *during* VUV irradiation can be investigated.

This experimental concept has clear advantages with respect to the early experiments, in which the residue had to be studied, *ex situ*, in air, and at room temperature. MATRI^{2}CES allows to record mass spectra at astronomically relevant temperatures and under fully controlled conditions *in situ*. Thermal processing can be largely excluded, and data are recorded basically in real time. In order to characterize the experimental performance of MATRI^{2}CES, this paper focuses on a bottom-up scenario, starting from individual precursors, rather than a mixture. The ultimate goal of this setup, will be to characterize mass spectra of ices as complex as used in the initial radiation experiments (Muñoz Caro et al., 2002; Bernstein et al., 2002).

2.3 RESULTS

In this section we present the behaviour of methane ice under influence of VUV radiation and the validation of the diagnostic concept. This section is divided into three subsections; the first subsection focusses on interpreting the obtained spectra after VUV irradiation qualitatively, the second subsection describes the kinetics following a fitting procedure of the small species, and in the final subsection experimental constraints are discussed.

2.3.1 *Kinetic study: qualitative approach*

The photo-chemical evolution, i.e., fluence dependence of the mass spectra during the 64 minutes of irradiation is presented in figure 2.4. Clearly visible in the reference mass spectrum (t = 0 min), is the fragmentation pattern of CH_4 resulting from the electron impact. In addition to this fragmentation pattern, low intensity peaks appear at m/z 26 ($C_2H_2^+$), 27 ($C_2H_3^+$), 28 ($C_2H_4^+$) and at 32, 33, 48 and 49. The last four peaks can be attributed to CH_4^+-clusters, with m/z 33 and 49 with a combination of $^{13}CH_4^+$ containing clusters and (protonated) clusters. These clusters are the result of the pure nature of the methane ice, and after only eight minutes of irradiation the clusters disappear in the spectra. A substantial amount of larger species has been formed.

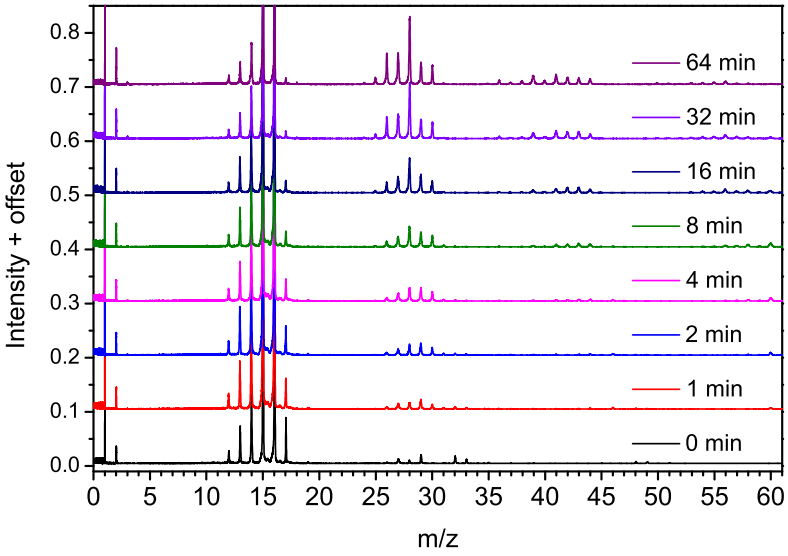

Figure 2.4: Mass spectra of ~15 nm-thick methane ice (CH_4), deposited at 20 K (220 averages) at different VUV irradiation times, using a microwave H_2 discharge lamp. The total fluence ranges from 3×10^{15} photons cm^{-2} (1 min) to 1.9×10^{17} photons cm^{-2} (64 min), corresponding roughly with 10^7 years in a dark interstellar cloud.

Directly after the onset of the irradiation, more complex species such as ethane are formed, as can be deduced from the typical mass fragmentation pattern. This behaviour is in agreement with previous observations using IR spectroscopy of energetically processed methane ice (Gerakines et al., 1996; Baratta et al., 2002; Bennett et al., 2006).

A comparison of the mass spectra shows that the low intensity peaks observed in the reference mass spectrum (t = 0 min) are significantly less pronounced than the peaks arising upon VUV irradiation. From the increasing signal at higher masses, it is clear that for higher fluences the complexity of hydrocarbon species formed in the ice further increases.

A detailed look at the final acquired mass spectrum is presented in figure 2.5. In particular at higher masses (m/z > 48), exact quantification of the individual detected peaks is challenging, as similar mass peaks may be due to different species, but even then it is clear that peaks show up in the $C_6H_x^+$ mass range, evidencing the formation of larger species. Following equation 1, these peaks can only originate from species either with that size or larger.

From this figure it becomes clear that with increasing fluence also the level of molecular complexity in the ice increases. Clearly, a reaction chain is followed in which newly formed species can recombine with radicals, forming even more complex species. For a relatively short irradiation time - in the initial experiments ices were irradiated for days (Muñoz Caro et al., 2002; Bernstein et al., 2002; Briggs et al., 1992) - already rather large species with up to seven carbon atoms can be found. This is very comparable to findings concluded from VUV irradiation of pure methanol ice (Öberg et al., 2009), yielding new species with up to 10 atoms. There further analysis was hindered by spectral confusion and mass spectrometric limitations (mass range). Specifically, the latter point is not an issue with the TOF system used here. However, as stated before, identical fragmentation products (or masses) for different species make an analysis complicated, but not impossible.

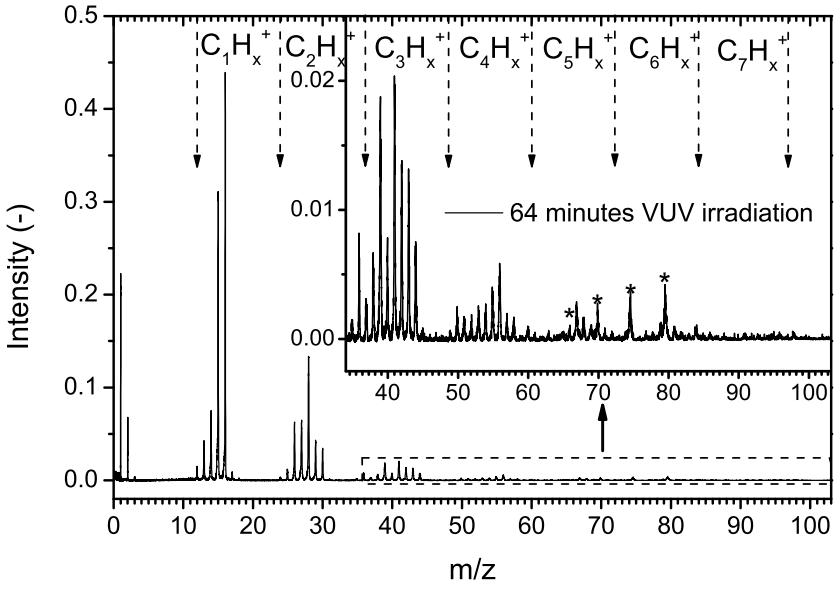

Figure 2.5: Mass spectrum of ~ 15 nm-thick methane ice (CH_4), deposited at 20 K (220 averages). This ice is processed for 64 minutes using the H_2-discharge lamp. The inset shows a detailed version of the high mass part of the spectrum. Peaks with an asterix cannot be related to a specific species and are likely due to the fact that the present experiment lacks a skimmer between the photoprocessing and detection units.

2.3.2 *Kinetic study: quantitative approach*

Solid methane has previously been irradiated using a H_2 microwave discharge lamp, using IR spectroscopy as analytical technique, and also here larger hydrocarbons have been detected (Gerakines et al., 1996; Baratta et al., 2002; Bennett et al., 2006). In order to quantify the kinetics upon solid CH_4 irradiation (figure 2.4) we fitted the mass spectra recorded at different irradiation times.

The overall time-of-flight spectra are first mass-calibrated as described in section 2.2.4.1. Subsequently, the mass spectra are baseline corrected, by fitting a baseline through an array of points where no signal is present. The individual peaks are then integrated to obtain the total intensity of every single mass. This intensity is proportional to the number of ions detected.

Each mass spectrum obtained at different irradiation times is regarded as a linear combination of n individual compounds present in the ablated material:

$$MS_t = \sum_{i=1}^{n} a_i \times \sigma_i \times MS_i \tag{4}$$

where MS_t is the mass spectrum acquired at a specific irradiation time t, a_i corresponds both to the fitting parameter and to the mole fraction of a constituent i, σ_i and MS_i are the corresponding electron impact cross section and the reference electron impact mass spectrum, respectively. The fitting procedure is driven by Matlab 7.9.0 (R2009b), and uses the Nelder-Mead optimisation algorithm (Lagarias et al., 1998). Figure 2.6 shows an example of the fitting procedure of the mass spectrum discussed before after 64 min VUV photolysis of CH_4 at 20 K. The red crosses in the top panel of the figure show the best fit of equation 4 to the mass spectrum together with the residuals in the bottom panel. The fitting library is shown in table 2.1, and consists of all hydrocarbons containing less than four carbon atoms as well as possible contaminants. Larger species are excluded in the fitting library, since the accuracy of the fit above m/z 48 is similar to the intensity of the individual peaks.

Table 2.1: Electron-impact cross sections of species considered in the mass fitting routine.

Name	Formula	σ_{70eV} (Å^2) (Kim et al., 2014)
Methane	CH_4	3.524
Ethane	C_2H_6	6.422
Ethylene	C_2H_4	5.115
Acetylene	C_2H_2	4.374
Propane	C_3H_8	8.619
Propene	C_3H_6	8.736
Allene	C_3H_4	8.080
Propyne	C_3H_4	7.662
Nitrogen	N_2	2.508
Oxygen	O_2	2.441
Water	H_2O	2.275

The photo-chemical evolution of the species, fitted from the kinetics mass spectra (figure 2.5) is shown in figure 2.7. The same fitting library, table 2.1, is used for all mass spectra at different irradiation times. The degeneracy of the fit has been examined by using different initial guesses for all parameters (a_i); the same minimum was found, resulting in the same set of abundances. Photodesorption has been neglected and the sum of all species is normalised to 100%. Propyne is not observed in the 64 minutes irradiation, but most likely can be formed if the propene abundance further increases during longer irradiation time scales. We are confident about the fit, since the formation trend of the species makes sense from a chemical perspective.

In previous photo-processing studies of solid methane, the formation of ethane and propane were observed, and clearly larger aliphatic chains were also formed (Gerakines et al., 1996; Baratta et al., 2002; Bennett et al., 2006). As the vibrational modes of different hydrocarbons are rather similar, their absorption profiles overlap substantially. MATRI^{2}CES has the capability of providing additional insights in the formation networks of such species, and this will be discussed in Chapter 4 (Bossa et al., 2015).

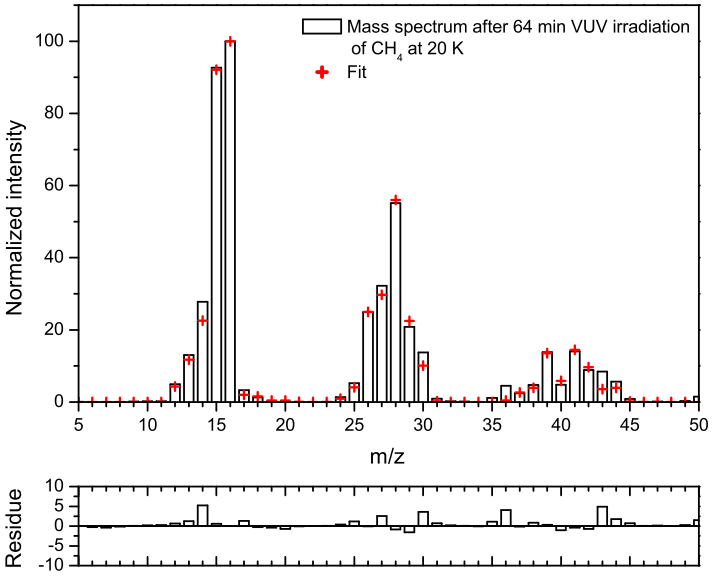

Figure 2.6: Fitting the mass spectrum obtained after 64 min VUV photolysis of CH_4 at 20 K in linear combination of 70 eV electron impact mass spectrum (NIST Standard Reference Database 69: NIST Chemistry WebBook) and electron impact cross sections (NIST: Electron-Impact Cross Section Database).

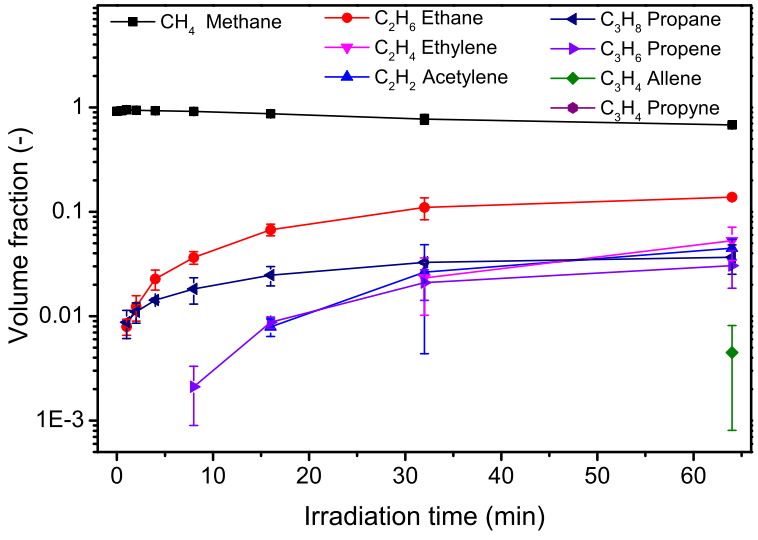

Figure 2.7: Evolution of small hydrocarbons during the first 64 minutes of VUV irradiation. The error bar is based on three times the standard deviation, the large error at t = 32 min is due to a smaller statistical sample. Propyne is included in the fitting library, but is not observed.

2.3.3 *Validation experiments*

In this section, the performance of the system is validated, as MATRI^{2}CES is crossing untouched areas. In the following subsections, the influence of the laser ablation wavelength and the extraction time will be discussed, as well as the detection limit and the typical mass resolution obtained.

2.3.3.1 *Ablation wavelength dependance*

In order to investigate the influence of laser wavelength, we have repeated experiments for three clearly different wavelengths. The fundamental of a Nd:YAG laser, frequency doubled and tripled: 1064, 532 and 355 nm, respectively, have all been used to ablate pure CH_4 ice. At these three wavelengths, CH_4 has no clear overlap with electronic transitions. Common interstellar ice constituents such as H_2O, CH_3OH, CO, e.g. do not exhibit transitions at these wavelengths either. The resulting mass spectra are shown in figure 2.8.

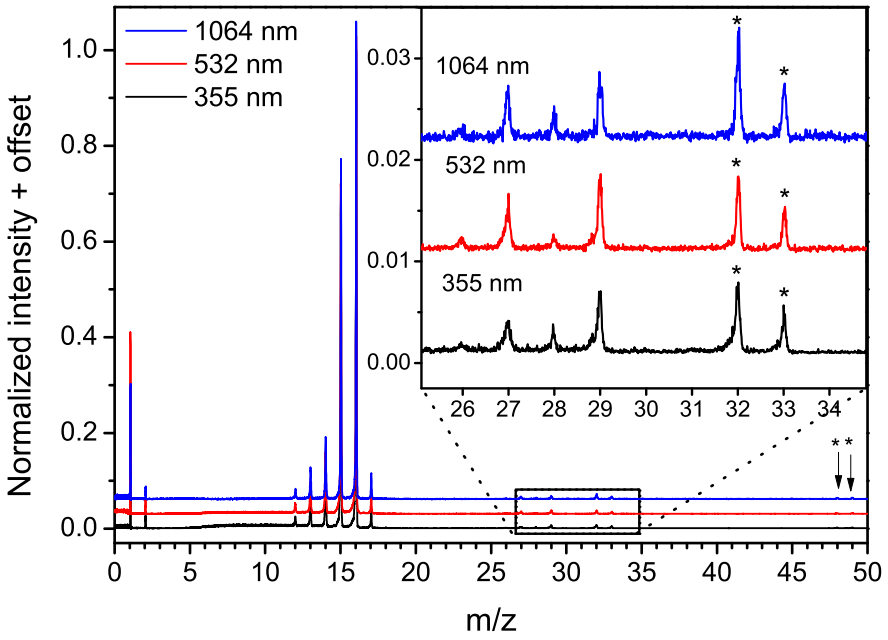

Figure 2.8: Mass spectra of ablated CH_4 ice using different wavelength of ablation. Peaks marked with an asterix (∗) are attributed to CH_4 clusters. The inset shows a zoom-in of the part containing additional peaks. The shown mass spectra are normalised to m/z 16 peak for comparison.

Clearly visible in these spectra, is the fragmentation pattern of CH_4 resulting from the electron gun ionisation. In addition to the fragmentation pattern, low intensity peaks appear at m/z 26 ($C_2H_2^+$), 27 ($C_2H_3^+$), 28 ($C_2H_2^+$) and m/z 32, 33, 48 and 49 originate from CH_4 clusters, as previously discussed, a combination of $^{13}CH_4^+$ containing clusters and protonated clusters. The intensity of the observed peaks at m/z 26, 27, 28 and 29 slightly differs between different wavelengths, however the same peaks are observed. The amount of energy per pulse to induce desorption of the ice differs strongly with wavelength, as is expected from the properties of gold. Gold absorbs UV photons with a high efficiency, while only a small fraction of IR photons is absorbed. This experiment shows that the ablation process in the examined wavelength range is similar. We have opted to use 355

nm for the VUV irradiation experiments, since applying different wavelengths does not affect the final mass spectrum. Additionally, 355 nm photons are efficiently absorbed by the gold substrate, we therefore need a relatively low pulse energy.

2.3.3.2 *Ion extraction time*

As mentioned before, the time sequence is controlled by the DG535 pulse generator. After the laser pulse induces desorption, a plume of desorbing ice constituents is directed toward both the ion optics and ionisation source. Different time delays between the laser pulse and the ion extraction pulse are taken to probe the different parts of the desorption plume and ultimately to optimise the extraction timing and the signal-to-noise ratio (figure 2.2, x µs). Figure 2.9 shows a typical ion extraction time scan from an argon ice with a thickness of ~ 70 ML. Argon is used here, instead of CH_4, since its isotopes offer a direct way to estimate the sensitivity level of MATRI^{2}CES. Each of these spectra is the average of 220 individual spectra.

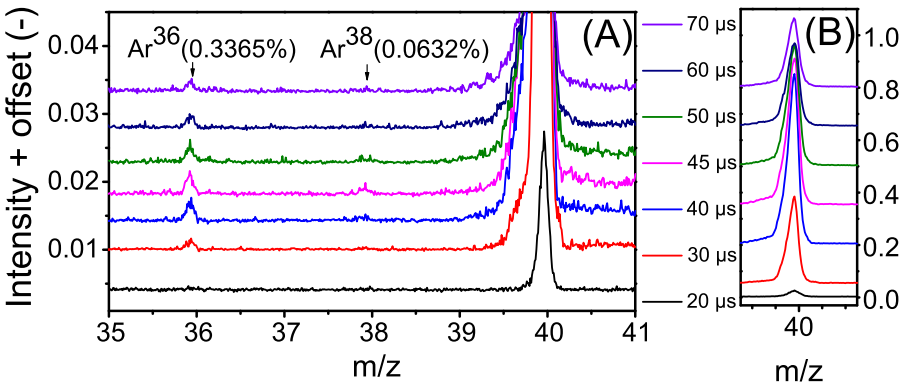

Figure 2.9: Mass spectra of ablated Argon ice with a thickness of 70ML, the time label indicates time difference between laser pulse and ion extraction of ions to the flight tube. Panel (A) contains the overview, focussing on the Argon isotopes, $^{36}Ar^+$ and $^{38}Ar^+$. Panel (B) contains the main $^{40}Ar^+$ peak.

In figure 2.10, the integrated area of the $^{40}Ar^+$ is plotted versus the ion extraction time. Depending on laser fluence, and ice thickness the optimal extraction time can differ slightly, with typical values in the 15 to 70 µs range. In this example the optimal time difference between the laser pulse and the ion extraction pulse is 45 µs.

2.3.3.3 *Detection limit and mass resolution*

The detection limit of the instrument is estimated by ablating different thin films of pure argon ice at 20 K. In contrary to the deposition of methane, the z-translator does not cycle up and down during deposition, providing a more accurate estimation of the ice-thickness. Argon has the additional advantage that it does not fragment upon electron impact ionization, and the two existing stable isotopes aid in determining the detection limit of MATRI^{2}CES. The experimental conditions are the same as with the photolysis experiments. By monitoring the two stable isotopic peaks, $^{38}Ar^+$ and $^{36}Ar^+$, and combining this observation with their natural abundances, 0.063% and 0.337%, an estimate of the detection limit can be obtained.

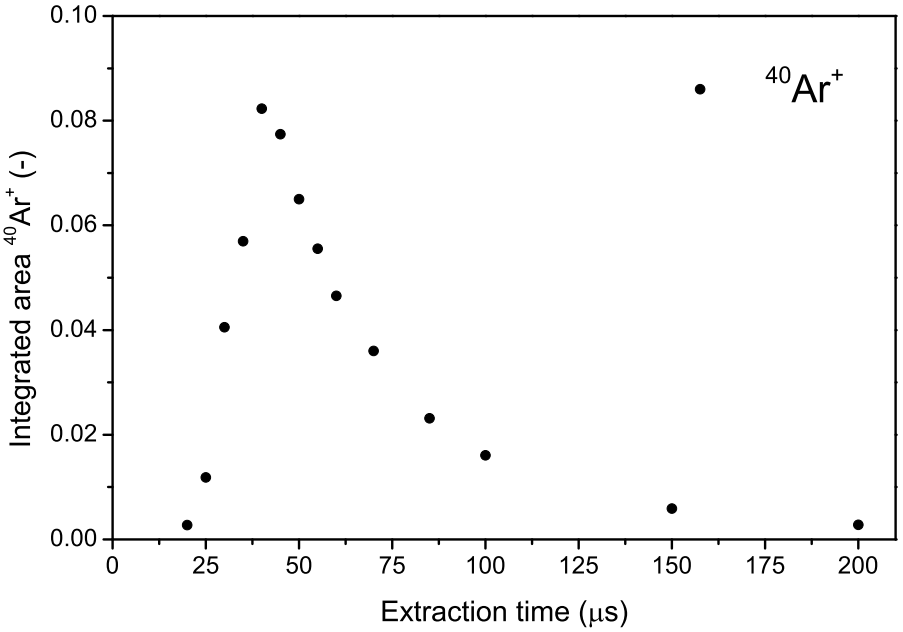

Figure 2.10: Integrated area of the $^{40}Ar^+$ peak versus extraction time, the time difference between the laser pulse and the ion extraction pulse.

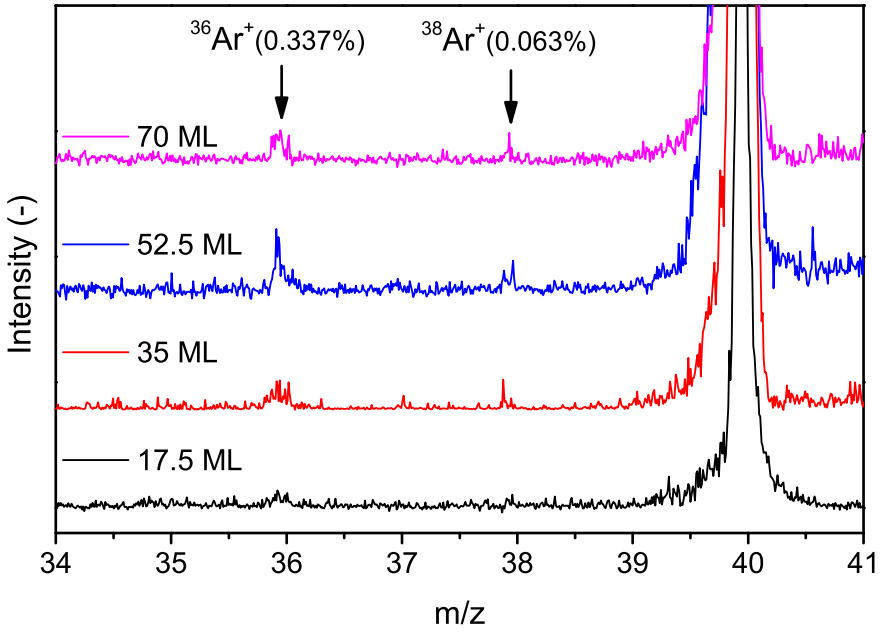

Figure 2.11: Mass spectra of laser ablated argon ice of different layer thickness. The two stable argon isotopes are used to estimate the detection limit of the experiment.

The detection limit has a strong dependence on the settings of the DAQ-card. In this case we try to derive the detection limit of MATRI^{2}CES under the same conditions as with the VUV irradiation experiments. The laser ablation intensity is kept constant over the different experiments, only the ion extraction time is optimised for every different ice thickness. In figure 2.11 the results for different argon ice thicknesses are shown.

For an ice thickness of 35 ML, the $^{38}Ar^+$ becomes clearly visible. This inclines that the typical detection limit using these specific settings, is equal to or better than, 35 ML $\times$ 0.063% $\leqslant$ 0.02 ML. This value is significantly better than other solid state techniques such as IR spectroscopy.

Analysing $^{40}Ar^+$ by taking the FWHM, the mass resolution obtained for ablated argon ice is M/ΔM ~ 400. For solid CH_4 the mass resolution for the molecular ion peak is M/ΔM ~ 320. This mass resolution is more than sufficient to apply for heavier species.

2.4 CONCLUSIONS

MATRI^{2}CES, a new ultra-high vacuum experimental setup, introduced here, combines laser desorption with TOF mass spectrometry to study photo induced chemical processes in interstellar ice analogues, taking advantage of the high sensitivity of mass spectrometric techniques. Utilising this new *in situ* analysis method, we have demonstrated that VUV photo-processing ($\sim 1.9 \times 10^{17}$ photons cm^{-2}) of solid CH_4 ice yields species with at least 6 carbon atoms. With a more quantitative approach, using electron induced fragmentation patterns listed in the NIST database, we demonstrate that we can trace the formation routes of small carbon species in our methane ice upon VUV photo-processing. Electron impact cross sections and fragmentation patterns for different molecules are known and can be used to interpret the obtained mass spectra. The advantage of electron impact ionisation over for example REMPI is its general applicability. REMPI strongly depends on photon cross sections, while the cross sections for electron impact ionisation are in the same order of magnitude. Additional information on individual reactions in the photochemistry can be obtained using for example deuterated species and ^{13}C-labelling.

The results presented here show the potential of this new experimental setup for astrochemistry. It provides an additional, complementary analysis method, next to the regular solid state techniques, of examining the processes occurring in the solid phase. We expect that MATRI^{2}CES will be able to bridge solid state reaction in interstellar ices as studied so far, *i.e.*, for relatively small molecules, to larger species of (pre) biotic interest. MATRI^{2}CES also holds the potential to provide rate constants and branching ratios of photochemical reactions.

The experiments performed here on CH_4 ice are of limited astronomical interest. Methane ice exists (Lacy et al., 1991; Boogert et al., 1996; Gibb et al., 2004; Öberg et al., 2008), but in the ISCM it is not found in a pure form. For this reason, also CH_4 in H_2O will be studied. The ultimate aim of MATRI^{2}CES, is to investigate *in situ* the formation of complex organic molecules, for example sugars and amino-acids, under the photo-processing of interstellar ice analogous. Can these species be formed in photo-processed interstellar ice analogous? In what kind of environment (ice composition, temperature, VUV fluence) will they form more efficiently? With the settings described here such objectives now come within reach, and the goal for the nearby future is to reproduce previous mixed bulk ice experiments, but now for fully controlled experimental conditions.

BIBLIOGRAPHY

Baratta, G. A., Leto, G., & Palumbo, M. E. 2002, Astron. Astrophys., 384, 343
Belov, M. E., Alimpiev, S. S., Mlynsky, V. V., Nikiforov, S. M., & Derrick, P. J. 1995, Rapid Commun. Mass Spectrom., 9, 1431
Bennett, C. J., Jamieson, C. S., Osamura, Y., & Kaiser, R. I. 2006, Astrophys. J., 653, 792
Berkenkamp, S., Karas, M., & Hillenkamp, F. 1996, Proc. Natl. Acad. Sci., 93, 7003
Bernstein, M. P., Dworkin, J. P., Sandford, S. A., Cooper, G. W., & Allamandola, L. J. 2002, Nature, 416, 401
Boogert, A. C. A., Schutte, W. A., Tielens, A. G. G. M., et al. 1996, Astron. Astrophys., 315, L377
Bossa, J.-B., Duvernay, F., Theulé, P., et al. 2009, Astron. Astrophys., 506, 601
Bossa, J.-B., Isokoski, K., de Valois, M. S., & Linnartz, H. 2012, Astron. Astrophys., 545, A82
Bossa, J.-B., Paardekooper, D. M., Isokoski, K., & Linnartz, H. 2015, Phys. Chem. Chem. Phys., 17, 17346
Briggs, R., Ertem, G., Ferris, J. P., et al. 1992, Origins. Life. Evol. B., 22, 287
Chen, Y.-J., Chuang, K.-J., Muñoz Caro, G. M., et al. 2014, Astrophys. J., 781, 15
Chen, Y.-J., Nuevo, M., Yih, T.-S., et al. 2008, Mon. Not. R. Astron. Soc., 384, 605
de Marcellus, P., Meinert, C., Nuevo, M., et al. 2011, Astrophys. J. Lett., 727, L27
Ellegaard, O. & Schou, J. 1998, J. Appl. Phys., 83, 1078
Elsila, J. E., Dworkin, J. P., Bernstein, M. P., Martin, M. P., & Sandford, S. A. 2007, Astrophys. J., 660, 911
Focsa, F. & Destombes, J. 2001, Chem. Phys. Lett., 347, 390
Garrod, R. T. & Herbst, E. 2006, Astron. Astrophys., 457, 927
Georgiou, S. & Koubenakis, A. 2003, Chem. Rev., 103, 349
Gerakines, P. A., Schutte, W. A., & Ehrenfreund, P. 1996, Astron. Astrophys., 312, 289
Gibb, E. L., Whittet, D. C. B., Boogert, A. C. A., & Tielens, A. G. G. M. 2004, Astrophys. J. Suppl. Ser., 151, 35
Gudipati, M. S. & Yang, R. 2012, Astrophys. J. Lett., 756, L24
Håkansson, K., Zubarev, R., & Håkansson, P. 1998, Rapid Commun. Mass Spectrom., 12, 705
Herbst, E. & van Dishoeck, E. F. 2009, Ann. Rev. Astron. Astrophys., 47, 427
Holtom, P. D., Bennett, C. J., Osamura, Y., Mason, N. J., & Kaiser, R. I. 2005, Astrophys. J., 626, 940
Hudgins, D. M., Sandford, S. A., Allamandola, L. J., & Tielens, A. G. G. M. 1993, Astrophys. J. Suppl. Ser., 86, 713
Hudson, R. L., Moore, M. H., Dworkin, J. P., Martin, M. P., & Pozun, Z. D. 2008, Astrobiology, 8, 771
Ikeda, A., Matsumoto, M., Ogura, S., Okano, T., & Fukutani, K. 2013, J. Chem. Phys., 138,
Isokoski, K. 2013, PhD thesis, Leiden Observatory, Leiden University
Isokoski, K., Bossa, J.-B., Triemstra, T., & Linnartz, H. 2014, Phys. Chem. Chem. Phys., 16, 3456
Jones, B. M. & Kaiser, R. I. 2013, J. Phys. Chem. Lett., 4, 1965
Kim, Y.-K., Irikura, K., Rudd, M., et al. 2014, Electron-impact cross sections for Ionization and Excitation
Kobayashi, K., Kasamatsu, T., Kaneko, T., et al. 1995, Adv. Space Res., 16, 21
Lacy, J. H., Carr, J. S., Evans, N. J., et al. 1991, Astrophys. J., 376, 556
Lafosse, A., Bertin, M., Domaracka, A., et al. 2006, Phys. Chem. Chem. Phys., 8, 5564
Lagarias, J., Reeds, J., Wright, M., & Wright, P. 1998, SIAM. J. Optim., 9, 112
Linnartz, H., Bossa, J.-B., Bouwman, J., et al. 2011, Proc. Int. Astron. Union., 280, 390
Maity, S., Kaiser, R. I., & Jones, B. M. 2014, Farad. Discuss., 168, 485
Mihesan, C., Ziskind, M., Chazallon, B., Focsa, C., & Destombes, J. 2005a, Appl. Surf. Sci., 248, 238
Mihesan, C., Ziskind, M., Chazallon, B., et al. 2005b, Surf. Sci., 593, 221
Muñoz Caro, G. M., Meierhenrich, U. J., Schutte, W. A., et al. 2002, Nature, 416, 403
Nelson, R., Rainbow, M., Lohr, D., & Williams, P. 1989, Science, 246, 1585
Nuevo, M., Auger, G., Blanot, D., & d'Hendecourt, L. 2008, Origins. Life. Evol. B., 38, 37
Nuevo, M., Meierhenrich, U. J., d'Hendecourt, L., et al. 2007, Adv. Space Res., 39, 400
Nuevo, M., Meierhenrich, U. J., Muñoz Caro, G. M., et al. 2006, Astron. Astrophys., 457, 741
Öberg, K. I., Boogert, A. C. A., Pontoppidan, K. M., et al. 2008, Astrophys. J., 678, 1032
Öberg, K. I., Fuchs, G. W., Awad, Z., et al. 2007, Astrophys. J. Lett., 662, L23

Öberg, K. I., Garrod, R. T., van Dishoeck, E. F., & Linnartz, H. 2009, Astron. Astrophys., 504, 891

Pirkl, A., Soltwisch, J., Draude, F., & Dreisewerd, K. 2012, Anal. Chem., 84, 5669

Prasad, S. S. & Tarafdar, S. P. 1983, Astrophys. J., 267, 603

Schieltz, D., Chou, C.-W., Luo, C.-W., et al. 1992, Rapid Commun. Mass Spectrom., 6, 631

Sinnock, A. C. & Smith, B. L. 1968, Phys. Lett. A, 28, 22

Stein, S. 2014, "Mass Spectra" in NIST Chemistry WebBook, NIST Standard Reference Database Number 69, Eds. P.J. Linstrom and W.G. Mallard, National Institute of Standards and Technology, Gaithersburg MD, 20899, http://webbook.nist.gov, (retrieved May 7, 2014).

Theulé, P., Duvernay, F., Danger, G., et al. 2013, Adv. Space Res, 52, 1567

Westley, M. S., Baratta, G. A., & Baragiola, R. A. 1998, J. Chem. Phys., 108, 3321

Wu, Y.-J., Wu, C. Y. R., Chou, S.-L., et al. 2012, Astrophys. J., 746, 175

Yang, R. & Gudipati, M. S. 2014, J. Chem. Phys., 140,

3

CONTROLLING THE EMISSION PROFILE OF A MICROWAVE DRIVEN H_2 DISCHARGE LAMP TO SIMULATE INTERSTELLAR RADIATION FIELDS

Context. Microwave discharge hydrogen-flow lamps have been used for more than half a century to simulate interstellar UV radiation fields in the laboratory. Recent discrepancies between identical measurements in different laboratories, as well as clear wavelength dependent results obtained in monochromatic (synchrotron) experiments, hint at a more elaborate dependence on the exact discharge settings than assumed so far.
Aims. We have investigated systematically two lamp geometries in full dependence of a large number of different running conditions and the spectral emission patterns are characterized for the first time with fully calibrated absolute flux numbers.
Methods. A sophisticated plasma lamp calibration set-up has been used to record the Vacuum-UV emission spectra with a spectral resolution of 0.5 nm and bandwidth of 1.6 nm in the 116-220 nm region. Spectra are compared with the output of a calibrated D_2-lamp which allows a derivation of absolute radiance values.
Results. The general findings of over 200 individual measurements are presented, illustrating how the lamp emission pattern depends on i) microwave power, ii) gas and gas mixing ratios, iii) discharge lamp geometry, iv) cavity positioning, and v) gas pressure.

N.F.W. Ligterink,* D.M. Paardekooper,* K.-J. Chuang, M.L. Both, G.A. Cruz-Diaz, J.H. van Helden and H. Linnartz *Controlling the Emission Profile of a MW driven H_2 Discharge Lamp to simulate Interstellar Radiation Fields*, Astron. Astrophys., 584, (2015) A56.
* *Both authors contributed equally to this work*

3.1 INTRODUCTION

For the last two decades, microwave discharge hydrogen-flow lamps (MDHLs) (Warneck, 1962; Davis & Braun, 1968) have been widely used as vacuum-ultraviolet (VUV) light sources in laboratory experiments to simulate interstellar radiation fields in astrochemical studies (Westley et al., 1995; Gerakines et al., 1996; Baratta et al., 2002; Muñoz Caro et al., 2002; Cottin et al., 2003; Leto & Baratta, 2003; Loeffler et al., 2005; Watanabe et al., 2007; Öberg et al., 2007; Muñoz Caro et al., 2010; Islam et al., 2014; Cook et al., 2014; Henderson & Gudipati, 2015). These experiments aim to simulate and ultimately unravel the complex photoprocesses (photodesorption, photodissociation, and photochemistry) taking place in interstellar ice analogues. The spectral distribution of the interStellar radiation field (ISRF) is strongly dependent on the interstellar environment. As ice processing is particularly interesting in dark interstellar clouds which are largely shielded from external light sources, laboratory studies have been focusing on simulating the VUV photons emitted by H and H_2 after excitation by cosmic rays that do penetrate the cloud. In the laboratory, these photons are produced using a MDHL. Typically, it has been assumed that the lamp spectrum is dominated by Lyman-α photons around 121 nm, with a broad and weaker emission band situated around 160 nm. The estimated flux of the MDHL at sample position in a number of papers is based on previously reported values in the literature, which roughly span between 10^{13}-10^{15} photons $s^{-1}cm^{-2}$ and generally lack information on the spectral energy distribution (SED). However, exact running conditions of the lamp, i.e. the dependence on the experimental settings, influence both the total photon flux and the SED of the impacting radiation at the ice sample. In other situations the flux of the lamp is either directly measured using a NIST (National Institute of Standards and Technology) calibrated photodiode or indirectly by actinometry using for example the conversion of O_2 to O_3 (Gerakines et al., 1996; Cottin et al., 2003; Islam et al., 2014; Fulvio et al., 2014). When using a NIST calibrated photodiode for photon flux measurements, the quantum yield is known at different wavelengths. Since the photodiode is also sensitive to visible light, the contribution of visible light emitted by the MDHL has to be taken explicitly into account as well. In the actinometry case, the O_2 to O_3 conversion efficiency typically used is taken from gas phase experiments performed by Groth (1937). Recent experiments indicate that the quantum efficiency in the solid state is significantly lower (Cottin et al., 2003; Fulvio et al., 2014) and hint toward a wavelength dependency, although detailed wavelength dependent studies are still lacking in the literature.

It is clear that both calibration methods require knowledge of the emission spectrum of the lamp to accurately determine the flux at different photon energies, which strongly depends on the experimental settings.

The importance of controlling the emission spectrum of the MDHLs has been pointed out by various recent studies (Chen et al., 2014; Es-sebbar et al., 2015). Photodesorption rates for several molecules using synchrotron radiation (Fayolle et al., 2011, 2013) as well as direct cross section measurements of the main constituents of interstellar ice show strong wavelength dependences in the VUV domain (Cruz-Diaz et al., 2014a,b). Recently, Chen et al. (2014) showed that the differences in CO photodesorption rates reported by various groups over the past decade may be partly explained by differences in MDHL emission spectra. Carbon monoxide is an excellent example, since it strongly absorbs 160 nm photons while Lyman-α photons are clearly off resonance, as has been shown in independent experiments (Fayolle et al., 2011; Cruz-Diaz et al., 2014a).

The main purpose of the present study is to systematically identify the importance of various parameters for operating the MDHL: pressure, gas compositions (H_2, D_2, addition of He), microwave power, lamp geometry, pumping efficiency, and cavity positioning. The systematic approach presented here allows the optimization of lamp settings for specific

experiments, using the MDHL in a more wavelength selective way. The study complements the work of Chen et al. (2014) and more recently Es-sebbar et al. (2015). The main difference between the present work and these two recent studies is that the spectral irradiance of the MDHLs is characterized absolutely, using a fully calibrated measurement procedure. This allows us to obtain the relative photon flux in full wavelength dependence.

We also list a number of very practical issues, such as the degradation of MgF_2 windows that are typically used and potentially affect the overall outcome of studies in which accurate flux numbers are needed. It should be noted though, that the paper is not intended as a reference to skip calibration procedures. In the best case, the right order of magnitude can be derived from the information given here. The dependences that are described below will make it clear that flux measurements at the sample distance are necessary to guarantee that numbers depending on absolute photon fluxes are correct.

3.2 EXPERIMENTAL

Section 3.2.1 describes the microwave discharge hydrogen-flow lamp, while in section 3.2.2 the UV/VUV spectrometer used for characterization is described. To convert the different radiation units, from irradiance to photon flux at the sample distance, an additional calibration set-up had to be constructed, which is described in section 3.2.3. To test the implications that result from this work, in section 3.2.4 the main characteristics of one of our UHV ice set-ups are described. The astronomical relevance of the MDHL findings is illustrated here with VUV ice irradiation experiments for different lamp settings.

3.2.1 *Microwave discharge hydrogen-flow lamp*

The MDHL consists of a pyrex lamp-tube and an air-cooled Sairem Evenson microwave cavity which is powered by a Sairem GMP 03 K/SM microwave generator. The plasma is ignited using a BD-10A high frequency generator. The geometry of the lamp-tube can be either F- or T-type, as depicted in figure 3.1. This lamp-tube is connected to a set-up using an UHV MgF_2 window (Torr Scientific Ltd) and a custom-made connection piece. A rubber ring seals off the connection at the lamp side, the other two available ports are used for the inlet and outlet of the gas flowing through the tube. The port near the MgF_2 window is typically the inlet of the gas. The system is evacuated by either a TS300 dry scroll pump or a DS-302 rotary vane pump, both manufactured by Agilent. The typical base pressure of the system obtained with the scroll pump and oil pump are $\sim 10^{-2}$ mbar and $\sim 5-10\times10^{-3}$ mbar, respectively. Pressure monitoring is performed at various positions. Two gauges (Agilent PCG-750 and Granville-Phillips Convectron gauge) are situated at the inlet of the gas flow and an additional Agilent PCG-750 is attached near the outlet. These gauges have been calibrated for H_2 with reference to both $0.00-10.00$ mbar and $0-1000$ mbar Edwards Barocell manometers with a 0.15% accuracy of reading. All the pressure values mentioned and presented are absolute values. The gas inlet of the lamp-tube can be directly connected to a needle valve, reducer, and gas bottle or to a flow controller gas mixing system. The latter can be used for pure gasses and binary gas mixtures. Flow rates in this system are given in standard cubic centimetres per minute (sccm). The gas outlet of the lamp tube is connected to a pump without further flow restrictions. Gasses used in our experiments are hydrogen (99.999% pure, Air Liquide / Alphagaz), helium (99.999% pure, Air Liquide / Alphagaz), and deuterium (99.8% pure, Air Liquide / Alphagaz).

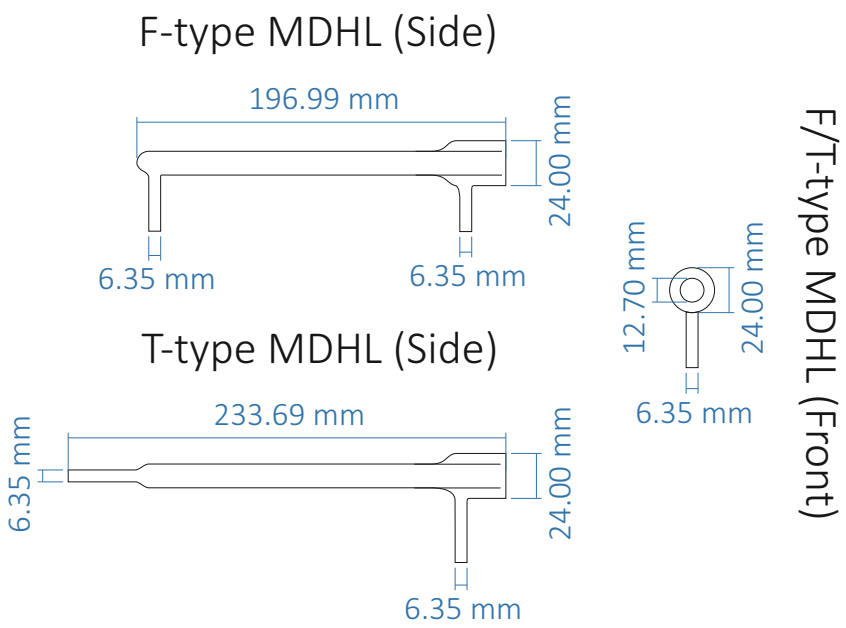

Figure 3.1: Schematic of the F- and T-type MDHL used in this study. Both lamps are based on commercially available Opthos Instruments MDHLs.

3.2.2 *Greifswald UV/VUV spectrometer*

All spectra presented here were measured in November 2014 during a one-week measurement campaign at the UV/VUV spectroscopy set-up located at the Leibniz Institute for Plasma Science and Technology (INP Greifswald, Germany). This set-up, schematically depicted in figure 3.2, has been routinely used for the last two decades as a diagnostic tool for characterizing the UV/VUV emission of (atmospheric) plasma (Foest et al., 2007; Lange et al., 2009). The system consists of two independent optical beam lines which can be coupled into the VUV-monochromator by a shared rotatable parabolic mirror. The entire set-up is evacuated to high vacuum ($\sim 2 \cdot 10^{-6}$ mbar) conditions by turbo molecular pumps. The MDHL is mounted onto the inlet of the first beam line, while the rest of the system is kept at high vacuum conditions by a shutter valve. The light from the lamp passes through a MgF_2 window (Torr Scientific Ltd, 115 nm cut off) and a pinhole (0.6 mm diameter), and is directed towards the parabolic mirror. The second beam line houses a deuterium lamp (Cathodeon V03) of which the spectral radiance (E_λ: $\mu W\ sr^{-1}\ mm^{-2}\ nm^{-1}$) in the 116-220 nm range is known; this lamp was calibrated by the Physikalisch Technische Bundesanstalt (PTB). The orientation of the rotatable parabolic mirror (focus length 1.5 m) determines which of the two beam lines is optically connected to the spectrometer. The entrance slit of the spectrometer is set to 1.0 mm, giving a spectral bandwidth of 1.6 nm. In this way the absolute response of the complete system is thus determined for a spectral bandwidth of 1.6 nm.

The 0.5 m path-length spectrometer (VM-505 Acton Research) has a 1200 g/mm grating. Light exits through a 1 mm slit and is detected by a VUV-photon multiplier tube. The output of the calibrated spectra is given in absolute spectral radiance as $\mu W\ sr^{-1}\ mm^{-2}\ nm^{-1}$.

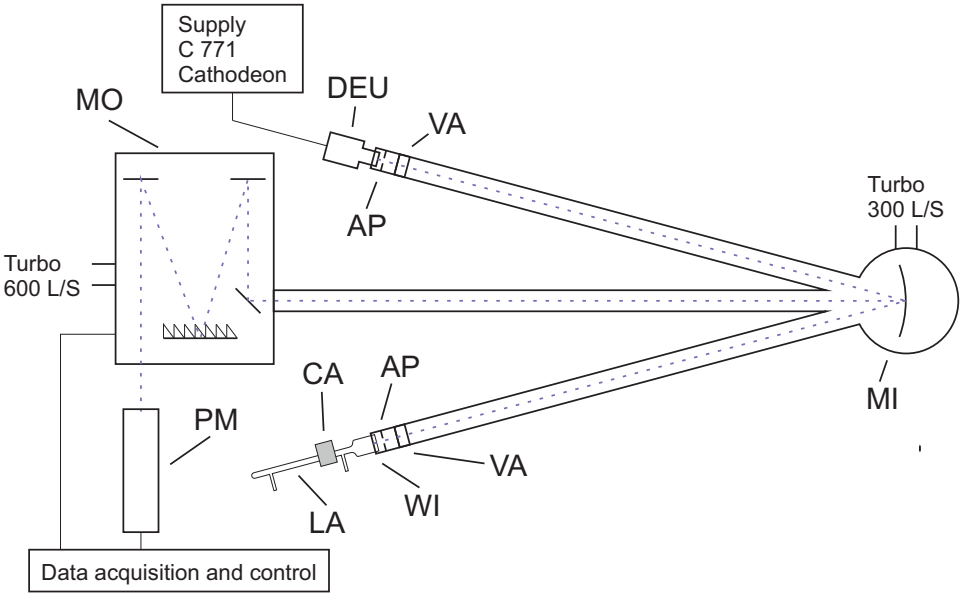

Figure 3.2: Experimental set-up at the INP Greifswald for VUV measurements, (DEU): Physikalisch Technische Bundesanstalt (PTB) calibrated D_2 lamp, (AP): Aperture, 0.6 mm (diameter), (VA): Valve, (MI): Mirror, f= 1.5 m, (WI): MgF_2 window, (PM): Photomultiplier, (MO): VUV-Monochromator (VM-505 Acton Research); 0.5m, 1200g/mm, (LA): Microwave Discharge Hydrogen-flow Lamp, (CA): Microwave Evenson cavity.

3.2.3 *Photon flux measurements*

The conversion of spectral radiance ($\mu W\ Sr^{-1}\ mm^{-2}\ nm^{-1}$) to photon flux at the sample location (photon $cm^{-2}\ s^{-1}$) is far from trivial. This is true even when all the dimensions of the set-up are known. In the Greifswald set-up only a small fraction of the plasma contributes to the light passing through the pinhole (diameter 0.6 mm); extrapolating to the full plasma introduces a large error and assumes that the plasma is homogeneous. Therefore, a set of complimentary VUV photon flux measurements of the MDHLs at various settings have been performed on a small set-up specifically constructed for this purpose in Leiden. It consists of a calibrated photodiode, shutter valve, and MgF_2 window with connection piece for the MDHL. The photodiode is a 1 cm^2 NIST calibrated AXUV-100, of which the photocurrent is measured using a Keithley 485 autorange picoammeter. The distance between the MgF_2 window and photodiode is 31 cm. The entire set-up is evacuated to a pressure of 10^{-2} mbar.

The photodiode is used to measure the total flux emitted by the MDHL. This type of photodiode has a low band gap of 1.12 eV and is therefore also sensitive to visible light. The contribution of visible light to the photocurrent has to be subtracted. Flux measurements are thus performed with and without a KBr window in the optical path. This window blocks any radiation below 240 nm and has 90% transmission above this wavelength, up to 1000 nm. By subtracting the visible response from the total photocurrent of the diode, corrected for the absorption of KBr, the photocurrent in the range between 115 to 240 nm can be determined. This yields the total energy in this spectral range, and combined with the spectrum obtained at the calibrated set-up in Greifswald, the photocurrent per wavelength can be determined. It must be noted that the energy recorded in the range 115-

240 nm is assumed to be equal to the energy in the range 116-220 nm, since no hydrogen emission is present from 220 to 240 nm. The transmission of the MgF_2 window between 115 and 116 is small. The calibrated spectrum is then converted to units of photons sr^{-1} mm^{-2} nm^{-1} and normalized to an integrated value of one. Next, the measured total VUV photocurrent is assigned proportionally to each wavelength by the normalized spectrum. This results in a wavelength dependent photocurrent that can be converted to a wavelength dependent photon flux according to equation 5,

$$I(\lambda) = \frac{i(\lambda)}{e \cdot \eta(\lambda)} \tag{5}$$

where $I(\lambda)$ is the wavelength dependent photon flux in photon cm^{-2} s^{-1}, $i(\lambda)$ the photocurrent, e the electron charge, and η (λ) the detection efficiency. The resulting wavelength dependent photon flux can be integrated to obtain the total photon flux of the lamp. Absolute Lyman-α and molecular emission photon fluxes are determined by integrating the 120-124 and 155-165 nm regions, respectively. In our spectra more emission from molecular hydrogen transitions can be seen outside the 155-165 nm region, especially at shorter wavelengths between 130-155 nm. However, the molecular emission peaks at 158 and 161 nm account by far for most of the emission and are therefore considered to be most sensitive to changes in the lamp settings.

Lyman-α and molecular emission fluxes are normalized to 100% of the total flux of the spectrum in order to visualize trends in the contribution of certain spectral regions. The remaining part of the spectrum is discussed as well. The 2σ error is determined from 15 individual measurements performed at identical settings throughout the measurement run. Errors are found to be $\pm$11% in the total photon flux, $\pm$4% in the Lyman-α contribution, $\pm$1% in the molecular emission contribution and $\pm$3% in the remaining emission contribution.

3.2.4 *CryoPAD II*

The Cryogenic Photoproduct Analysis Device II (CryoPAD II) is used to experimentally test the MDHL SED calibrations on interstellar ice analogues. The set-up is an upgraded version of the system described by Öberg et al. (2007). Ices are grown on a gold coated 'cold finger' that is mounted on top of a UHV chamber (5×10^{-11} mbar) through directed deposition. A closed-cycle helium cryostat realizes temperatures as low as 17 K and a temperature regulator (Lakeshore) allows accurate temperature settings. Ice thicknesses are determined using isothermal desorption techniques. Also mounted onto the chamber is the MDHL with a MgF_2 window to sample distances of 16 cm. The ice diagnostics upon VUV irradiation are realized both spectroscopically and mass spectrometrically. The light of an Agilent FTIR 660 spectrometer (500-4000 cm^{-1}, 2.0 cm^{-1} resolution) is guided in reflection modus onto a MCT detector to obtain RAIR (reflection absorption infrared) spectra. The entire IR beam path is purged with water-free dry air. Perpendicular to the IR beam, a Pfeiffer QMA200 Quadrupole Mass Spectrometer (QMS) is mounted to sample gas phase species that are emitted from the ice surface. This construction allows the photoprocessing of the ice upon VUV irradiation to be studied in situ and in real time. Details of the methods used have been described in Ioppolo et al. (2014) and Linnartz et al. (2015).

3.3 RESULTS

3.3.1 *Photon flux*

The most commonly used settings for either an F- or T-type MDHL are 0.41 mbar pure hydrogen pressure, at an input power of 100 W. We take the output generated by the T-type lamp as standard. Photon fluxes obtained from other experiments are normalized to this value for the majority of the data.

The spectrum of the lamp for these settings is shown in figure 3.3. Following the method described in section 3.2.3 using a calibrated photodiode, a total VUV photocurrent of 1.6 ± 0.2 μA is measured for the standard T-type lamp at a distance of 31 cm (MgF_2 window to photodiode). From this current, a photon flux of $(9 \pm 2) \cdot 10^{12}$ photons s^{-1} cm^{-2} is derived. Uncertainties in photo current and total flux determine the error in this value. The Lyman-α contribution to the total output is 36%, the molecular emission between 155 and 165 nm contributes 19% to the total output and the remaining emission of the lamp has a contribution of 45%. The remaining emission consists of all the output between 116 and 220 nm, excluding what is present in Lyman-α and the molecular part.

Based on the irradiance measurements performed in Greifswald, assuming a homogenous circular emitting source at the position of the aperture, we have calculated the photon flux. This leads to a total VUV photon flux at the photodiode position of $\sim 1.3 \cdot 10^{13}$ photons s^{-1} cm^{-2}, within a factor of two agreement with the value acquired in the direct flux measurement in Leiden.

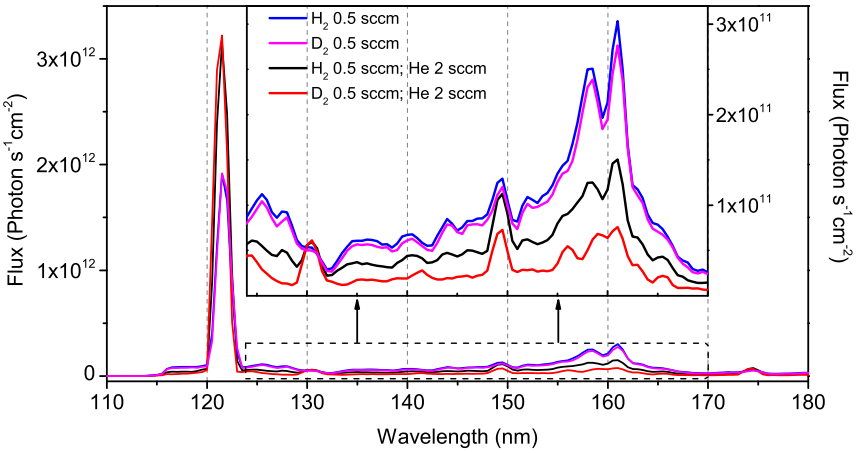

Figure 3.3: VUV spectra in the 110 − 180 nm range of a T-type geometry MDHL, the H_2/D_2 partial pressure is kept at 0.41 mbar. The effect of adding Helium with the H_2 or D_2 is clearly shown. Photon flux (y-axis) estimations are based on NIST photodiode measurements. Emission at ~ 130, ~ 149, and ~ 175 nm indicate traces of oxygen and nitrogen.

3.3.2 *H_2 pressure dependence*

In figure 3.4, the response of an F-type MDHL is plotted as a function of hydrogen pressure. The total flux is normalized with respect to the standard settings of the T-type MDHL. The relative contributions of Lyman-α (120-124 nm), molecular emission (155-165 nm),

and remaining emission is presented as well. Clearly visible at 0.41 mbar H_2 is a maximum in the total flux. For this pressure, the contribution of the Lyman-α band reaches the maximum as well, while the contribution in molecular emission is still significantly high. The remaining emission clearly has a local minimum at this pressure. At higher H_2 pressure, above 1 mbar, the total flux gradually decreases. It starts increasing again above 4 mbar. Lyman-α gradually decreases to zero for pressures above 0.41 mbar. The molecular emission shows a similar trend up to 4 mbar. At this point the molecular contribution steeply increases again and is responsible for the overall increase in total flux.

In summary: higher H_2 pressures (with respect to the standard settings) favour emission in the 160 nm region, whereas pressures between 0.4-0.8 mbar are better for Lyman-α emission.

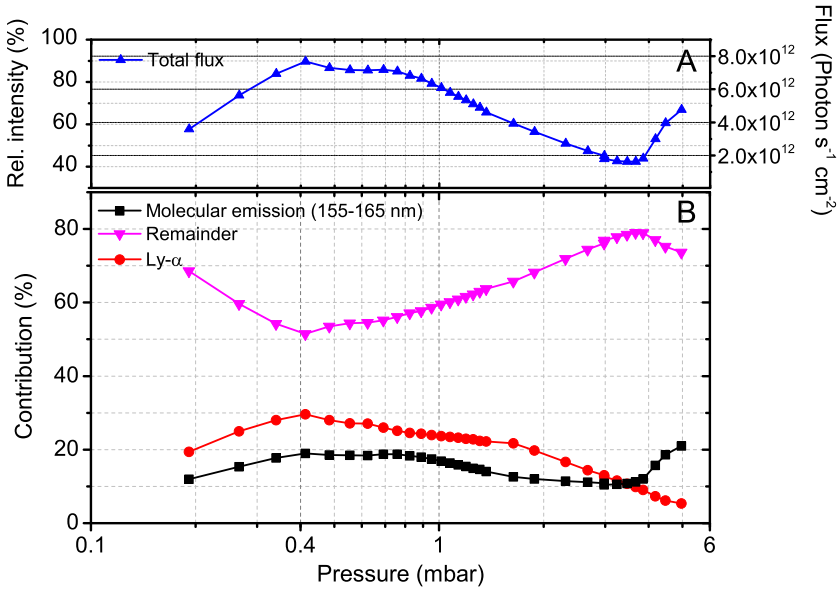

Figure 3.4: Total flux **A)** and spectral contribution **B)** as a function of H_2 pressure dependence of a F-type MDHL for standard settings. The relative intensity (left axis) is normalized to 100% of the standard T-type MDHL, photon flux (right axis) estimations are based on NIST photodiode measurements.

3.3.3 *Mixtures and different gasses*

Adding helium to hydrogen in a MDHL can have a significant influence on the SED and flux (Holländer & Wertheimer, 1994; Benilan et al., 2011; Chen et al., 2014; Cook et al., 2014; Es-sebbar et al., 2015). This is illustrated in figure 3.5A, which shows a decline in the total flux moving to higher concentration of helium admixtures. However, a dependence on the H_2 pressure used in the mixture is also seen. The general trend is comparable with the flux variation in pure H_2 where flux decreases towards higher pressure. In figure 3.5B, the spectral contribution is depicted for different H_2 pressures (0.41, 0.59, and 0.76 mbar). Within the error bars, the spectral contributions measured at different H_2 pressures overlap, confirming that in this pressure regime the amount of He is the dominant source of spectral change.

The addition of He to H_2 (and D_2 as will be discussed below) significantly alters the spectral emission pattern. By adding 2 sccm of He, the spectral purity of Lyman-α increases by a factor of ~ 1.65 from $35-40\%$ to $60-65\%$ while the total flux is nearly constant. The helium has a quenching effect on the molecular hydrogen, while increasing the effective Lyman-α flux.

As more He is added to H_2, the Lyman-α and molecular emission contributions reach a maximum and minimum, respectively, and remain at a stable level. In contrast to the spectral contributions, the total photon flux peaks around an H_2:He 1:2 mixing ratio and slowly decreases for higher amounts of helium.

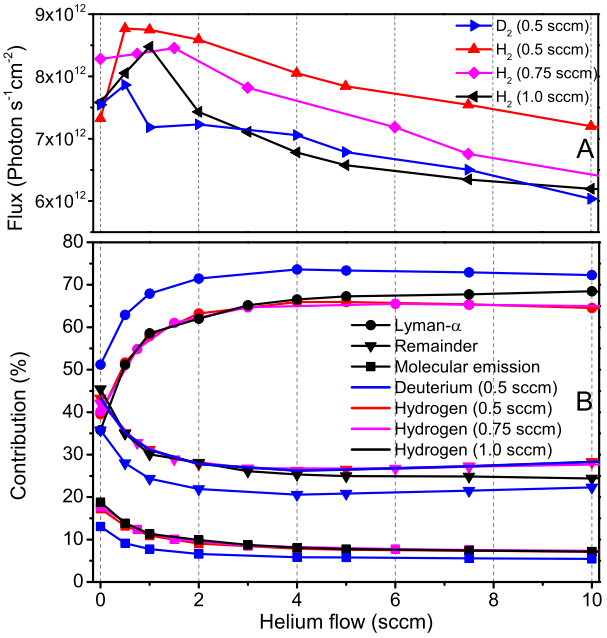

Figure 3.5: Flux dependance **A)** and spectral contribution **B)** of H_2 or D_2 as function of helium flow. Different fixed molecular hydrogen flows are shown (0.5, 0.75, and 1.0 sccm), resulting in 0.41, 0.59, and 0.76 mbar as a function of the helium flow rate. Additionally, D_2 in He is depicted (0.5 sccm /0.41 mbar).

Further alteration of the MDHL output can be accomplished by changing from H_2 to D_2 mixed with helium. This results in the highest contribution (up to $\sim 75\%$) of Lyman-α and lowest molecular emission and remaining contributions. The photon flux is reduced by roughly 15% compared to 0.41 mbar hydrogen mixed in helium, however. The corresponding VUV spectra are shown in figure 3.3.

Similar to the 1:15 H_2:He mixing ratio shown in Chen et al. (2014), we find a substantial effect of helium addition to hydrogen. A different mixing range has recently been evaluated in Es-sebbar et al. (2015), but extrapolating our settings to theirs seems to yield a comparable trend in photon flux decrease. The changing H_2 concentration might be the explanation for the increase in Lyman-α contribution. From the extended measurements performed in this article more trends become apparent. At higher ad-mixing of helium, the total flux decreases while the spectral purity of Lyman-α does not increase further. We conclude that the highest observed contribution of Lyman-α emission, is realized for D_2 in He.

3.3.4 *MDHL power dependence*

The microwave (MW) cavity input power determines the strength of the microwave field used in the MDHL, and thus directly influences how intensely the plasma is excited. This may also effect the SED. So far, three studies have been reported that focus on the MW dependency. Cottin et al. (2003) presented flux measurements over a limited range, from 30 to 80 W. Cruz-Diaz (2014) presented data about the peak intensities at Lyman-α, 157.8 nm and 160.8 nm, for MW powers ranging from 55 to 90 W. Finally, Es-sebbar et al. (2015) conducted a wavelength dependent study in combination with actinometry of the MW power on H_2:He mixtures. All three of the studies hint towards a linear behaviour between flux and MW input power. This is confirmed in our study. Figure 3.6 shows the relative output of an F-type MDHL at 0.41 mbar hydrogen versus microwave cavity input power, in the range of 50 to 130 W. Up to 110 W, the total photon flux increases linearly with input microwave power. Above 110 W the increase in flux is not as steep, but still significant. At 130 W, the trend suggests that the flux is reaching a plateau. At this microwave power the air cooling is no longer sufficient and the temperature of the cavity starts increasing. Therefore no higher microwave power measurements were performed. The relative contributions of Lyman-α, molecular, and remaining emission are also presented in figure 3.6. As can be seen, the lamp spectrum does not follow the photon flux trend linearly, but the deviations are not substantial. This finding is different from the conclusion derived in Es-sebbar et al. (2015) for H_2:He mixtures. The molecular emission and the Lyman-α contribution have a respective minimum and maximum at 100 W input power. The relative difference is as big as 10%. In conclusion, tuning the input power between 60 and 120 W offers a way to tune the photon flux output by up to a factor of 2. With the change in power small changes in SED are also found.

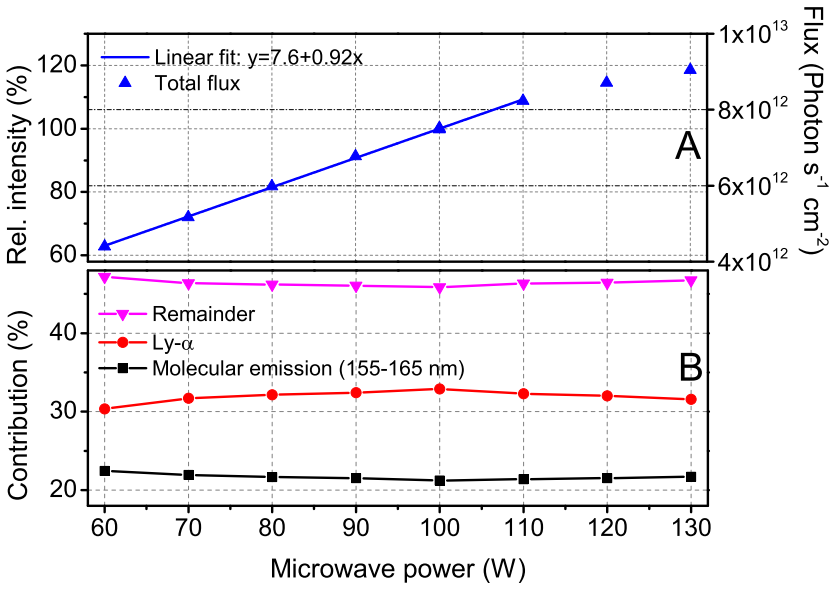

Figure 3.6: Relative flux dependance on microwave cavity input power. The total flux is normalized to the 100 W value. Lyman-α, molecular emission and remainder are given as percentages of the total flux. Corrected for time dependent behaviour.

3.3.5 *Pumping efficiency in F- and T-type MDHLs*

Comparative measurements between an F- and T-type MDHL have been performed. Under identical settings the output was measured for a number of hydrogen pressures ranging from 0.24 to 0.7 mbar. In figure 3.7 an example is presented for a hydrogen pressure of 0.41 mbar.

The T-type lamp is found to increase the Lyman-α emission by 30% on average, compared to the F-type MDHL. At the same time the molecular hydrogen emission remains identical for the F- and T-type MDHL. A total photon flux increase is also observed for the T-type lamp, which can be explained by the increase in Lyman-α emission. The increase of this particular atomic hydrogen line was also reported by Chen et al. (2014) for a pressure of 0.4 torr (0.53 mbar). They found an increase in Lyman-α when using a T-type MDHL of more than 100% compared to an F-type lamp as well as a decrease in molecular emission. These findings are not fully in line with the results in the present study. Chen et al. (2014) suggested that different pumping efficiencies were responsible for the difference in spectral output of the F- and T-type MDHLs. The T-shape geometry ensures that gasses can be more easily evacuated from the MDHL. This in turn limits collisional de-excitation of excited atomic hydrogen and therefore an increase in Lyman-α output is seen. Building on this argument, using different pumping capacities on the same lamp should make it possible to reproduce this effect. This can be achieved by using different types of pumps, for example a scroll pump and rotary vane pump. Respectively, these pumps are able to reach a base pressure in the low 10^{-3} and low 10^{-2} mbar region and have a pumping capacity of 285 l/min and 300 l/min for air. In addition, it is known that scroll pumps do not pump hydrogen as efficiently as oil-based rotary vane pumps.

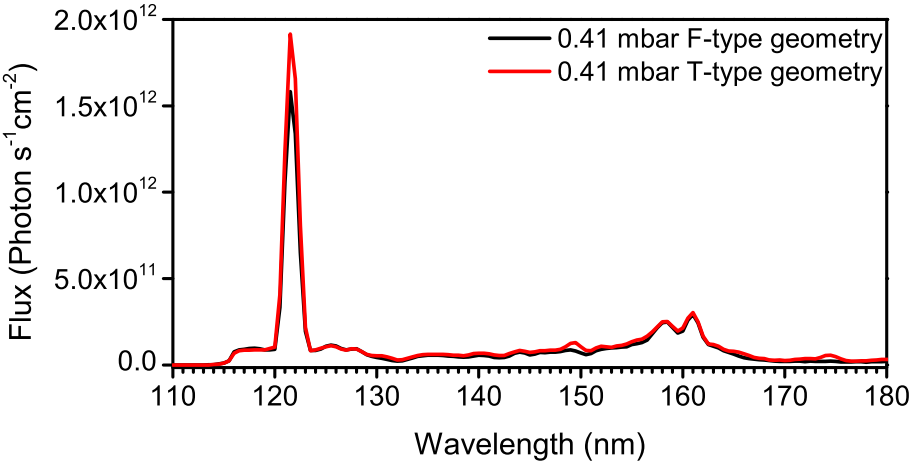

Figure 3.7: VUV spectra in the 110-180 nm range of different geometry MDHLs (F- and T-types) at a molecular hydrogen pressure of 0.41 mbar.

Two sets of measurements were performed with an F-type lamp running at various H_2 pressures, while being pumped by either a scroll pump or a rotary vane pump. Although the input pressure is identical in both sets of experiments, a pressure difference between the two pumps was observed on the gauge at the pump side. Pressures are between 6 and 60% lower for the rotary vane pump, confirming that the rotary vane pump removes hydrogen more efficiently from the MDHL than the scroll pump.

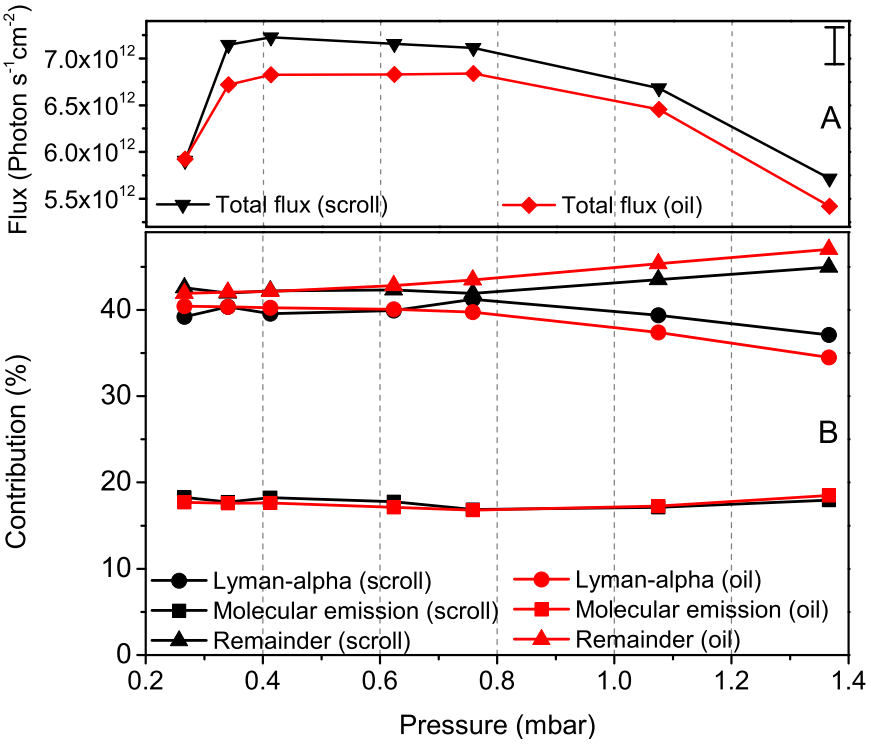

Figure 3.8: Lyman-α (circles), molecular emission (squares), remainder (triangles) contribution, and normalized total photon flux (top) for various pressures with different pumps. The oil pump (black) gives a lower photon flux than the scroll pump (red), but the contributions are virtually identical.

The VUV spectra, shown in figure 3.8, show no significant change in the spectral distribution of the lamp output for the two different pumps. Only the total photon flux output is higher for the measurements with the scroll pump. Therefore the pumping efficiency cannot explain the differences in spectral distribution between an F- and T-type lamp. It is not fully clear what causes this difference in Chen et al. (2014), because for similar settings the effect is not found here. It could be caused by the slightly different geometries of the lamps.

In conclusion, choosing a T-type cavity can be beneficial when higher Lyman-α and total flux is required. Although the spectral distribution is not expected to change for different pumping efficiencies, the total photon flux can be slightly affected. Therefore, when running a series of experiments, the same pumping system should always be used.

3.3.6 *Distance dependence*

In this study measurements are performed to determine the influence of the microwave cavity positioning on the output spectrum. The measurements are done at cavity positions of 9.0, 7.3, and 5.5 cm from the MgF_2 window for H_2 flow pressures of 0.41, 0.59, and 0.76 mbar (see figure 3.9). The overall trend is that the total photon flux decreases slightly while moving the cavity away from the MgF_2 window. Additionally, the spectral energy distribution does show minor changes as well. The percentage-wise contribution of Lyman-

α increases and the molecular emission contribution decreases when the cavity is moved towards the MgF_2 window. Although this is small and within the error, this effect is observed for all pressures studied.

Although it is a small effect (for the distances studied here), the change in photon flux is interesting. The limited data set available scales with an isotropic r^{-2} decrease, suggesting that the MW cavity defines a point source. The change in spectral output may be related to a higher column density of rest gasses in between the plasma and window when increasing the distance, affecting the SED in a wavelength dependent way. At this stage it is not possible to say more; the overall effects are small. Nevertheless, as the position does matter, keeping the cavity on a fixed position during a set of experiments is recommended.

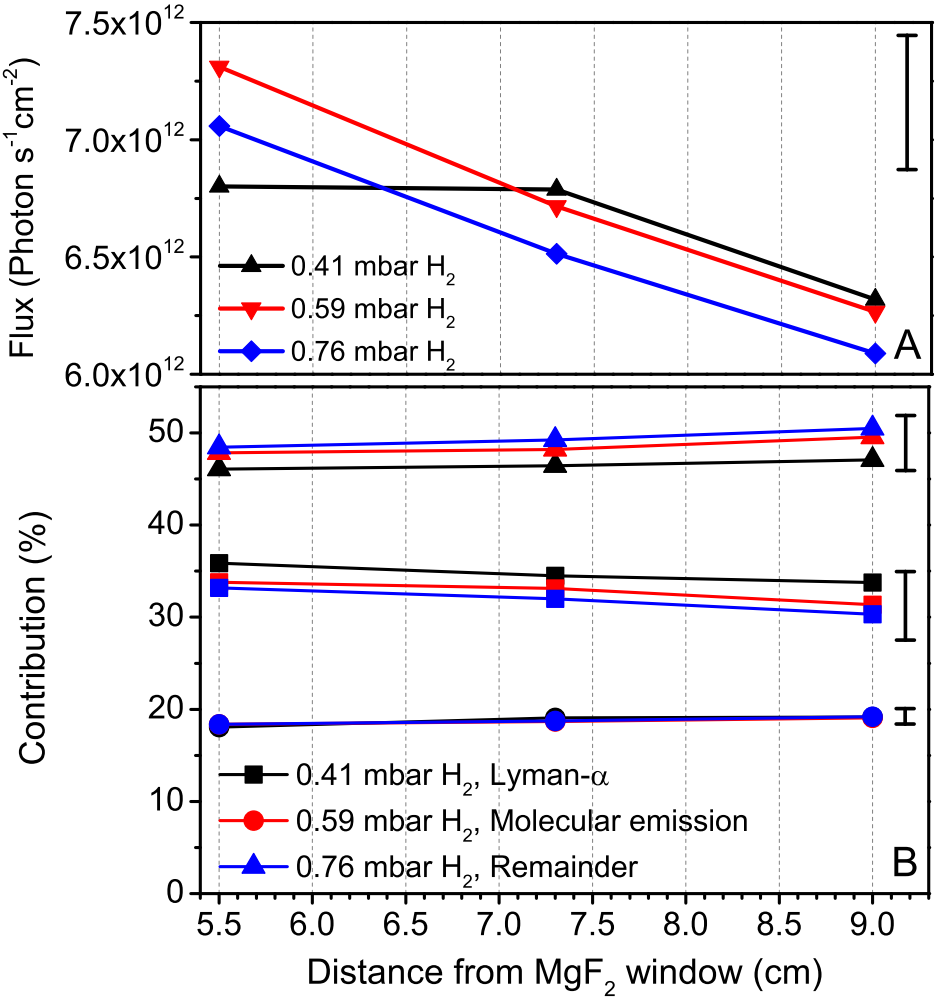

Figure 3.9: Variations in spectral output depending on cavity location, 0.41 mbar (black), 0.59 mbar (red), and 0.76 mbar (blue) H_2 flow pressure. Lyman-α (squares), molecular emission (circles), and remainder of the VUV spectrum are shown (triangles).

3.3.7 *Practical issues*

In addition to the systematic dependences discussed before, there are also a number of very practical issues that should be taken into account when operating the MDHL. The most prominent practical issues running MDHLs involve stability over time (section 3.3.7.1) and the effect of degradation of the MgF_2 window (section 3.3.7.2).

3.3.7.1 *MDHL stability over time*

In many of the previous studies using MDHLs it was found that these exhibit changes in the output photon flux over operating time. Two important contributors to this effect are thermal settling of the lamp and degradation and pollution of the transmission window (Warneck, 1962; Chen et al., 2014). To determine the stability of our lamp spectrum over time, a T-type MDHL was run at 0.41 mbar H_2 for an hour while taking a spectrum every 5 minutes (see figure 3.10). The first spectrum was taken immediately after turning on the MDHL. In the first 5 minutes a drop in total photon flux is seen, after which the output linearly decreases. This decrease is mainly caused by a quick drop in molecular emission. The linear decrease in flux is similar to that reported by Chen et al. (2014); however, no stable region is reached, possibly owing to the shorter duration of the experiment; one hour in this work and two and a half hours in Chen et al. (2014).

More interesting are the Lyman-α and molecular emission contributions to the total flux. These are found to remain at a stable level after the first 5 minutes of lamp operation, which guarantees that spectral properties of the lamp are directly proportional to its photon flux.

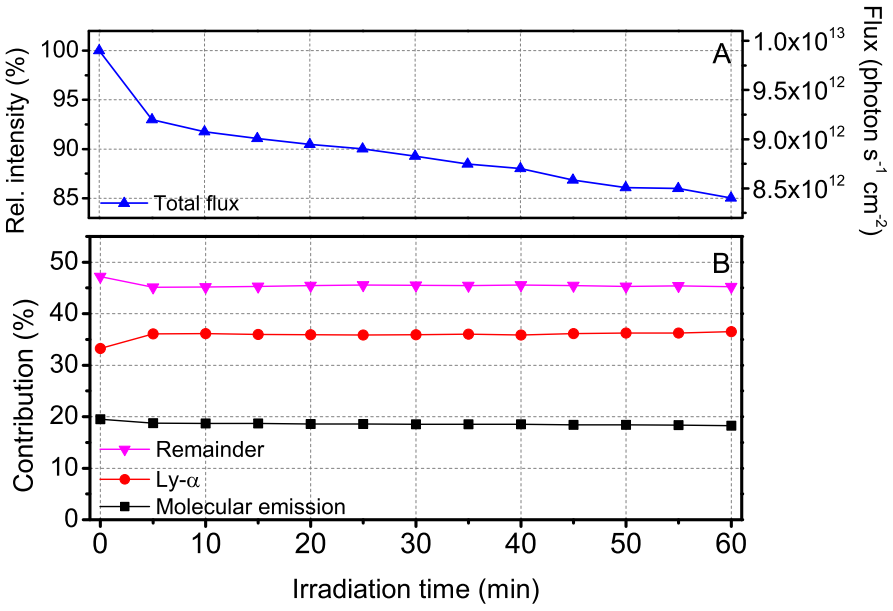

Figure 3.10: Relative flux decrease over time, combined with the relative contribution of Lyman-α, molecular, and remaining emission for standard MDHL settings, using a T-type lamp.

This result is surprising, since Warneck (1962) found that the contribution of the Lyman-α component decreases more rapidly than the molecular contribution. This is possibly due to differences in the way the SEDs are determined. Warneck (1962) made use of a nickel photocell to detect the 120-130 nm range and ozone actinometry for the 135-185 nm region. These broadband techniques are not suitable for distinguishing wavelength dependences and consequently only provide information on the overall flux. For general lamp operation starting the irradiation experiments after the lamp has settled for 10 to 15 minutes is recommended. In this way the photon flux and spectral fluctuations do not play a dominant role in the experiment. After this period the spectral contributions will remain stable and therefore it is sufficient to only trace variations in the photonflux.

3.3.7.2 *Effects on the MgF_2 window*

As already suggested in paragraph 3.3.7.1, pollution of the MgF_2 window can have a big influence on the output of the MDHL. Carbon products formed in the plasma can deposit on the MDHL side of the window. Especially if the VUV lamp is being pumped with an oil-based pump, there will be oil vapours in the system that can be processed by the plasma and deposited as a residue on the window. On the vacuum chamber side, gas molecules can be adsorbed on the window, and residual gas molecules will be present in the vacuum chamber. When the lamp is in operation these molecules can be processed by the VUV field to form a residual layer. Es-sebbar et al. (2015) showed a decrease of 50% in transmission of the MgF_2 window after 8 hours of irradiation, which was ascribed to the deposition of trace species. We do not observe such a drastic decrease in transmission. However, this discrepancy could be explained by a difference in measurement technique. A third effect is the processing of the window itself. The harsh VUV output of the lamp causes structural changes of the material over time. This was shown by Warneck (1962) for LiF, and it is also likely to happen for MgF_2, although on a different time scale. These two effects, pollution and window processing, can be responsible for diminishing the flux and may cause spectral changes over longer periods of time.

It should be noted that in the Greifswald measurements, the window degradation has not been explicitly taken into account, as this would imply that the window had to be removed regularly. Instead, we expect that degradation effects along a series of measurements, focussing on one specific parameter, are negligible or much less relevant than the effect of the changing parameter under investigation.

3.3.8 *CO photodepletion measurements*

Laboratory experiments have shown that photodesorption offers an effective non-thermal mechanism that explains the detection of molecular gas phase species in low temperature regions in the ISM where these species are expected to be fully frozen out. However, the exact numbers vary between different groups, even when experimental procedures are largely identical. This has become clear, particularly for the photodesorption yield obtained for pure CO ice. Öberg et al. (2007), Muñoz Caro et al. (2010), and Chen et al. (2014) provide values of $(2.7 \pm 1.3) \cdot 10^{-3}$, $(35 \pm 5) \cdot 10^{-3}$, and $(212 \pm 3) \cdot 10^{-3}$ molecules per incident photon, respectively. These measurements have been performed with broadband MDHLs. In a monochromatic and wavelength dependent study Fayolle et al. (2011) showed that CO photodesorption occurs predominantly at longer wavelengths between 135 and 165 nm, following a desorption induced by electronic transition (DIET) mechanism. For wavelengths around Lyman-α the photodesorption is much less efficient. Therefore, different SED characteristics, specifically the Lyman-α to molecular emission band ratio, will definitely influence the overall photodesorption rate that follows from the MDHL experiments.

This is illustrated in Figure 3.11 where the corresponding SEDs of two well-characterized lamp settings are used to derive photodesorption rates.

Using CryoPAD II, a T-type MDHL is operated at 100 W and either 0.41 mbar of pure H_2 or a 1:3 H_2:He gas mixture, at a pressure of 2.13 mbar, is used. The SEDs for these settings comprise 36% and 67% of Lyman-α and 19% and 8% molecular emission, respectively, while the total flux for both settings is similar (less than $\sim 0.5 \cdot 10^{12}$ photons s^{-1} cm^{-2} difference, or about 6%, in the calibrated measurements). The vacuum UV photons impinge on thin ice layers (13 or 16 MonoLayers (MLs), 1 ML = 10^{15} molecules) of pure CO deposited on top of a 17 K gold surface; the layers are thick enough to exclude surface effects. A typical experiment lasts 2 hours. The ongoing photodepletion (the combined effect of photodesorption and photochemistry) of the CO ice over time is subsequently tracked by the decrease in the 2142 cm^{-1} CO band.

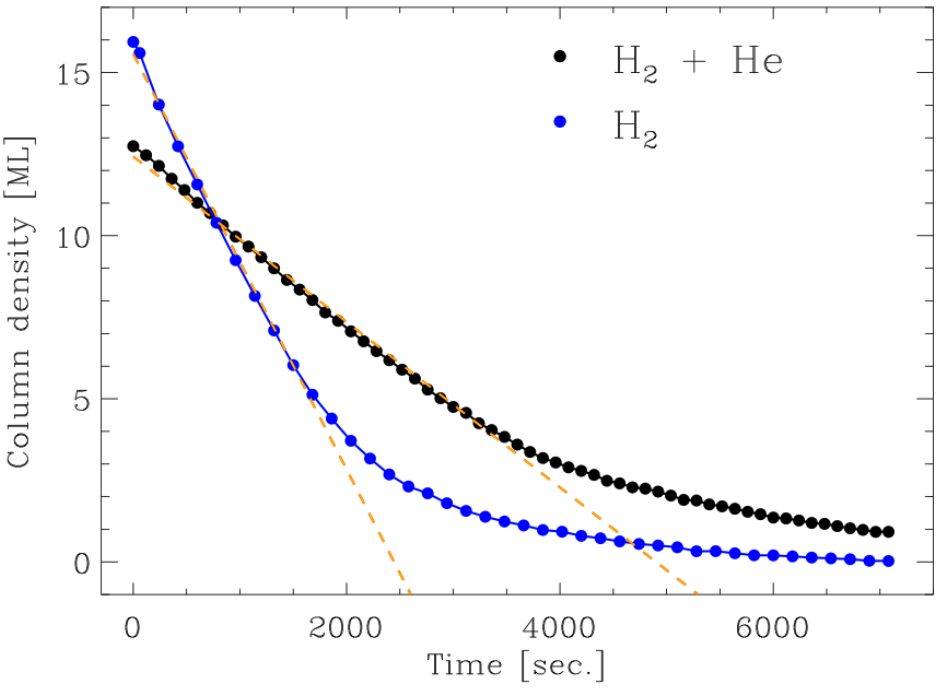

Figure 3.11: CO photodesorption of ices irradiated with either Pure H_2 at 0.41 mbar (blue) or H_2:He 1:3 (black) at 2.13 mbar.

Taking thicknesses of 5 ML or more as the regime where surface effects can be neglected, the linear fits allow a photodepletion rate to be derived. As expected from the work by Fayolle et al. (2011), an ice irradiated with light from the MDHL running on the H_2:He mixture (suppressed 160 nm emission) photodepletes less rapidly than the ice irradiated with pure H_2 that exhibits a molecular emission that is roughly two times bigger. Obviously, this photodepletion value is different for the different lamp settings, fully in agreement with the main findings of the work presented in this paper. It also may explain, at least to some extent, the deviations found in the different photodesorption studies in agreement with Chen et al. (2014). It is for this reason that we stress how important it is to record the SEDs in situ. Other artefacts might also be at play; it is likely that other photo induced effects affect the final values, (wavelength dependent) chemical processes forming CO_2, for

example, that in turn may photodesorb (wavelength dependent, see Fillion et al., 2014). The two curves in the figure yield a photodepletion rate of $(6 \pm 3) \cdot 10^{-3}$ and $(3 \pm 1) \cdot 10^{-3}$ ML s^{-1} for H_2 and the H_2:He mixture, respectively. It will take a greater effort to bring all experimental numbers in line, but obviously an important uncertainty has now been characterized.

Besides quantitative issues, a changing SED may also affect the outcome of many chemical studies performed over the past decades; different molecules may react resonantly with different emission bands, and particularly higher energetic photons may cause bonds to cleave more easily. With the information provided here such dependencies can now be studied relatively easily.

Table 3.1: Parameter influences

Influence	Effect on SED (Lyman-α)	Effect on SED (Molecular Emission)	Effect on flux (photon cm^{-2} s^{-1})
Pressure	Large effect ~ 30%	Large effect ~ 15%	Large effect ~ 30%
Power	Limited effect ~ 3%	Limited effect ~ 3%	Large effect ~ 50%
Helium	Large effect ~ 100%	Large effect ~ 50%	Limited effect ~ 5%
Deuterium	Moderate effect ~ 10%	Moderate effect ~ 10%	Moderate effect ~ 15%
F- vs. T-type	Moderate effect ~ 20%	Limited effect	Moderate effect ~ 20%
Cavity	Limited effect ~ 3%	Limited effect ~ 3%	Limited effect
Time	No effect	No effect	Limited effect ~ 7%

3.4 CONCLUSIONS

In this work the influence of various running conditions on both flux and SED of the microwave discharge hydrogen-flow lamp has been studied. The main findings are summarized in table 3.1. The conclusions of this work are:

1. The effects of hydrogen pressure, ad-mixing helium, exchanging hydrogen for deuterium, microwave power, pumping efficiency, cavity position, and practical issues such as stability over time need to be taken into account.

2. The relative contribution of Lyman-α to the emission profile of the MDHL can be increased by up to 65% when helium is added to the hydrogen. Further spectral purity of Lyman-α of up to nearly 75% can be achieved by exchanging hydrogen for deuterium. Alternatively, high percentages of molecular emission can be generated by increasing the hydrogen pressure.

3. Recommendations are given on how to operate the MDHL at the highest efficiency and consistency. They include allowing sufficient time for the settling of the lamp, using a fixed cavity position, and accounting for pollution on the lamp window.

4. Variations in the SED can, to a certain extent, explain the differences in the literature among different laboratory experiments. However, it seems unlikely that it will explain order of magnitude differences.

5. It is important to characterize the SED and photon flux in situ, preferably with a combination of monochromator and calibrated photodiode.

BIBLIOGRAPHY

Baratta, G. A., Leto, G., & Palumbo, M. E. 2002, Astron. Astrophys., 384, 343
Benilan, Y., Gazeau, M.-C., Es-Sebbar, E.-T., et al. 2011, in EPSC-DPS Joint Meeting 2011, 1317
Chen, Y.-J., Chuang, K.-J., Muñoz Caro, G. M., et al. 2014, Astrophys. J., 781, 15
Cook, A. M., Mattioda, A. L., Quinn, R. C., et al. 2014, Astrophys. J. Suppl. Ser., 210, 15
Cottin, H., Moore, M. H., & Bénilan, Y. 2003, Astrophys. J., 590, 874
Cruz-Diaz, G. A. 2014, PhD thesis, Centro de Astrobiología, Universidad Autonoma de Madrid
Cruz-Diaz, G. A., Muñoz Caro, G. M., Chen, Y.-J., & Yih, T.-S. 2014a, Astron. Astrophys., 562, A119
Cruz-Diaz, G. A., Muñoz Caro, G. M., Chen, Y.-J., & Yih, T.-S. 2014b, Astron. Astrophys., 562, A120
Davis, D. & Braun, W. 1968, Appl. Opt., 7, 2071
Es-sebbar, E.-t., Bénilan, Y., Fray, N., et al. 2015, Astrophys. J. Suppl. Ser., 218, 19
Fayolle, E. C., Bertin, M., Romanzin, C., et al. 2011, Astrophys. J. Lett., 739, L36
Fayolle, E. C., Bertin, M., Romanzin, C., et al. 2013, Astron. Astrophys., 556, A122
Fillion, J.-H., Fayolle, E. C., Michaut, X., et al. 2014, Farad. Discuss., 168, 533
Foest, R., Kindel, E., Lange, H., et al. 2007, Contrib. Plasma Phys., 47, 119
Fulvio, D., Brieva, A. C., Cuylle, S. H., et al. 2014, Appl. Phys. Lett., 105, 014105
Gerakines, P. A., Schutte, W. A., & Ehrenfreund, P. 1996, Astron. Astrophys., 312, 289
Groth, W. 1937, Z. Phys. Chem., 37, 307
Henderson, B. L. & Gudipati, M. S. 2015, Astrophys. J., 800, 66
Holländer, A. & Wertheimer, M. 1994, J. Vac. Sci. Technol., A, 12
Ioppolo, S., Fedoseev, G., Minissale, M., et al. 2014, Phys. Chem. Chem. Phys., 16, 8270
Islam, F., Baratta, G. A., & Palumbo, M. E. 2014, Astron. Astrophys., 561, A73
Lange, H., Foest, R., Schafer, J., & Weltmann, K.-D. 2009, IEEE Trans. Plasma Sci., 37, 859
Leto, G. & Baratta, G. A. 2003, Astron. Astrophys., 397, 7
Linnartz, H., Ioppolo, S., & Fedoseev, G. 2015, Int. Rev. Phys. Chem., 34, 205
Loeffler, M. J., Baratta, G. A., Palumbo, M. E., Strazzulla, G., & Baragiola, R. A. 2005, Astron. Astrophys., 435, 587
Muñoz Caro, G. M., Jiménez-Escobar, A., Martín-Gago, J. Á., et al. 2010, Astron. Astrophys., 522, A108
Muñoz Caro, G. M., Meierhenrich, U. J., Schutte, W. A., et al. 2002, Nature, 416, 403
Öberg, K. I., Fuchs, G. W., Awad, Z., et al. 2007, Astrophys. J. Lett., 662, L23
Warneck, P. 1962, Appl. Opt., 1, 721
Watanabe, N., Mouri, O., Nagaoka, A., et al. 2007, Astrophys. J., 668, 1001
Westley, M. S., Baragiola, R. A., Johnson, R. E., & Baratta, G. A. 1995, Nature, 373, 405

4

METHANE ICE PHOTOCHEMISTRY AND KINETIC STUDY USING LASER DESORPTION TIME-OF-FLIGHT MASS SPECTROMETRY AT 20 K

The ice photochemistry of pure methane (CH_4) is studied at 20 K upon VUV irradiation from a microwave discharge H_2 flow lamp. Laser Desorption Post-Ionization Time-Of-Flight Mass Spectrometry (LDPI TOF-MS) is used for the first time to determine branching ratios of primary reactions leading to CH_3, CH_2, and CH radicals, typically for fluences as expected in space. This study is based on a stable end-products analysis and the mass spectra are interpreted using an appropriate set of coupled reactions and rate constants. This yields clearly different values from previous gas phase studies. The matrix environment as well as the higher efficiency of reverse reactions in the ice clearly favor CH_3 radical formation as the main first generation photoproduct.

J.-B. Bossa, D. M. Paardekooper, K. Isokoski, and H. Linnartz, *Methane ice photochemistry and kinetic study using laser desorption time-of-flight mass spectrometry at 20 K*, Phys. Chem. Chem. Phys., 17, (2015) 17346.

4.1 INTRODUCTION

At the present time, more than 180 different species not including isotopologues have been observed in interstellar and circumstellar media. Models of interstellar chemistry involving both gas-phase and solid-phase reactions are employed to understand the complex chemical formation route of the observed species and to predict their abundances in the regions where they reside (van Dishoeck, 2014). The reliability of these models depends on the accuracy of the reaction rate coefficients that are contained in databases for use in astrochemistry; e.g., UMIST Database for Astrochemistry (McElroy et al., 2013), NIST Chemical Kinetics Database (Manion et al., Release 1.6.8, Data version 2013.03, National Institute of Standards and Technology, Gaithersburg, Mary- land, 20899-8320, 2013, http://kinetics.nist.gov/), KInetic Database for Astrochemistry (Wakelam et al., 2012). For the gas phase, accurate data have been derived in the laboratory, but in the solid phase such data are still largely lacking (Wakelam et al., 2010). Moreover, processes on icy grains cannot be considered to be isolated processes. Nevertheless, it is a long-standing problem that in the absence of experimental data on ice films, astrochemical models use gas phase reaction rate coefficients instead, which are often extrapolated beyond measured temperatures, to determine the abundance of reactants and products in interstellar ices during the different stages of star formation. This may lead to considerable errors.

A few laboratory studies have been reported that mention branching ratio estimations for photochemical experiments simulating UV fluences as expected for typical dense cloud lifetimes (Gerakines et al., 1996; Öberg et al., 2009). For some pure ices, backward reactions that convert products to the initial reactant are so fast that forward reactions cannot be investigated directly. For example, the solid-state methylamine (CH_3NH_2) photodissociation pathways have been unraveled by using carbon monoxide (CO) as an H atom scavenger (Bossa et al., 2012a). Genuine kinetic studies involving energetic processing of ices are difficult to perform and need accurate and time resolved surface science techniques. The extensive and systematic study of thermal reactivity in binary and ternary ice mixtures together with diffusion measurements have already provided kinetic parameters (Theulé et al. (2013); Mispelaer et al. (2013) and references therein). Hydrogen – deuterium substitution experiments on pure methylamine ice (Oba et al., 2014) and energetic electron irradiations on a pure methane (CH_4) ice (Bennett et al., 2006) and on a NH_3:CH_4 binary ice mixture (Kim & Kaiser, 2011) have been kinetically investigated by combining reflection absorption infrared spectroscopy (RAIRS) and mass spectrometry during temperature programmed desorption experiments (TPD). In these latter studies, the quantitative analysis relies on the column densities of both reactants and products as a function of the different energetic processing times. These values are generally determined from the mid-infrared spectra by integrating – preferably – non-overlapping vibrational bands and by using the corresponding band strengths from the literature, i.e., the A-values written in cm molecule^{-1} unit. Overlapping infrared features are common when working with complex ices, i.e., composed by more than three different constituents. Band strengths and infrared band profiles are known to be strongly dependent on the ice temperature and on the ice composition (Öberg et al., 2007), thus larger uncertainties may arise when more complex species form in the ice. Intermediate species like radicals are also difficult to observe in the solid phase even when trapped at cryogenic temperatures. Only few of them are stable and can be directly observed in the mid-infrared (e.g., HCO or CH_3) (Gerakines et al., 1996; Bennett et al., 2006). Electron Paramagnetic Resonance (EPR) implemented for cryogenic materials (Toriyama & Iwasaki, 1979; Shkrob et al., 2011) should be ideal to monitor radicals during an irradiation, but this technique has, to our knowledge, not often been used in the field of laboratory astrophysics (Zhitnikov & Dmitriev, 2002). Another

suitable experimental technique that may compensates the current limitations of regular surface science techniques (e.g., RAIRS and TPD) is the Laser Desorption Post-Ionization Time-Of-Flight Mass Spectrometry (LDPI TOF-MS) (Focsa & Destombes, 2001; Gudipati & Yang, 2012). This technique allows the *in situ* analysis of small fractions of a processed ice sample at different irradiation times, thus allowing kinetic studies, as demonstrated in a recent technical review (Paardekooper et al., 2014).

The focus here is on solid methane (CH_4). Interstellar methane (CH_4) is ubiquitous and the solid phase abundances range from 1 to 5 % relative to H_2O, depending on the targeted source type (Gibb et al., 2004; Öberg et al., 2011). Gas phase methane (CH_4) photolysis is the main source of more complex hydrocarbons in the atmospheres of Titan (Wilson & Atreya, 2000; Romanzin et al., 2005) and the giant planets (Dobrijevic et al., 2003; Smith & Nash, 2006). Several reviews dedicated to the different photolysis pathways of gas phase methane in the Lyman-α wavelength region demonstrate the complex photochemistry and list contradictory results concerning the branching ratios between the various products (see Romanzin et al., 2005; Blitz & Seakins, 2012, and references therein). These differences were explained by the collisional conditions and the nature of the probed processes (Romanzin et al., 2005). In contrast to a gas phase environment, solid materials present higher densities and reduced mobilities of their constituents. Thus atoms and radicals trapped within a processed cold ice can efficiently recombine and reform the initial material. Therefore, backward reactions slow down the primary photodissociation processes and one can expect a drastically different chemical evolution scenario compared to the one observed in the gas phase studies (Okabe, 1978; Yung & Demore, 1999).

The objective of this present kinetic study is to understand – in a bottom-up approach and using the LDPI TOF-MS technique – the methane photochemistry at cryogenic temperatures and therefore in the solid phase, and to provide for the first time effective rate coefficients and branching ratios for primary processes at 20 K.

4.2 EXPERIMENTAL APPROACH

The experiments were carried out in the novel, contamination-free ultra-high vacuum (UHV) setup MATRI^{2}CES, thoroughly described in Paardekooper et al. (2014). The central unit is an UHV chamber in which thin ice samples can be grown with monolayer precision onto an off-centred gold-coated copper cylinder ending in a rectangular flat sampling edge surface. The substrate holder is mounted on a closed-cycle helium cryostat that, in conjunction with resistive heating, allows for temperature control from 20 to 300 K with a relative precision of 0.1 K (Lakeshore model 331). Only gas phase methane (CH_4, Praxair, purity 99.9995 %) is introduced into the main chamber with an aperture adjusted leak valve following a front deposition procedure. During deposition at 20 K, the substrate holder is continuously (vertically) translating back and forth to achieve a relatively flat ice growth (similar as the spray painting technique). The thickness of the ice samples is typically around 50 ML. The thickness is determined in separate experiments but with identical deposition procedures and using laser optical interference (Bossa et al., 2012b) ($\lambda = 632.8$ nm, He-Ne laser, Thorlabs HRS015) with a refractive index of 1.329 (Brunetto et al., 2008). The vacuum ultraviolet (VUV) irradiation ($\lambda > 120$ nm) is generated by a microwave discharge H_2 flow lamp (Opthos instruments) separated from the main UHV chamber by a UHV magnesium fluoride (MgF_2) window with a cut-off wavelength at 120 nm. Lamp settings during irradiation are $P_{H_2} = 7 \times 10^{-1}$ mbar, F-type quartz-lamp geometry, microwave forward power 80 %, and reflected power of 10 %. The integrated emission flux of the microwave-discharge H_2 lamp in the 120 – 200 nm wavelength range at 140 mm (from the lamp window to the sample) is $2-4 \times 10^{13}$ photons s^{-1} cm^{-2}. The spectral profile of the lamp mainly contains Lyman-α ($\lambda = 121.6$ nm) photons emitted

(~ 75%) together with the remaining $\lambda = 160$ nm photons (see Chen et al., 2014; Ligterink et al., 2015, Chapter 3). The substrate holder is directly connected to a two axis translation stage system: horizontal (y) and vertical (z) motions are allowed in order to always expose non-overlapping *fresh spots* of an ice sample to the laser desorption beam for kinetic study and for mass spectra averaging. The VUV emission is stopped, before ice diagnostics, for positioning the substrate holder at the right (y, z) coordinate. Meanwhile, we expect that radical diffusion and reactivity are efficient enough even at 20 K, especially for the methyl radical for which the diffusion is already efficient even diluted in water (Öberg et al., 2010). We assume that no reactions (i.e., upon diffusion and recombination) occurs during the laser ablation process and that the observed products are representative of the ice photochemistry prior to ablation. Partial ablations of hydrocarbon-rich cryogenic ices are achieved using the unfocused ~ 1.25 mm diameter) third harmonic beam of a Nd:YAG laser (Polaris II, New Wave Research, 355 nm, 10 Hz repetition rate, 143 mJ cm^{-2} energy density without attenuation, unpolarized). Laser desorption is used to bring species into the gas phase, generally as a desorption plume. Laser attenuation, resulting in a laser pulse energy of 8-9 mJ cm^{-2} and ion extraction time are optimised to probe the desorption plume where both clustering and chemical reactions are negligible upon desorption compared to the VUV irradiation effects. The local temperature rise where the laser hits the ice/gold interface is estimated around 600 K (El-Adawi & Elshehawey, 1986) (upper limit obtained without laser attenuation) after a 4 ns laser pulse striking the vacuum/ice/gold three-phase layered structure (Dohnálek et al., 2003; Bossa et al., 2014) at an incident angle of 30°, with a reflectivity $(R_s + R_p)/2 = 0.39$. Typically around 220 laser ablation pulses are needed to record one averaged time-of-flight spectrum with good signal-to-noise ratio. Ablated ice constituents are subsequently ionised by an orthogonal beam of electrons generated by a 70 eV electron impact ion source located underneath the UHV chamber, hence allowing laser-desorption and ionisation events occurring at the same spot. Positive ions are generated between the extraction and repeller plates of the time-of-flight system (Jordan TOF Products, Inc.) for an optimum ion transmission. After electron impact ionisation, cations with different masses are accelerated into a second UHV time-of-flight chamber/tube in reflection mode for mass-separation following the different arrival times to the 40 mm MCP detector. A 3-point internal calibration is then performed for each averaged spectrum using fragment ion peaks and/or the molecular ion peak of the initial ice material.

4.3 RESULTS

The electronic absorption spectrum of gas phase CH_4 begins for wavelengths below 140 nm (Lee & Chiang, 1983). The solid phase CH_4 absorption spectra slightly shift to shorter wavelengths compared to the gas phase (Cruz-Diaz et al., 2014), and present three non resolved absorptions near Lyman-α. Therefore, the Lyman-α photons emitted from the microwave-discharge H_2 flow lamp (and not the 160 nm photons) likely correspond to the main incident radiation susceptible to be absorbed by the pure CH_4 ice. Among the different photodissociation channels accessible near Lyman-α, three fragments (CH_3, CH_2, and CH radicals) can form stable end-products like C_2H_6, C_2H_4, and C_2H_2 hydrocarbons. The branching ratios of the solid state photodissociation pathways leading to these radicals, therefore, can be determined by monitoring the molar fractions of the three stable photoproducts together with the decrease of methane as a function of irradiation time. In the following, specific attention will be paid to hydrocarbons up to two carbon atoms only, i.e., four molecules in total namely methane, ethane, ethylene, and acetylene. Note that the different possible electronic states (singlet and triplet) of CH_2 are not distinguished in this study.

In the following the results are presented. We employed highly sensitive laser desorption post ionisation time-of-flight mass spectrometry to identify the molecular complexity emerging during the VUV irradiation of a pure CH_4 ice at 20 K. At different predefined irradiation times, i.e., 2, 4, 8, 12, 16, 24, 32, 40, 48, 56, 64, 72, 80, 88, and 96 min. (the last value corresponding to maximum 10^7 years of photolysis in dense molecular clouds), the VUV lamp is switched off and a mass spectrum is recorded. Since we are limited to nine measurements per processed ice, experiments are repeated up to four times with overlapping irradiation times as repeatability check points.

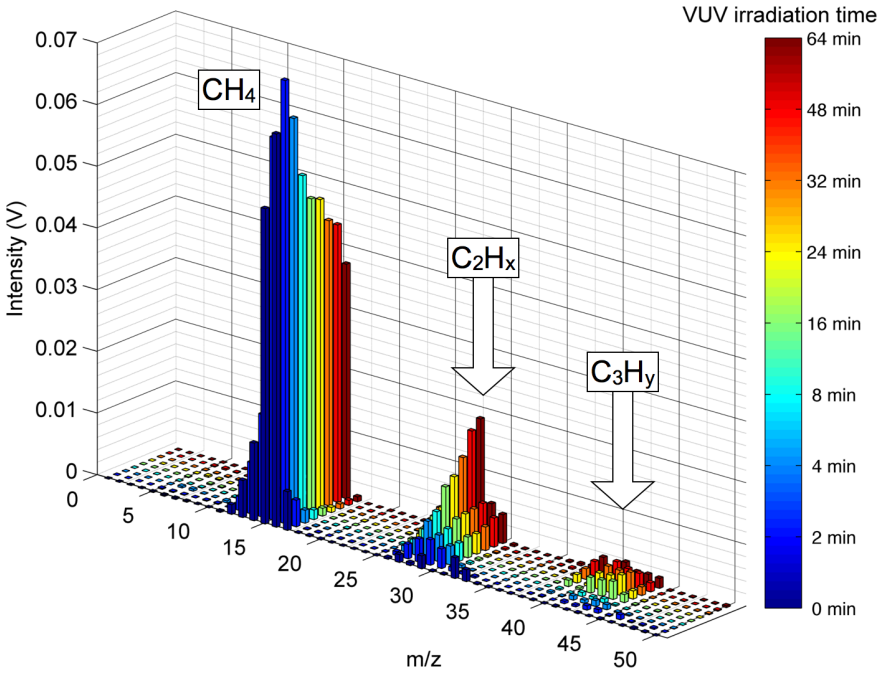

Figure 4.1: ReTOF 70 eV electron impact mass spectra sample as a function of the VUV irradiation time (color bar) of the initial (CH_4) and newly formed ice products (C_2H_x and C_3H_y), with x = 2,4,6 and y = 4,6,8.

Figure 4.1 shows a typical example of ReTOF mass spectra as a function of irradiation time (2, 4, 8, 16, 24, 32, 48, and 64 min.), with 0 min. the reference mass spectrum recorded right before starting the photolysis. The spectra display the signal intensity in Volt as a function of m/z ratios. The intensity can be directly correlated to the total counts of the ionised species coming from the laser desorption process that induces desorption of the ice constituents at well-defined irradiation time and processed ice spots. For clarity, m/z ratios are only given up to m/z 50, although very weak peaks related to more complex hydrocarbons containing up to six carbon atoms are observed (in good agreement with a recent study following an identical experimental protocol (Paardekooper et al., 2014).

The mass spectra of the unprocessed CH_4 ice (dark blue in figure 4.1) depicts low intensity mass peaks above m/z 16 related to light clusters that disappear later on. Figure 4.1 clearly shows a homologous series of straight-chained hydrocarbons, steadily appearing with irradiation time (C_2H_x and C_3H_y, with x = 2, 4, 6 and y = 4, 6, 8). The set of peaks belonging to the homologous series, generally decreases in intensity with increasing

m/z ratios, meaning that the abundances of the photoproducts decrease with molecular complexity. This is consistent with the fact that longer multi-step processes are needed to form more complex species.

In constrast to soft and selective ionisation techniques, 70 eV electron impact sources provide a large number of ions with an extensive fragmentation. Although fragmentation is useful for structure determination, it can also provide mass spectra congested with overlapping fragment peaks and barely visible molecular ion peaks, thus making the interpretation difficult. As a solution and following the quantitative approach used in Paardekooper et al. (2014), each spectrum recorded at a specific irradiation time is regarded as a composite mass spectrum of individual compounds present in the ablated material. For quantification, a fitting procedure is used that needs (i) the different reference mass spectra (Stein, 2014) of CH_4, C_2H_6, C_2H_4, and C_2H_2, and (ii) the corresponding electron impact cross sections at 70 eV (3.524, 6.422, 5.115, and 4.374 $Å^2$, respectively (Kim et al., 2014)) as input, and that provides molar fractions as output. We can therefore determine the temporal decay of CH_4 and the related growth of C_2H_6, C_2H_4, and C_2H_2 as shown in figure 4.2 (full circles).

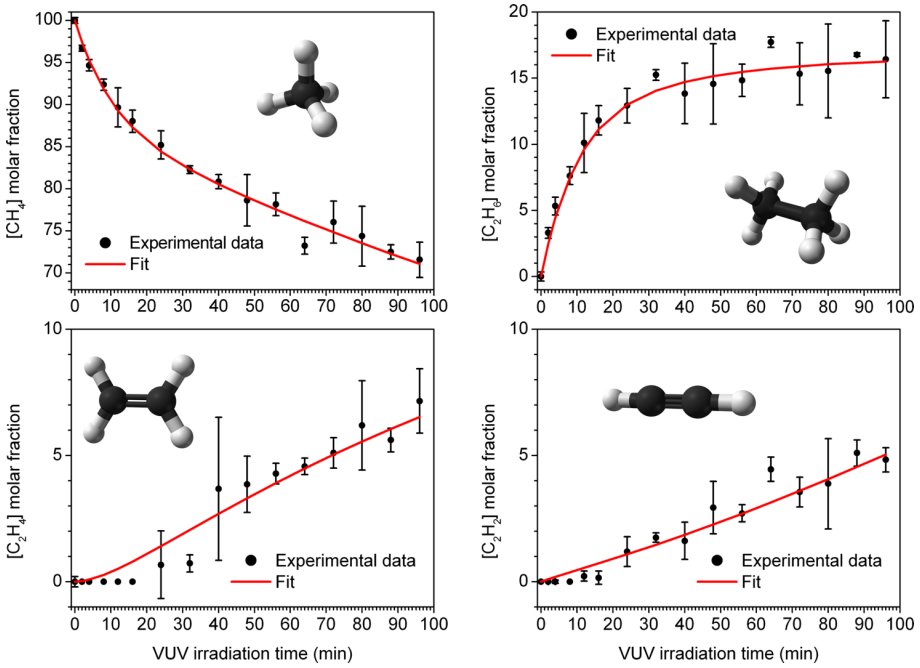

Figure 4.2: Temporal growth and decay of the molar fractions (full circles) of photoproducts and initial material, extracted from the ReTOF mass spectra shown in given in figure 4.1. Fit (in red) of the reduced chemical model (Table 4.1 and Eqs. 6–11) to the molar fractions of methane (*top left*, initial material), ethane (*top right*, photoproduct), ethylene (*bottom left*, photoproduct), and acetylene (*bottom right*, photoproduct). The experimental error bars are representative of the repeatability of the measurements only.

As a check, we extended the set of reference spectra with hydrocarbons containing up to three carbon atoms, thus adding C_3H_8, C_3H_6 and the two C_3H_4 isomers, and we found that these more complex molecules only count for about 4% of the ice mixture at the highest irradiation value (96 min.), meaning that the main photoproducts are – in this study – hydrocarbons with one or two carbon atoms. This will simplify our reaction scheme model

and the total number of parameters to optimise in the next section. Also, a straight exclusion of these larger species does not result in a substantial increase in the uncertainty of the derived parameters. It is important to note at this point that the quantitative approach described above is only used for electron impact mass spectra interpretation by taking into account the fragmentation and that the corresponding outcome is used – in a further step – in a reaction scheme model to understand the actual photochemical processes taking place within the ice.

4.3.1 *Proposed reaction scheme*

We propose a reduced chemical network that is initiated by the methane photodissociation yielding the first generation of photoproducts, i.e., the CH_3, CH_2, and CH radicals, followed by *radical–neutral* and *radical–radical* reactions that form the second generation of photoproducts (e.g., C_2H_6, C_2H_4, and C_2H_2). Then, we allow a limited interplay between each generation of photoproducts, that eventually leads to other hydrocarbons up to two carbon atoms. The reactions considered for the reduced chemical network are given in Table 4.1 and this network comprises a set of 15 distinct reactions with a corresponding R-labeling.

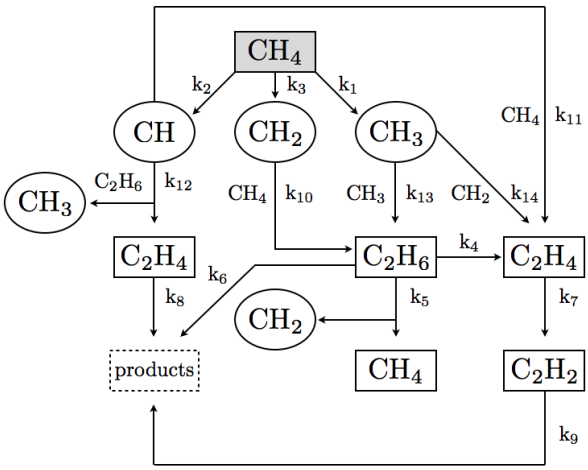

Figure 4.3: Schematic diagram illustrating the reduced reaction network considered in this study. Rectangles indicate stable end-products observable using the LDPI TOF-MS technique, ovals indicate radicals, and the dotted rectangle concerns precursors of hydrocarbons containing more than two carbon atoms.

A schematic diagram is given in figure 4.3 and illustrates the reduced reaction network considered in this study. Note that the model does not take into account tunnelling effects, radical conversions, neither the successive fragmentations of CH_3 leading to CH_2+H and to CH+H radicals; the measured branching ratios are effective values within these settings. Since the *radical–radical* reactions involving the CH_3 and CH_2 radicals (R13-R15) are exothermic and require almost no entrance barrier (Woon, 2002), we assume that they are efficient even at 20 K and occur much faster than the photodissociation pathways that

produce these two radicals (R1 and R3). Thus these two latter routes are assumed to be rate-determining steps. In this way we limit our system to 12 parameters (i.e., reaction rates) instead of 15, initially. The corresponding rate equations (Eqs. 6–11) are listed here in full detail to exclude any ambiguity in the analysis, with the time dependent molar fractions in brackets and the involved reaction numbers in parentheses:

$$\begin{aligned}\frac{d[CH_4]}{dt} = &-2\,k_1\,[CH_4]^2 \quad (R1/R13)\\ &-k_{11}\,[CH_4]\,[CH]-k_2\,[CH_4] \quad (R2/R11)\\ &+k_5\,[C_2H_6] \quad (R5)\\ &-2\,k_3\,[CH_4]^2 \quad (R3/R15)\\ &-k_1\,[CH_4]-k_3\,[CH_4] \quad (R1/R3/R14)\\ &-k_2\,[CH_4] \quad (R2/R12)\\ &-k_3\,[CH_4]-k_{10}\,[CH_4]\,[CH_2] \quad (R3/R10)\end{aligned} \tag{6}$$

Table 4.1: Overview of the reactions involved in this study

Reaction Number	Reaction Type	Rate constant (in s^{-1})
	Photodissociation (first order)	
R1	$CH_4 + h\nu \rightarrow CH_3 + H$	k_1
R2	$CH_4 + h\nu \rightarrow CH + H + H_2$	k_2
R3	$CH_4 + h\nu \rightarrow CH_2$ [a] $+ 2H/H_2$	k_3
R4	$C_2H_6 + h\nu \rightarrow C_2H_4 + 2H/H_2$	k_4
R5	$C_2H_6 + h\nu \rightarrow CH_4 + CH_2$	k_5
R6	$C_2H_6 + h\nu \rightarrow$ products[b]	k_6
R7	$C_2H_4 + h\nu \rightarrow C_2H_2 + 2H/H_2$	k_7
R8	$C_2H_4 + h\nu \rightarrow$ products[c]	k_8
R9	$C_2H_2 + h\nu \rightarrow$ products[d]	k_9
	Neutral–radical (second order)	
R10	$CH_4 + CH_2 \rightarrow CH_3 + CH_3$	k_{10}
R11	$CH_4 + CH \rightarrow C_2H_4 + H$	k_{11}
R12	$C_2H_6 + CH \rightarrow C_2H_4 + CH_3$	k_{12}
	Radical–radical (second order)	Assumptions:
R13	$CH_3 + CH_3 \rightarrow C_2H_6$	$k_{13} \gg k_1$
R14	$CH_3 + CH_2 \rightarrow C_2H_4 + H$	$k_{14} \gg k_1, k_3$
R15	$CH_2 + CH_2 \rightarrow C_2H_2 + 2H/H_2$	$k_{15} \gg k_3$

[a] Singlet and/or triplet state.
[b] C_2H_5+H and/or CH_3+CH_3.
[c] C_2H_3+H.
[d] C_2H+H and/or C_2+H_2.

$$\begin{aligned}\frac{d[C_2H_6]}{dt} = &+ 2\,k_1\,[CH_4]^2 \quad (R1/R13)\\ &- k_5\,[C_2H_6] \quad (R5)\\ &- k_4\,[C_2H_6] \quad (R4)\\ &- k_{12}\,[C_2H_6]\,[CH] \quad (R2/R12)\\ &- k_6\,[C_2H_6] \quad (R6)\\ &+ k_{10}\,[CH_4]\,[CH_2] \quad (R3/R10)\end{aligned} \tag{7}$$

$$\begin{aligned}\frac{d[C_2H_4]}{dt} = &+ k_{11}\,[CH_4]\,[CH] \quad (R2/R11)\\ &+ k_1\,[CH_4] + k_3\,[CH_4] \quad (R1/R3/R14)\\ &+ k_4\,[C_2H_6] \quad (R4)\\ &- k_7\,[C_2H_4] \quad (R7)\\ &- k_8\,[C_2H_4] \quad (R8)\\ &+ k_{12}\,[C_2H_6]\,[CH] \quad (R2/R12)\end{aligned} \tag{8}$$

$$\begin{aligned}\frac{d[C_2H_2]}{dt} = &+ 2\,k_3\,[CH_4]^2 \quad (R3/R15)\\ &+ k_7\,[C_2H_4] \quad (R7)\\ &- k_9\,[C_2H_2] \quad (R9)\end{aligned} \tag{9}$$

$$\begin{aligned}\frac{d[CH_2]}{dt} = &+ k_5\,[C_2H_6] \quad (R5)\\ &+ k_3\,[CH_4] - k_{10}\,[CH_4]\,[CH_2] \quad (R3/R10)\end{aligned} \tag{10}$$

$$\begin{aligned}\frac{d[CH]}{dt} = &- k_{11}\,[CH_4]\,[CH] \quad (R2/R11)\\ &+ k_2\,[CH_4] - k_{12}\,[C_2H_6]\,[CH] \quad (R2/R12)\end{aligned} \tag{11}$$

4.3.2 *Fitting procedure and data treatment*

The system of coupled differential equations is solved numerically by fitting simultaneously the molar fractions of methane $[CH_4]$, ethane $[C_2H_6]$, ethylene $[C_2H_4]$, and acetylene $[C_2H_2]$ at a given irradiation time grid. The methylene radical (CH_2) and methylidyne radical (CH) are intermediate species regarding the *neutral–radical* reactions (R10 – R12). Since we cannot probe their molar fractions as a function of irradiation time, their relative abundances are simply positive variables in the fitting procedure, with the initial conditions $[CH_2]_{t=0} = [CH]_{t=0} = 0\%$. The rate constant optimisation procedure is driven by Matlab 7.9.0 (R2009b) and combines the built-in *ode45* function (ordinary differential equation solver Runge–Kutta 4^{th} and 5^{th} order) with the Nelder-Mead algorithm (Lagarias et al., 1998). The parameter optimisation is proceeded by trying to minimise the squared differences (errors) between the model predictions (y^p) and the experimental values (y):

$$\mathrm{SSE} = \sum_{k=1}^{16}\sum_{l=1}^{4}(y_k - y_k^p)^2, \tag{12}$$

Where k is the number of data points and l corresponds to the number of monitored species. In data fitting, it is usually assumed that the smallest parameter set will provide the most reasonable predictions. The proposed reduced chemical model corresponds to a 12 parameters problem which implies that the function surface has several local solutions. An initial guess of parameters is always required before an optimisation procedure can start. Because the function evaluation (i.e., SSE) strongly depends on the initial set of parameters, the optimisation procedure is repeated many times (e.g., up to 2000 times). This approach is time consuming but creates probability distributions of the estimated parameters, thus providing the statistical analysis tools to (i) estimate the parameters and associated standard errors and (ii) test the linear relationship between each parameter. Before each cycle, an uniformly distributed initial set of 12 rate constants is chosen pseudorandomly from 10^{-1} to 10^{-12} min^{-1}. Each of them can later on vary freely from 0 to 10^{-1} min^{-1} in order to better fit the chemical model to the experimental data. A poor set of starting parameters can lead to a local solution and/or a poor fit, thus giving errors in the rate constants estimation. For this reason, weights (w) are implemented within the different fitting results and they are defined as $1/SSE^2$ so better fits count more than poor ones. The weighted mean (μ_w) and weighted standard deviation (σ_w) are then used to provide an unbiased estimate of both the mean and the standard deviation of the optimised rate constants.

Table 4.2: Effective rate constants and corresponding standard errors of the mean derived from fitting the reduced chemical model (Table 4.1 and Eqs. 6–11) to the experimental data.

Effective Rate Constants (μ_w in s^{-1})		SEM ($\frac{1}{\sqrt{n}} \times \sigma_w$ in s^{-1})
k_5	$= 1.038 \times 10^{-3}$	5×10^{-6}
k_{12}	$= 5.3 \times 10^{-4}$	2×10^{-5}
k_{11}	$= 4.9 \times 10^{-4}$	2×10^{-5}
k_7	$= 1.33 \times 10^{-4}$	3×10^{-6}
k_4	$= 1.115 \times 10^{-4}$	5×10^{-7}
k_9	$= 5.3 \times 10^{-5}$	3×10^{-6}
k_8	$= 2.2 \times 10^{-5}$	2×10^{-6}
k_{10}	$= 7 \times 10^{-6}$	2×10^{-6}
k_6	$= 1.7 \times 10^{-6}$	1×10^{-7}
k_1	$= 1.120 \times 10^{-6}$	3×10^{-9}
k_3	$= 4.26 \times 10^{-8}$	3×10^{-10}
k_2	$= 2.1 \times 10^{-8}$	5×10^{-9}

The weighted mean of each rate constant is given in Table 4.2, together with the standard error of the mean ($SEM = \frac{1}{\sqrt{n}} \times \sigma_w$). The weighted correlation coefficients (rw) are given is Table 4.3 and correspond to real numbers ranging from -1 (anti-correlated) to $+1$ (correlated). The diagonal elements of the correlation matrix are unity by definition. Furthermore, the correlation matrix is a symmetrical matrix so only the lower diagonal is presented. As the rw-values approach zero, the related pair of rate constants is considered either less correlated or uncorrelated. The resulting fits of the reduced chemical model (Eqs. 6–11) to the different molar fraction evolutions are depicted in figure 4.2 and reproduce

Table 4.3: Weighted correlation coefficients (rw) between optimised rates constants ranging from k_1 to k_{12}.

	k_1	k_2	k_3	k_4	k_5	k_6	k_7	k_8	k_9	k_{10}	k_{11}	k_{12}
k_1	1.00	–	–	–	–	–	–	–	–	–	–	–
k_2	-0.06	1.00	–	–	–	–	–	–	–	–	–	–
k_3	0.42	-0.02	1.00	–	–	–	–	–	–	–	–	–
k_4	-0.54	-0.18	-0.92	1.00	–	–	–	–	–	–	–	–
k_5	0.94	-0.03	0.45	-0.52	1.00	–	–	–	–	–	–	–
k_6	-0.34	0.06	-0.23	0.13	-0.33	1.00	–	–	–	–	–	–
k_7	-0.39	0.00	-0.89	0.87	-0.42	0.17	1.00	–	–	–	–	–
k_8	-0.29	0.02	-0.20	0.32	-0.28	0.13	0.19	1.00	–	–	–	–
k_9	-0.29	0.02	-0.54	0.60	-0.30	0.12	0.64	0.10	1.00	–	–	–
k_{10}	-0.41	-0.01	-0.21	0.36	-0.17	0.06	0.20	0.05	0.14	1.00	–	–
k_{11}	0.04	0.01	-0.06	0.05	0.04	-0.02	0.05	0.00	0.03	-0.01	1.00	–
k_{12}	0.04	0.01	-0.04	0.03	0.04	-0.02	0.04	0.01	0.02	0.00	0.16	1.00

the experimental data well, with some deviations for short irradiation times for ethane (C_2H_6) and ethylene (C_2H_4).

4.4 DISCUSSION

We discuss now the results presented above concerning the methane ice photochemistry and kinetic study in the solid phase. The photo-destruction of pure methane leads to the formation of larger photoproducts with numerous unsaturated compounds. After 96 min. of VUV irradiation at 20 K, the composite ice material is mainly formed by CH_4 (70 - 75 %), i.e., CH_4 molecules that have not been consumed or that have been simply reformed, and the rest being photoproducts with up to two carbon atoms. More complex hydrocarbons beyond three C-atoms can be observed but are not taken into account, as discussed earlier. Any quantitative analysis of these hydrocarbons is therefore difficult and provides large uncertainties. However, processes that are diffusion driven like radical-radical reactions involving heavier radicals (e.g., C_2H_5 precursor of C_3- and C_4-hydrocarbons) will be likely enhanced at higher temperatures, thus changing the ice chemistry. The proposed reduced chemical model (Table 4.1 and Eqs. 6–11) includes the three main photodissociation channels of methane and the formation/destruction routes of the three stable photoproducts containing up to two carbon atoms. The proposed model is based on the extensive work performed by the atmospheric chemistry community. We therefore assume that the overall reaction steps collected in the literature from the gas phase studies are also applicable in the solid phase (in contrast to the reaction rate coefficients). We would like to stress that one radical-radical reaction currently listed in the UMIST Database for Astrochemistry (McElroy et al., 2013) was originally included in the model and has been removed. This recombination reaction involves two methyl (CH_3) radicals but in contrast to reaction R13, yields acetylene (C_2H_4) and a molecular hydrogen (H_2):

$$CH_3 + CH_3 \rightarrow C_2H_4 + H_2 \tag{13}$$

By cancelling one by one the different reaction steps in the reduced chemical model, it appears that the presence of this reaction (Eq. 13) never provides a satisfactory conver-

gence criterium in the fitting procedure. Although the molar fractions of acetylene (C_2H_2) were well predicted, the other three molar fractions were largely over- and under-estimated along with the irradiation time, thus leading to a poor fit and finally to the conclusion that this reaction (Eq. 13) likely does not occur in the solid phase.

The photodissociation rates of pure methane ice at 20 K is rather slow with less than 30 % converted in more complex hydrocarbons at the end of 96 min. of photolysis (simulating up to 10^7 years in dense molecular clouds (Prasad & Tarafdar, 1983)). In the reduced chemical model, we assume that R1 and R3 are rate-determining steps. In Table 4.2 we observe that these two photodissociation pathways yielding CH_3 and CH_2 radicals are among the slowest steps in the network ($\leqslant$ 0.1% of the fastest reactions) and therefore determine the rate at which the overall scheme proceeds. This also means that pure methane ices have a remarkable stability under harsh VUV conditions. Previous experimental studies on ices have demonstrated that the photodissociation rates of methane strongly depend on the environment (Cottin et al., 2003). Water-rich porous environments may also affect the diffusion of both neutral and radicals photoproducts (Bossa et al., 2014; Cazaux et al., 2015). Compared to photodissociation rates measured in the gas phase, photodissociation rates in the solid phase are in general substantially lower, most likely because of the fast reverse reactions between the dissociation fragments (Öberg et al., 2010). The reverse reactions R1 and R3 that reform methane and reaction R5 that converts a photoproduct in methane are therefore non negligible in the solid phase. Unsaturated species are less abundant and shielding effects can also play a major role in the chemical evolution and composition of the processed ice. It is for example well known that ethane (C_2H_6) and most higher alkanes are efficiently shielded by methane (CH_4) in the gas phase (Yung & Demore, 1999; Moses et al., 2005), so its destruction is negligible compared to ethylene (C_2H_4) which is less shielded and therefore more destroyed. In this study, we observe that ethane (C_2H_6) is the most abundant photoproduct (Baratta et al., 2002) after ethylene (C_2H_4). This follows the shielding effects observed in the gas phase that seem to apply to the solid state as well.

Following the correlation matrix given in Table 4.3, there are no significant correlations between the optimised parameters k_1, k_2, and k_3, corresponding to the effective rate constants of the different photodissociation channels of methane leading to CH_3, CH, and CH_2 radicals, respectively. We can therefore determine the corresponding branching ratios with good confidence. Table 4.4 lists the calculated branching ratios for the three photodissociation channels of methane in comparison with gas phase data from the literature (Heck et al., 1996; Park et al., 2009; Lodriguito et al., 2009; Gans et al., 2011; Blitz & Seakins, 2012). These results are based on a stable end-products analysis that overcomes the intermediate species detection problem with realistic assumptions. The remaining effective rate constants can be used for any solid state modelling of cold surface irradiation containing methane. Each effective rate constant can be written as $k = \sigma f$, where σ corresponds to the photodissociation cross section for a given reaction (essential for models of interstellar chemistry), and f the given integrated emission flux. It is important to note that strong correlations between a pair of parameters means that both are simultaneously adjusted during the fitting procedure. Therefore, care is needed in their use and interpretation, since these parameters compensate each other (anti-correlated) or vary in about the same proportion (correlated). In this specific case, resulting parameter values and associated errors can be questionable. In our study, only few parameters present significant correlations (k_3/k_4, k_1/k_5, k_3/k_7, and to a lesser extend k_4/k_9 and k_7/k_9), which gives proof of the reliability of the overall network and fitting procedure, but also demonstrates that the parameter estimation remains difficult. The origin of parameter correlations can be diverse and does not necessarily imply the underlying physical or chemical process being studied. For example, a limited set of experimental observations or the fitting process itself

can also induce correlations (Johnson, 2000). Although weighted out, parameters deduced from poor fits still count in the probability distributions of the estimated parameters and may induce correlations. We also observe an intrinsic correlation between k_4 and k_7 which are associated to dehydrogenation processes R4 and R7. These two reactions are linked and yield sequentially ethylene (C_2H_4) and acetylene (C_2H_2) via very similar pathway involving the elimination of a molecular hydrogen (H_2). In addition, both reactions present similar kinetic rates. Therefore, it is not surprising that the corresponding rate constants are correlated: altering either parameter during the fitting procedure induces intrinsically a compensative change in the other.

We conclude now with interpreting the resulting values listed in Table 4.4. Most experimental studies in the gas phase agree that CH radical is the less abundant first generation photoproduct formed during the photolysis of methane (Romanzin et al., 2005; Blitz & Seakins, 2012). We observe the same trend in the solid phase: the CH radical is produced in trace amount (around 2%). The branching ratios are drastically different than those obtained in the gas phase (see also Table 4.4), thus reinforcing the hypothesis that the environment and reverse reactions (unlikely to occur in the gas phase) drive the photoproduct distributions during an irradiation. The primary process yielding the methyl radical (CH_3) is predominant at 20 K, so saturated species and hydrocarbons containing branched alkyl chains are likely expected. Since the reaction requiring the least energy occurs the fastest (Arrhenius law), we assume that the energies required to produce the two other radicals are above the energy required to produce the CH_3 radical (Bennett et al., 2006). This study can help in the identification of hydrocarbons on solar sytem bodies like Saturn's moon Titan that can present pure methane (CH_4) ice in solid aerosols or surface material. However, the pure methane ice studied here cannot be simply extrapolated to environments where ices are likely to be mixed. The branching ratios determined in this work cover the wavelength range of a specific microwave discharge H_2 flow lamp setting. Although pure methane ice presents high absorption close to Lyman-α and very weak absorption from 132 to 165 nm (Wu et al., 2012; Cruz-Diaz et al., 2014), this might not be always the case, especially for photoproducts that absorb at other available wavelengths. Future work should now focus on monochromatic irradiations as well as binary ice mixtures (e.g., N_2:CH_4 or porous H_2O:CH_4).

Table 4.4: Comparison of methane photodissociation pathways in the solid state (this work) and previous gas phase studies. Branching ratios are given in % (adapted from Blitz & Seakins, 2012):

Photolysis pathways:	CH_4 + Ly-α → CH_3 + H	CH_4 + Ly-α → CH_2 + 2H/H_2	CH_4 + Ly-α → CH + H + H_2
This study (solid phase, 20 K)	95±5	4±1	2±1
Gans et al. (2011)[a]	42±5	51±10	7
Lodriguito et al. (2009)[a]	39±3	60±7	15±8
Park et al. (2009)[a]	31±5	69	–
Heck et al. (1996)[a]	66	22	11
Mordaunt et al. (1993)[a]	49	0	51

[a] Gas phase study.

4.5 CONCLUSIONS

The results presented here demonstrate that the LDPI TOF-MS technique can be used to perform a systematic kinetic study on the methane photolysis in the condensed phase at 20 K and provide for the first time effective rate constants and branching ratios for primary processes under VUV light dominated by Lyman-α photons. This work is therefore relevant for modelers in astrochemistry and planetary science. This new experimental approach avoids the problems commonly encountered when using the regular surface science techniques such as limited sensitivity during TPD, infrared band strengths uncertainties, infrared band profile and infrared band overlaps (RAIRS) particularly, in the specific case of complex ices.
The main conclusions of the present work are:

- The photodissociation rates of pure methane ice at 20 K for VUV light dominated by Lyman-α photons are rather slow with less than 30 % converted to stable end-product hydrocarbons containing two carbon atoms (ethane being the most abundant photoproduct after ethylene and acetylene) for a total VUV fluence exposure of $\sim 1 \times 10^{17}$ photons cm^{-2}.

- The rate constants of the different photodissociation channels of methane strongly depend on the environment. The resulting branching ratios derived here for pure methane ice clearly deviate from previous gas phase values.

- Astrochemical models use and often extrapolate gas phase reaction rate coefficients for the solid state. This study shows that this may lead to considerable errors. It also shows that laboratory kinetics studies in the solid phase are now possible and provide for the first time data highly needed in astrochemical models.

BIBLIOGRAPHY

Baratta, G. A., Leto, G., & Palumbo, M. E. 2002, Astron. Astrophys., 384, 343
Bennett, C. J., Jamieson, C. S., Osamura, Y., & Kaiser, R. I. 2006, Astrophys. J., 653, 792
Blitz, M. A. & Seakins, P. W. 2012, Chem. Soc. Rev., 41, 6318
Bossa, J.-B., Borget, F., Duvernay, F., et al. 2012a, Aust. J. Chem., 65
Bossa, J.-B., Isokoski, K., de Valois, M. S., & Linnartz, H. 2012b, Astron. Astrophys., 545, A82
Bossa, J.-B., Isokoski, K., Paardekooper, D. M., et al. 2014, Astron. Astrophys., 561, A136
Brunetto, R., Caniglia, G., Baratta, G. A., & Palumbo, M. E. 2008, Astrophys. J., 686, 1480
Cazaux, S., Bossa, J.-B., Linnartz, H., & Tielens, A. G. G. M. 2015, Astron. Astrophys., 573, A16
Chen, Y.-J., Chuang, K.-J., Muñoz Caro, G. M., et al. 2014, Astrophys. J., 781, 15
Cottin, H., Moore, M. H., & Bénilan, Y. 2003, Astrophys. J., 590, 874
Cruz-Diaz, G. A., Muñoz Caro, G. M., Chen, Y.-J., & Yih, T.-S. 2014, Astron. Astrophys., 562, A120
Dobrijevic, M., Ollivier, J. L., Billebaud, F., Brillet, J., & Parisot, J. P. 2003, Astron. Astrophys., 398, 335
Dohnálek, Z., Kimmel, G. A., Ayotte, P., Smith, R. S., & Kay, B. D. 2003, J. Chem. Phys., 118, 364
El-Adawi, M. K. & Elshehawey, E. F. 1986, J. Appl. Phys., 60, 2250
Focsa, F. & Destombes, J. 2001, Chem. Phys. Lett., 347, 390
Gans, b., Boye-Peronne, S., Broquier, M., et al. 2011, Phys. Chem. Chem. Phys., 13, 8140
Gerakines, P. A., Schutte, W. A., & Ehrenfreund, P. 1996, Astron. Astrophys., 312, 289
Gibb, E. L., Whittet, D. C. B., Boogert, A. C. A., & Tielens, A. G. G. M. 2004, Astrophys. J. Suppl. Ser., 151, 35
Gudipati, M. S. & Yang, R. 2012, Astrophys. J. Lett., 756, L24
Heck, A. J. R., Zare, R. N., & Chandler, D. W. 1996, J. Chem. Phys., 104, 4019
Johnson, M. L. 2000, Numerical Computer Methods, Part C, Vol. 321 (Academic Press), 424–446
Kim, Y.-K., Irikura, K., Rudd, M., et al. 2014, Electron-impact cross sections for Ionization and Excitation
Kim, Y. S. & Kaiser, R. I. 2011, Astrophys. J., 729, 68
Lagarias, J., Reeds, J., Wright, M., & Wright, P. 1998, SIAM. J. Optim., 9, 112
Lee, L. C. & Chiang, C. C. 1983, J. Chem. Phys., 78, 688
Ligterink, N. F. W., Paardekooper, D. M., Chuang, K.-J., et al. 2015, Astron. Astrophys., 584, A56
Lodriguito, M. D., Lendvay, G., & Schatz, G. C. 2009, J. Chem. Phys., 131, 224320
Manion, J. A., Huie, R. E., Levin, R. D., et al. Release 1.6.8, Data version 2013.03, National Institute of Standards and Technology, Gaithersburg, Mary- land, 20899-8320, 2013, http://kinetics.nist.gov/, NIST Chemical Kinetics Database, NIST Standard Reference Database 17, Version 7.0 (Web Version)
McElroy, D., Walsh, C., Markwick, A. J., et al. 2013, Astron. Astrophys., 550, A36
Mispelaer, F., Theulé, P., Aouididi, H., et al. 2013, Astron. Astrophys., 555, A13
Mordaunt, D. H., Lambert, I. R., Morley, G. P., et al. 1993, J. Chem. Phys., 98, 2054
Moses, J. I., Fouchet, T., Bézard, B., et al. 2005, J. Geophys. Res., 110, E08001
Oba, Y., Chigai, T., Osamura, Y., Watanabe, N., & Kouchi, A. 2014, Meteoritics and Planetary Science, 49, 117
Öberg, K. I., Boogert, A. C. A., Pontoppidan, K. M., et al. 2011, Astrophys. J., 740, 109
Öberg, K. I., Bottinelli, S., Jørgensen, J. K., & van Dishoeck, E. F. 2010, Astrophys. J., 716, 825
Öberg, K. I., Fraser, H. J., Boogert, A. C. A., et al. 2007, Astron. Astrophys., 462, 1187
Öberg, K. I., Garrod, R. T., van Dishoeck, E. F., & Linnartz, H. 2009, Astron. Astrophys., 504, 891
Okabe, H. 1978, Photochemistry of small molecules
Paardekooper, D. M., Bossa, J.-B., Isokoski, K., & Linnartz, H. 2014, Rev. Sci. Instrum., 85, 104501
Park, J., Lee, P., Sim, K., Wook Han, J., & Yi, W. 2009, Bull. Korean Chem. Soc., 29, 177
Prasad, S. S. & Tarafdar, S. P. 1983, Astrophys. J., 267, 603
Romanzin, C., Gazeau, M.-C., Bénilan, Y., et al. 2005, Adv. Space Res, 36, 258
Shkrob, I. A., Marin, T. M., Adhikary, A., & Sevilla, M. D. 2011, J. Phys. Chem. C., 115, 3393
Smith, G. P. & Nash, D. 2006, Icarus, 182, 181
Stein, S. 2014, "Mass Spectra" in NIST Chemistry WebBook, NIST Standard Reference Database Number 69, Eds. P.J. Linstrom and W.G. Mallard, National Institute of Standards and Technology, Gaithersburg MD, 20899, http://webbook.nist.gov, (retrieved May 7, 2014).
Theulé, P., Duvernay, F., Danger, G., et al. 2013, Adv. Space Res, 52, 1567
Toriyama, K. & Iwasaki, M. 1979, J. Am. Chem. Soc, 101, 2516
van Dishoeck, E. F. 2014, Farad. Discuss., 168, 9
Wakelam, V., Herbst, E., Loison, J.-C., et al. 2012, Astrophys. J. Suppl. Ser., 199, 21
Wakelam, V., Smith, I. W. M., Herbst, E., et al. 2010, Space Sci. Rev., 156, 13
Wilson, E. H. & Atreya, S. K. 2000, J. Geophys. Res. E, 105, 20263
Woon, D. E. 2002, Astrophys. J. Lett., 571, L177
Wu, Y.-J., Wu, C. Y. R., Chou, S.-L., et al. 2012, Astrophys. J., 746, 175
Yung, Y. L. & Demore, W. B. 1999, Photochemistry in planetary atmospheres, ed. Y. L. Yung & W. B. Demore (Oxford University Press, New York)
Zhitnikov, R. A. & Dmitriev, Y. A. 2002, Astron. Astrophys., 386, 1129

5

LASER DESORPTION TIME-OF-FLIGHT MASS SPECTROMETRY OF VUV PHOTO-PROCESSED METHANOL ICE

Context. Methanol in the interstellar medium mainly forms upon sequential hydrogenation of solid CO. With typical abundances of up to 15% (with respect to water) it is an important constituent of interstellar ices where it is considered as a precursor in the formation of large and complex organic molecules (COMs), e.g. upon vacuum UV (VUV) photo-processing or exposure to cosmic rays.
Aims. This study aims at detecting novel complex organic molecules formed during the VUV photo-processing of methanol ice in the laboratory using a technique more sensitive than regular surface diagnostic tools. In addition, the formation kinetics of the main photo-products of methanol are unravelled for an astronomically relevant temperature (20 K) and radiation dose.
Methods. The VUV photo-processing of CH_3OH ice is studied by applying laser desorption post-ionisation time-of-flight mass spectrometry (LDPI TOF-MS), and analysed by combining molecule-specific fragmentation and desorption features.
Results. The mass spectra correspond to fragment ions originating from a number of previously recorded molecules and from new COMs, such as the series $(CO)_xH_y^+$, with $x = 3$ and $y < 3x - 1$, to which prebiotic glycerin belongs. The formation of these large COMs has not been reported in earlier photolysis studies and suggests that such complex species may form in the solid state under interstellar conditions.

D. M. Paardekooper, J.-B. Bossa and H. Linnartz, *Laser desorption time-of-flight mass spectrometry of VUV photo-processed methanol ice*, Astron. Astrophys., (in press, DOI:10.1051/0004 – 6361/201527937)

5.1 INTRODUCTION

In the interstellar medium, methanol (CH_3OH) is considered to be an important solid state precursor species in the formation of complex organic molecules (COMs) (van Dishoeck, 2014). Methanol is mainly formed through sequential hydrogenation of CO ice on top of cold dust grains, a process well studied in the laboratory (Watanabe & Kouchi, 2002; Fuchs et al., 2009; Chuang et al., 2016). This is fully consistent with astronomical observations, indicating that solid CH_3OH is abundant and predominately mixed with CO inside the ice mantle (Cuppen et al., 2011; Boogert et al., 2015; Penteado et al., 2015).

Upon (non)energetic processing, such interstellar ices become chemically active. Typically, atom-addition reactions or recombination reactions of fragments formed upon vacuum UV (VUV) irradiation, cosmic ion bombardment, or electron-impact result in the formation of new species. These processes have been simulated in different laboratories (Gerakines et al., 1996; Baratta et al., 2002; Bennett & Kaiser, 2007; Öberg et al., 2009; Hama & Watanabe, 2013; Islam et al., 2014; Boamah et al., 2014; Maity et al., 2014, 2015; Linnartz et al., 2015; Chuang et al., 2016; Mrad et al., 2016). These studies apply infrared (IR) spectroscopy (transmission or reflection) and temperature programmed desorption (TPD) combined with either quadrupole mass spectrometry (QMS), single photon ionisation time-of-flight mass spectrometry (SPI TOF-MS), or gas chromatography coupled to mass spectrometry (GC-MS). Several recent studies have shown how new products form upon processing of CH_3OH rich ices. In Baratta et al. (2002); Bennett & Kaiser (2007); Islam et al. (2014); Boamah et al. (2014); Maity et al. (2014, 2015) the role of electron or ion bombardment has been studied and in Gerakines et al. (1996); Hudson & Moore (2000); Baratta et al. (2002); Moore & Hudson (2005); Öberg et al. (2009); Islam et al. (2014); Mrad et al. (2016) VUV photolysis has been characterised. An overview of species detected in recent laboratory studies focusing on methanol ice processing is shown in the first four columns of Table 5.1. It is clear that all these solid state processes offer pathways towards molecular complexity in space. The techniques used for these identifications are powerful, sophisticated, and reliable. They have provided detailed insights into the processes at play, but every detection scheme comes with limitations, especially when low temperatures are involved. In situ IR spectroscopy, for example, holds the risk of overlapping bands or non-detections because of IR inactive modes. Ice destruction is inherent to TPD, which in parallel – like GC-MS – may induce thermally induced reactions. Recently, complementary detection schemes have become available that attempt to obtain new information from different perspectives on processed interstellar ice analogues (Henderson & Gudipati, 2015; Paardekooper et al., 2014; Bossa et al., 2015).

In the present study, we apply laser desorption post-ionisation time-of-flight mass spectrometry (LDPI TOF-MS) to gain additional insights into the photo-products of VUV processed CH_3OH ice. This technique has distinct advantages over the traditional techniques: i) Compared to infrared spectroscopy, this technique has an improved sensitivity (several orders of magnitude) and for a number of applications, the method is also more molecule selective. In addition, since ionisation is realised through energetic electrons, a quantitative analysis becomes possible since electron-impact cross sections of different species are known from literature; ii) Compared to regular TPD methods the total composition of the ice at any given temperature can be tracked; and iii) Any thermally induced reactions during TPD can be largely excluded. However, the interpretation of the LDPI TOF-MS data, is not straightforward and this is discussed below.

This paper is organised as follows. Section 5.2 presents a brief description of the experimental set-up and provides a detailed description of the data analysis performed. Section 5.3 presents the qualitative and quantitative interpretation of the experimental results. In section 5.4, the results are compared to conclusions from other studies available in the

Table 5.1: Overview of recent studies focusing on energetically processing methanol ice using a variety of detection techniques.

Molecule	Öberg et al.[1] (2009) VUV TPD/QMS and IR	Boamah et al.[2] (2014) 20 eV electrons TPD/QMS	Maity et al.[3] (2015) 2 keV electrons TPD/SPI TOF-MS and IR	Henderson & Gudipati[4] (2015) 2 keV electrons, VUV[A] 2S-LAIMS[B]	This work VUV LDPI TOF-MS
Carbon monoxide (CO)	Y		Y	Y?	Y
Methane (CH_4)	Y		Y	Y	Y
Ethane (C_2H_6)				Y?	?
Carbon dioxide (CO_2)	Y		Y	Y?	Y
Formaldehyde (H_2CO)	Y	Y	Y	Y	Y
Dimethyl ether (CH_3OCH_3)	Y	Y	Y		Y
Acetaldehyde (CH_3CHO)	Y	Y	Y	Y?	Y
Methyl formate ($HCOOCH_3$)	Y?	Y	Y	Y?	Y
Ethanol (CH_3CH_2OH)	Y	Y	Y		Y
Water (H_2O)				Y	Y
Ketene (H_2CCO)			Y		
Formic acid (HCOOH)	Y?				Y?
Acetic acid (CH_3COOH)	Y?	Y?			Y
Glycolaldehyde ($HOCH_2CHO$)	Y?	Y?	Y		Y
Methoxymethanol (CH_3OCH_2OH)		Y	Y		Y?
Ethylene glycol $(CH_2OH)_2$	Y	Y	Y		Y
Glycolic acid ($HOCH_2COOH$)		Y?			
Glycerin ($HOCH_2CHOHCH_2OH$)		Y?	Y		Y

[1] Öberg et al. (2009)
[2] Boamah et al. (2014)
[3] Maity et al. (2014)
[4] Henderson & Gudipati (2015) [A] In this study, 2 keV electrons are also used as energetic processing yielding a high degree of complexity, such as ethenone, glycolaldehyde, methyl acetate, ethyl acetate, and CH_3CO, as well as other species that are only tentatively identified. [B] 2S-LAIMS: two-step laser ablation and ionisation mass spectrometry.

literature. In section 5.5, the astrophysical implications are discussed and the main findings are summarised.

5.2 EXPERIMENTS AND ANALYSIS

5.2.1 *Experiments*

The experiments were carried out in our ultrahigh vacuum (UHV) set-up, MATRI^{2}CES (Mass Analytical Tool to study Reactions in Interstellar ICES), previously described in detail in chapter 2 (Paardekooper et al., 2014). MATRI^{2}CES consists of two UHV chambers, the main chamber for ice preparation and ice processing and a time-of-flight chamber. The base pressure of these chambers is in the 10^{-10} mbar range. In the main chamber a gold-coated copper substrate is in thermal contact with a closed-cycle helium cryostat, enabling substrate-temperatures down to 20 K. An accurate temperature control is achieved using a thermocouple and heating element, combined with a LakeShore-temperature regulator (model 331). Ices are grown on the substrate by leaking in gas-phase species through an all-metal needle valve attached to a capillary. Residual gasses trapped in liquid samples such as methanol, CH_3OH (Sigma Aldrich, 99.8%), and 13-methanol $^{13}CH_3OH$ (Sigma Aldrich, 99%) are removed by several freeze-pump-thaw cycles. The deposition rate of methanol was determined in advance by HeNe laser interference measurements (Baratta & Palumbo, 1998), using a refractive index of n = 1.33 (Weast, 1972). The substrate is stationary during deposition of the ice. Typical deposition times are 5 minutes and the ice growth is stopped when an ice thickness of ~ 13.5 nm is reached; this corresponds to ~ 40 monolayers (1 ML = 10^{15} molecules cm^{-2}).

MATRI^{2}CES deploys LDPI TOF-MS as a detection scheme to study new molecules formed in the VUV photo-processed ice. Desorption of the ice sample is induced using the unfocused, skimmed beam (~1 mm) of the third harmonic of a Nd:YAG laser (355 nm with a pulse length of $4-5$ ns). An attenuator is used to reduce the energy of the laser pulses. Typical laser pulse energies are of the order of 30 mJ cm^{-2}. The desorbed species are subsequently ionised by an electron gun, with a mean energy of either 35 or 70 eV. Since this energy exceeds the ionisation potential of molecules, this predominately results in dissociative ionisation. The generated ions are extracted by ion optics, situated in close proximity to the substrate. Subsequently, ions enter a field-free flight tube, which allows the ions to drift and to separate based on their mass-to-charge ratios (m/z), after which they are detected by a micro-channel plate (MCP). In the current configuration the mass resolution (M/ΔM) is about 400 (Paardekooper et al., 2014). Multiple desorption events for each ice sample are possible, since the cryostat is situated on top of two UHV translators, i.e. different surface areas are probed for subsequent desorption events. Typically 220 ablation events are measured along a column of 20 mm and this is repeated for nine columns. This guarantees that only the VUV photoprocessed ice region is studied (in principle it is possible to monitor a larger surface area). The columns are separated by 1.25 mm, i.e. there is no overlap of laser ablated ice surfaces between different columns. However, along one column subsequent ablation spots do overlap. This could cause problems as the beam is unfocused and the same ice spot is hit by overlapping laser pulses. However, no substantial changes were found for lower laser repetition rates and identical translation speed, i.e. for conditions where the spatial overlap decreases. Therefore, the data acquisition is operated for 220 spots, and this high number allows the S/N to increase. Throughout the article, we will use 'mass spectra' when referring to LDPI TOF-MS data.

Vacuum UV photo-processing is performed using a flowing H_2 microwave discharge lamp. Typical settings are 0.85 mbar and 80 W of applied microwave power. The lamp is attached to a MgF_2 UHV window directly facing the substrate; the distance between the

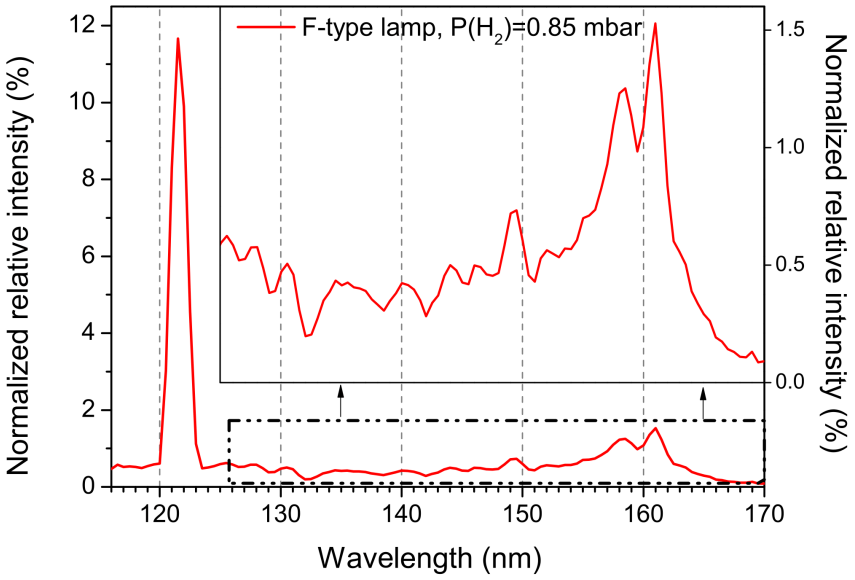

Figure 5.1: Spectral energy distribution of the VUV lamp (116-170 nm) described in the text (Ligterink et al., 2015, chapter 3).

window and the substrate is 14 cm. In a number of recent studies the spectral emission distribution of this lamp has been characterised in detail (see chapter 3, Chen et al., 2014; Es-sebbar et al., 2015; Ligterink et al., 2015). The spectral energy distribution is shown in figure 5.1. The flux at sample location is $(3 \pm 1) \cdot 10^{13}$ photons $cm^{-2}s^{-1}$; the spectral energy distribution peaks at Lyman-α ($\sim$ 121 nm) and around 160 nm. The VUV irradiation can be stopped at different times, i.e. for different total fluences, after which a mass spectrum can be recorded. This method can also characterise the photolysis kinetics of the precursor methanol and reaction products. Typical irradiation times amount to a few hours, i.e. much shorter than in other photolysis experiments (Bernstein et al., 2002; Muñoz Caro et al., 2002; Mrad et al., 2016).

5.2.2 *Analysis*

The acquired mass spectra are first discussed in a qualitative way, as a quantitative interpretation is complicated by the fragmentation upon electron-impact ionisation. We follow a three-step approach. First, MATRI^{2}CES is used to record the reference fragmentation patterns of the majority of the species expected to form upon VUV photolysis of methanol ice. These measurements are performed for two electron-impact energies, 35 and 70 eV. This is described in section 5.2.2.1. The second step, described in section 5.2.2.2, is to obtain mass spectra of irradiated methanol ice at elevated temperatures. Since different molecules sublime at different temperatures, we can link the relative decrease in intensity for the mass peaks with temperature to specific molecules. This step determines which species should be considered for the inclusion in the quantitative fit of the mass spectra, recorded for 20 K. By combining all the information in the final step, the low-temperature

photolysis data of methanol can be interpreted to obtain the abundances and kinetics of individual species; the fitting procedure is described in section 5.2.2.3.

5.2.2.1 *Reference experiments*

The NIST database[1] provides a guideline for the fragmentation of species at 70 eV electron-impact energy. For a more precise analysis it is necessary to derive set-up specific dissociative ionisation patterns (Schwarz-Selinger et al., 2001). Therefore, we measured the fragmentation pattern of most of the species that we expect to form during the VUV irradiation of CH_3OH ice in MATRI^{2}CES. The candidate species (Table 5.2) were selected based on studies of processed CH_3OH ice available in the literature (Öberg et al., 2009; Boamah et al., 2014; Maity et al., 2015). Using two different ionisation energies (35 and 70 eV) provides additional information. Owing to experimental limitations, the reference fragmentation patterns of species with negligible vapour pressure could not be recorded. The maximum number of fragment ions is produced at 70 eV since the de Broglie wavelength of the electrons is similar to the intramolecular bond length. A lower electron energy (35 eV) was also used since the fragmentation patterns differ from 70 eV while maintaining a relative high ion yield. Attempts to record mass spectra for electron energies near the ionisation potential (10-15 eV) were not successful because for these low energies both the electron densities and corresponding cross sections rapidly drop.

Table 5.2: Properties and sample purities of potential photoproducts of VUV-irradiated methanol ice.

Molecule	Chemical formula	Sample purity	T_{des}
Carbon monoxide	CO	99.997% (Praxair)	28 K
Methane	CH_4	99.999% (Praxair)	30 K
Ethane	C_2H_6	99% (Fluka)	60 K
Carbon dioxide	CO_2	99.996% (Praxair)	85 K
Formaldehyde	H_2CO	95% (Sigma Aldrich)[2]	95 K
Dimethyl ether	CH_3OCH_3	$\geqslant$ 99.9% (Fluka)	95 K
Acetaldehyde	CH_3CHO	$\geqslant$ 99.5% (Sigma Aldrich)	105 K
Methyl formate	$HCOOCH_3$	99% (Sigma Aldrich)	120 K
Methanol	CH_3OH	99.8% (Sigma Aldrich)	130 K
Ethanol	CH_3CH_2OH	$\geqslant$ 99.8% (Sigma Aldrich)	145 K
Water	H_2O	milliQ-grade	155 K
Formic acid	HCOOH	$\geqslant$ 95% (Sigma Aldrich)	130 K
Acetic acid	CH_3COOH	$\geqslant$ 99.8% (Sigma Aldrich)	155 K
Glycolaldehyde	$HOCH_2CHO$	Dimer (Sigma Aldrich)[3]	166 K
Ethylene glycol	$(CH_2OH)_2$	99.8% (Sigma Aldrich)	198 K
Glycolic acid	$HOCH_2COOH$	99% (Sigma Aldrich)[4]	235 K
Glycerin	$HOCH_2CHOHCH_2OH$	$\geqslant$ 99.5% (Sigma Aldrich)[4]	235 K

[2] Gas phase monomer obtained by heating paraformaldehyde to 50°C under vacuum.
[3] Gas phase monomer obtained by heating glycolaldehyde dimer to 80°C under vacuum (Hudson et al., 2005).
[4] Glycolic acid and glycerin have a low vapour pressure at room temperature; owing to experimental constraints it was not possible to obtain their reference mass spectra.

1 http://webbook.nist.gov/chemistry/

5.2.2.2 *Experiments at elevated temperature*

Additional information is obtained by taking into account that different ice constituents desorb at different temperatures. For this, we recorded a mass spectrum (70 eV) after irradiating methanol ice (20 K) for 64 minutes. Subsequently, the VUV irradiated ice was slowly (2.5 K min^{-1}) heated to 50 K, and was left to settle for 15 minutes. At this elevated temperature, CO and CH_4 thermally desorb, but molecules trapped inside the methanol matrix do not. Changes in the resulting mass spectrum summarised in the mass difference graphs reflect the loss of evaporated ice constituents. The decline of the dominant peaks of the reference fragmentation patterns confirms the presence of this molecule in the methanol irradiated ice. In this way, more species can be positively identified by using selected sets of temperatures that include the thermal desorption values of a large number of species (see Table 5.2). Here temperature ranges of 20-50, 50-100, 100-125, 125-150, 150-175, and 175-210 K are probed separately.

5.2.2.3 *Fitting*

Mass spectra are measured for different VUV fluences. A baseline correction is performed by fitting a baseline through an array of points where no mass signal is recorded. Subsequent integration of the individual peaks yields the total intensity of every single mass. Each of these mass spectra can be regarded as a linear combination of fragment ions from n individual compounds present in the ablated material,

$$MS_{t,E} = \sum_{i=1}^{n} a_i \times \sigma_{i,E} \times MS_{i,E} \tag{14}$$

where $MS_{t,E}$ is the mass spectrum acquired after a specific irradiation time t, i.e. specific VUV fluence, and electron energy E; a_i corresponds to the fitted mole fraction of a constituent i; and $\sigma_{i,E}$ and $MS_{i,E}$ are the corresponding electron-impact cross section and the reference mass spectrum, respectively. The fitting procedure is performed with Matlab 7.9.0 (R2009b) using the Nelder-Mead optimisation algorithm (Lagarias et al., 1998).

This method has recently been applied to interpret the VUV photo-processing of methane (CH_4, Paardekooper et al., 2014; Bossa et al., 2015). The method is here extended to fit equation 14 to the mass spectra recorded for two different electron energies, E. As the two different electron energies result in different fragmentation patterns, this adds extra constraints to the fit. Candidate species for the fitting library are selected based on their presence in experiments performed at elevated temperatures (see section 5.2.2.2).

This procedure comes with the shortcoming that possibly not all formed constituents are actually included in the fit, but we explicitly assume that these missing species are not formed in high abundances and consequently we expect that the overall accuracy of the fit is not strongly affected.

5.3 EXPERIMENTAL RESULTS

This section is divided into two parts. Section 5.3.1 describes a qualitative interpretation of the obtained mass spectra. Section 5.3.2 continues with a quantitative interpretation based on the approach described in section 5.2.2.

5.3.1 *Qualitative analysis*

5.3.1.1 *Unprocessed CH_3OH ice*

The mass spectra of unprocessed CH_3OH ice upon 35 and 70 eV electron impact ionisation are shown in figure 5.2. Clear differences are visible in the number of ions detected and the relative intensities for the different fragmentation channels. Comparing the 70 eV mass spectrum to the NIST database, the observed fragmentation pattern is in agreement within 15%. Such a small mismatch is expected for different experimental set-ups, as the exact values depend on the geometry of the ion source, the temperature of the filament, and the distribution in electron energies (Schwarz-Selinger et al., 2001). Moreover, protonated methanol-clusters are observed, for example at m/z = 65, 97, and 129 in figure 5.2. These originate from the clustering reaction:

$$(CH_3OH)^+_{n+1} \rightarrow (CH_3OH)_nH^+ + CH_3O \tag{15}$$

Focsa & Destombes (2001) showed that cluster formation in laser-induced desorption experiments of concentrated and polar molecules can take place; for pure methanol ice this has also been reported by Henderson & Gudipati (2015), and it is straightforward to identify the cluster mass since the main component of the ice is known. This changes when the ice is VUV processed and the resulting ice constituents are not fully known. The figure shows that it is important to take the presence of cluster ions into account when interpreting the mass signals.

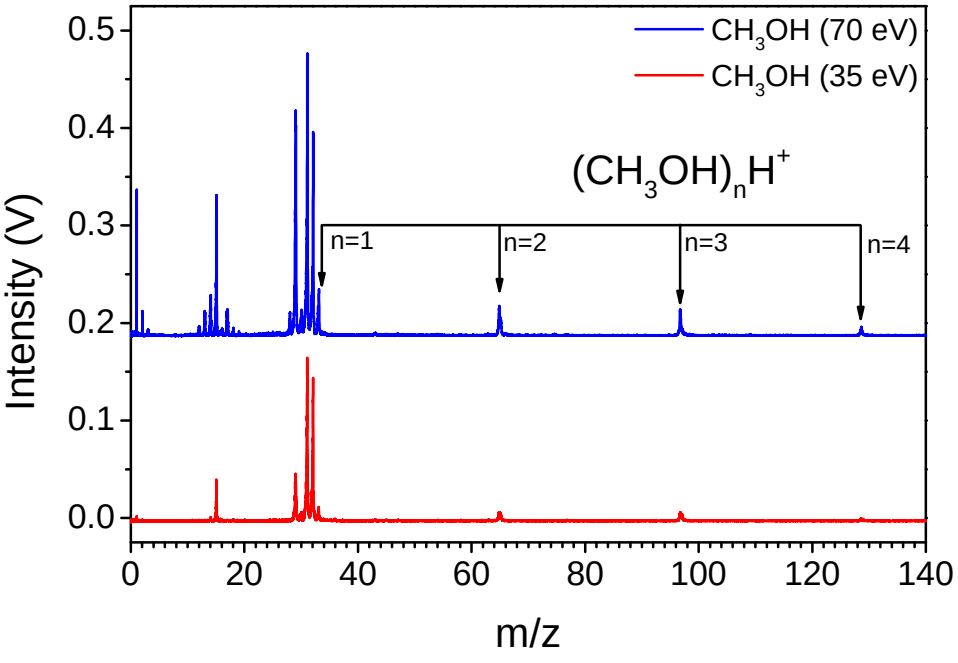

Figure 5.2: Reference mass spectra of ~ 13.5 nm-thick CH_3OH ice deposited at 20 K, using 35 eV (red) and 70 eV (blue) electrons as an ionisation source.

5.3.1.2 *VUV processed CH_3OH ice*

In figure 5.3, mass spectra are shown for CH_3OH ice for different VUV fluences. As soon as the irradiation starts, the number of peaks at higher masses increases, which indicates that COMs are formed in the ice. At m/z = 63 and 95, mass peaks two m/z units below the mass value of protonated methanol dimer and trimer, a clear increase in intensity is observed. These have been assigned earlier to methanol oxidation products, clustering with methanol (Henderson & Gudipati, 2015). To discriminate between cluster peaks and photo-products, we performed two experiments with different laser pulse energies, as this results in different densities in the desorption plume (Paardekooper et al., 2014), and also influences the intensity of the cluster peaks. All m/z containing ion counts in the spectra are integrated, and the fraction of both high and low laser pulse energy mass signals is presented in figure 5.4.

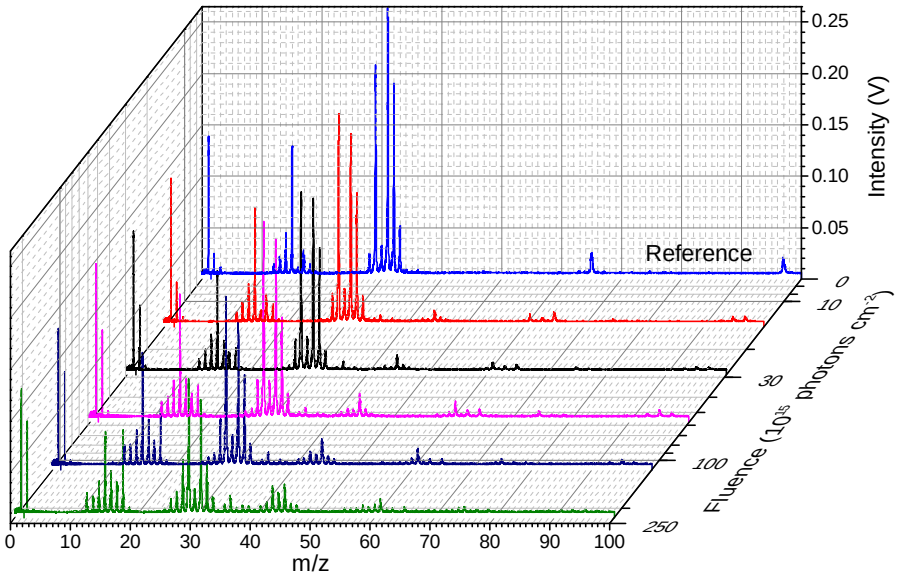

Figure 5.3: Mass spectra of ~ 13.5 nm-thick methanol ice, deposited at 20 K, using 70 eV electrons as an ionisation source, at different VUV fluence. The VUV fluence is plotted on a log scale, for clarity the reference spectrum is presented at the origin.

At low m/z values (<47), with the exception of m/z = 33 $(CH_3OH)H^+$, no cluster signals are present. The signals in that region originate from photoproducts present in the ice. Therefore, by linearly extrapolating the reliable low-mass products (<47), it is possible to discriminate between mass peaks originating from clusters and from products. Based on this approach, we attribute the origin of the following masses predominantly to clusters: m/z = 33, 63, 65, 75, 79, 93, 95, and 97. We can directly assign 33, 65, and 97 to the protonated methanol clusters, $(CH_3OH)_nH^+$. From previous work (Henderson & Gudipati, 2015), m/z values at 59, 61, 73, 77, 89 and 91 are also expected to contain at least small cluster contributions. For our experimental conditions, however, we do not find strong experimental evidence of clustering at these m/z values. The remaining peaks are direct evidence of the formation of new species, including larger COMs, which is the topic of this study.

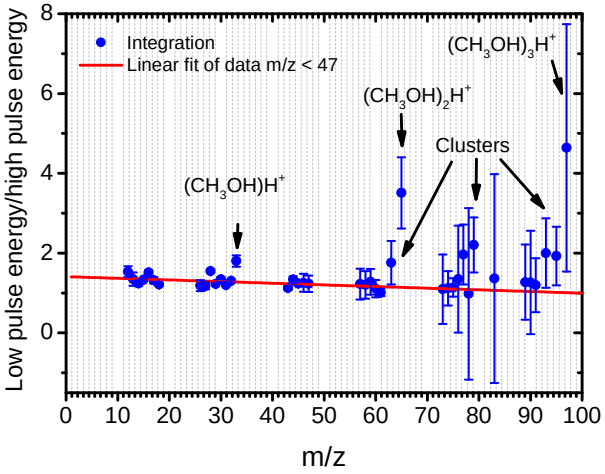

Figure 5.4: Intensity ratio of low to high laser pulse energy. A $2\,\sigma$-error bar is shown.

In figure 5.5, a mass spectrum is shown where the methanol ice has been processed with VUV photons for 128 minutes leading to a fluence of $(2.3 \pm 0.8) \cdot 10^{17}$ photons cm^{-2}. Mass signals from cluster ions are indicated and it is clear that new mass peaks are detected in the range of m/z = 85..91. These peaks likely originate from $(CO)_xH_y^+$, with $x = 3$ and $y < 3x - 1$. This result proves that the parent molecules leading to these fragment ions contain at least a total of six carbon or oxygen atoms. This finding is important as to date no low temperature (20 K) in situ studies have reported COMs in this size range upon relatively short VUV photolysis of pure methanol ice. Previous results, including the findings in the recent study by Mrad et al. (2016), were realised after irradiation of an ice mixture for days, using gas chromatography to identify the chemical components of the resulting residue (Muñoz Caro et al., 2002; Bernstein et al., 2002; Briggs et al., 1992). The present study shows in situ and in real time that large complex species are indeed formed. Other studies on the processing of methanol ice with electrons (Boamah et al., 2014; Maity et al., 2015; Kaiser et al., 2015), using QMS or SPI TOF-MS combined with TPD, find larger species as well, but as in the case of the GC-MS studies special care is needed to exclude that new species are thermally formed during the warm-up phase.

5.3.1.3 *VUV processed CH_3OH and $^{13}CH_3OH$ ice*

Figure 5.6 presents the mass spectra of VUV photo-processed CH_3OH and $^{13}CH_3OH$ ices. The $^{12}C \rightarrow {}^{13}C$ isotopic shifts are a guide in determining the number of carbon atoms reflected by particular peaks. This supports, for example, the assignment of the cluster m/z = 65 to $(CH_3OH)_2H^+$ since this mass shifts to m/z = 67. The mass peak at m/z = 75 shifts to m/z = 78, indicating that the corresponding fragment ion consists of three carbon and two oxygen atoms.

The peak intensities shown in figure 5.6 are integrated, and are correlated with respect to the isotopic shift, $C_nO_mH_y^+$ and $^{13}C_nO_mH_y^+$, with $n = 1..2$ and $m = 0..n$. For example, one data point is the integrated area of $^{12}CH^+$ with respect to $^{13}CH^+$; another is $^{12}C_2H_2O^+$ with respect to $^{13}C_2H_2O^+$. The corresponding correlation diagram is shown in the inset of figure 5.6, and confirms a good correlation between carbon content and the chosen assignment.

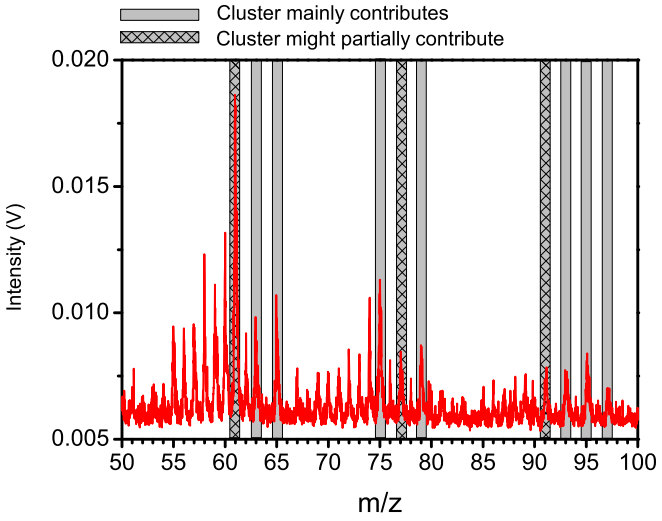

Figure 5.5: Mass spectrum of ~ 13.5 nm-thick methanol ice deposited at 20 K, photo-processed for 128 min corresponding with a fluence of $(2.3 \pm 0.8) \cdot 10^{17}$ photons cm^{-2} using 70 eV electrons as an ionisation source.

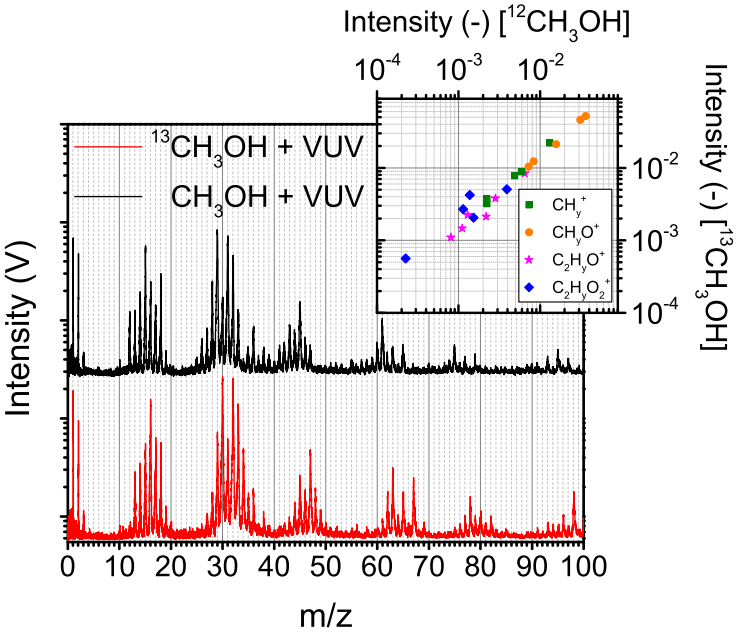

Figure 5.6: Mass spectrum of ~ 13.5 nm-thick methanol ice (CH_3OH and $^{13}CH_3OH$) deposited at 20 K, using 70 eV electrons as an ionisation source, irradiated for 64 min and corresponding fluence: $(1.2 \pm 0.4) \cdot 10^{17}$ photons cm^{-2}. The inset depicts the correlation of the peak intensities between the two experiments, i.e. $^{12}CH_y$ vs. $^{13}CH_y$.

5.3.2 *Quantitative analysis*

A quantitative interpretation of the data presented in the previous paragraphs is not straightforward. Different photo-products fragment into similar masses upon electron impact ionisation, which complicates the analysis. However, as explained in section 5.2.2.3, it is possible to incorporate another molecule-specific parameter as a diagnostic tool, namely the desorption temperature. In the paragraphs below, the photo-products are assigned using this extra information, and the mass spectra are interpreted in terms of the set-up specific reference fragmentation patterns. This allows a fitting library to be created for both the 35 and 70 eV electron-impact ionisation experiments. The resulting data are used as input to interpret the mass spectra of the photo-processed methanol ice at 20 K and to determine which new species are formed.

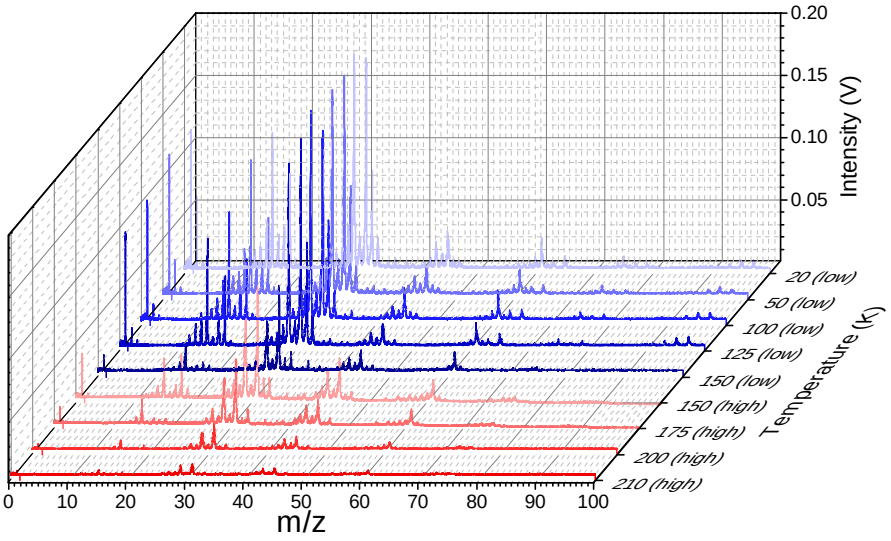

Figure 5.7: Overview of the mass spectra of VUV processed methanol ice acquired at different temperatures, using 70 eV electrons as an ionisation source. The fluence level is noted in brackets. Low fluence corresponds to $(1.2 \pm 0.4) \cdot 10^{17}$ photons cm^{-2} and high fluence to $(5 \pm 2) \cdot 10^{17}$ photons cm^{-2} (estimated). The high-fluence experiment follows a different experimental procedure: simultaneous deposition ($\sim$ 240 ML) and photolysis (4 hours).

5.3.2.1 *Assignment of photolysis products*

In order to confirm the presence of different photoproducts, we have conducted experiments in which we first VUV irradiate CH_3OH ice at 20 K for 64 minutes, corresponding to a fluence of $(1.2 \pm 0.4) \cdot 10^{17}$ photons cm^{-2}. Subsequently, before and after increasing the substrate temperature, mass spectra are recorded using 70 eV electrons as an ionisation source. The strategy is to visualise the thermally induced decrease in the dominant peaks in the reference fragmentation pattern and to link this to a specific reaction product, based on the temperature range where a decrease is observed. In addition to the decrease caused by desorption, other changes in the ice can also affect the peak intensities, such as

local rearrangement and phase changes of the ice structure. The desorption temperature of different species is listed in Table 5.2. The desorption profiles are typically wide and can therefore cause overlap between temperature gaps.

To strengthen the assignment of species with desorption temperatures higher than methanol (~ 130 K) we conducted an experiment following a different procedure. After reaching a substrate temperature of 20 K, we deposited methanol with a slow deposition rate (~ 1 ML/min) for a duration of 4 hours, while simultaneously exposing the sample to VUV photons. In our experimental conditions this approach yields a higher energy deposit per molecule and a thicker layer of processed ice (~ 240 ML). In turn, a larger abundance of COMs is obtained. Subsequently, the temperature was ramped up to 150, 175, 200, and 210 K. Mass spectra were recorded for all temperatures. Figure 5.7 provides an overview of both low- and high-fluence experiments. Up to 150 K, the spectra show the previously mentioned protonated methanol clusters. Above this temperature, these signals nearly vanish.

In order to characterise new photoproducts, we compare the difference in absolute intensity of individual mass peaks to reference mass spectra between 20 and 50 K (A), 50 and 100 K (B), 100 and 125 K (C), 125 and 150 K (D), 150 and 175 K (E), and 175 and 210 K (F). As an illustrating example, first one figure will be discussed (Fig. 5.8), covering 150 to 175 K (i.e. range E).

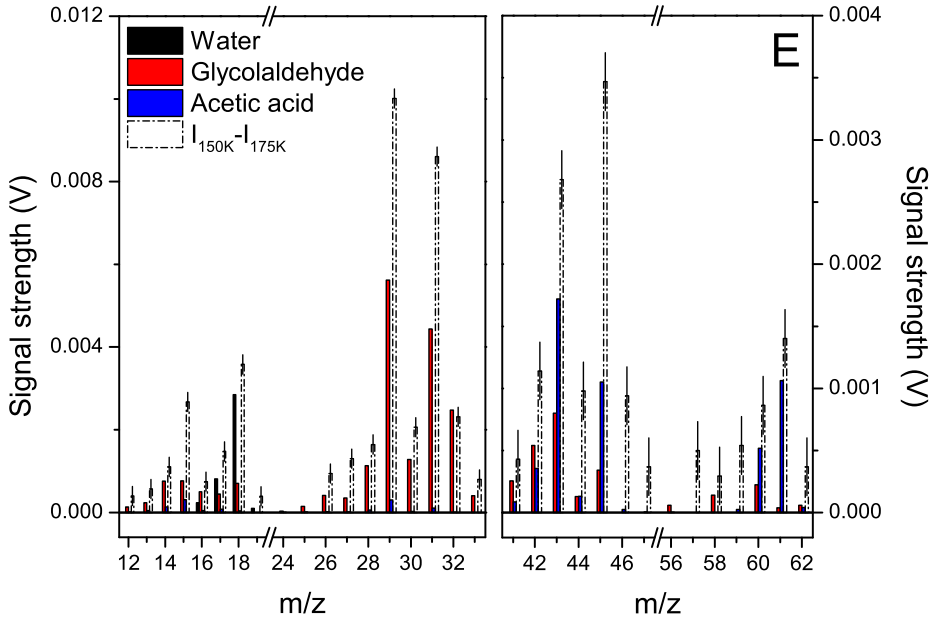

Figure 5.8: Ion mass fragmentation signals (black, red, and blue filled boxes) and integrated mass difference signal (open boxes) for T=150 and 175 K are shown for the m/z peaks that correspond to ion fragment masses of water, glycolaldehyde, and acetic acid for 70 eV electron impact. The derived uncertainty level is indicated for each difference signal.

Figure 5.8 compares the reference fragmentation patterns of water, glycolaldehyde, and acetic acid with the absolute difference between the mass spectra obtained at 150 and 175 K. These species are selected based on their desorption temperature in this temperature range (see also Table 5.2). It is clear that H_2O desorbs from the substrate; therefore, we confirm that H_2O is formed during the irradiation of CH_3OH-ice. The majority of the intensity differences is in agreement with the fragmentation patterns of glycolaldehyde and acetic acid, although differences are found for m/z = 29, 31, 44, 45, and 46. These may be due to remaining ethanol still present at 150 K (Öberg et al., 2009). In the sections below, the different temperature regimes with corresponding desorbing molecules are discussed separately.

A (20 − 50 K): Identification of CO and CH_4

The difference in peak intensity between the spectra acquired at 20 and 50 K is compared with the reference fragmentation patterns of CO and CH_4 (Fig. 5.9). After this temperature increase, a minor intensity decrease is observed in the mass range 12 to 16, indicating that part of the CH_4 formed in the ice has desorbed. We do not observe a clear decrease at m/z = 28, although it is expected that CO forms during photo-processing. Methane and carbon monoxide have been detected previously in photolysis studies using IR spectroscopy (Gerakines et al., 1996; Öberg et al., 2009). The limited decrease in intensity observed in our experiment is due to the large fraction of the species trapped in the methanol matrix; this has previously been observed with reflection-absorption IR spectroscopy (RAIRS) studies. At higher temperatures (100 K, as depicted in figure 5.10) m/z = 28 clearly decreases. Some other m/z values show a minor decrease; it is expected that this is caused by local rearrangement in the ice structure.

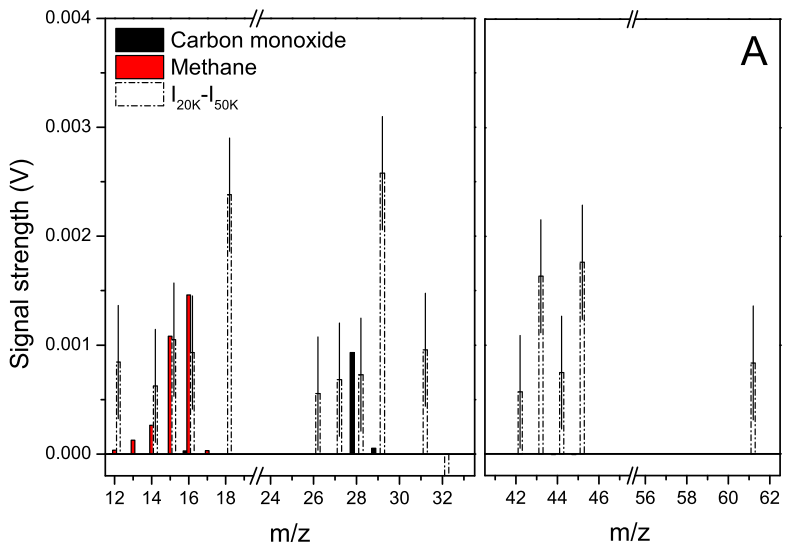

Figure 5.9: The ion mass fragmentation signals (black and red filled boxes) and integrated mass difference signal (open boxes) for T=20 and 50 K are shown for the m/z peaks that correspond to ion fragment masses of carbon monoxide and methane for 70 eV electron impact. On top of the difference signals the derived uncertainty level is indicated.

B (50 – 100 K): Identification of H_2CO, CH_3OCH_3 and CO_2

Figure 5.10 presents the difference in integrated intensity between mass spectra obtained at 50 and 100 K compared with reference fragmentation patterns of formaldehyde, dimethyl ether, and carbon dioxide. A decrease in the main fragmentation peaks of formaldehyde is observed. We also observe a decrease at m/z = 44, 45, and 46 indicating that CH_3OCH_3 has started desorbing from the ice. The decrease at m/z = 44 is consistent with the presence of carbon dioxide. Moreover, signal decreases at m/z = 26, 27, 42, and 43 are observed; m/z = 26 and 27 possibly originate from the fragmentation of ethane (C_2H_6), but an unambiguous assignment is not possible since the fragmentation pattern does not fully match. The decreased intensity at m/z = 42 and 43 is unexpected and not fully understood. The molecules H_2CO and CO_2 have been observed in several photolysis studies, (Gerakines et al., 1996; Öberg et al., 2009) and CH_3OCH_3 has been detected by Öberg et al. (2009).

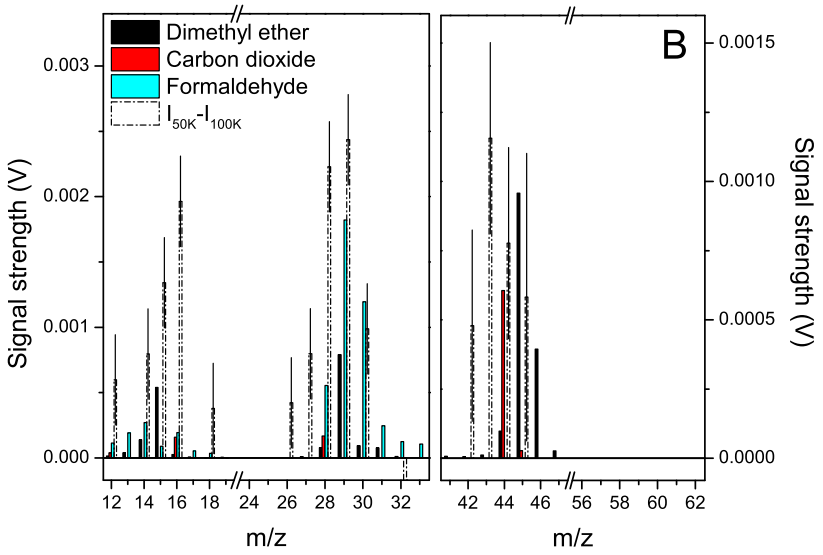

Figure 5.10: The ion mass fragmentation signals (black, red and cyan filled boxes) and integrated mass difference signal (open boxes) for T=50 and 100 K are shown for the m/z peaks that correspond to ion fragment masses of dimethyl ether, carbon dioxide and formaldehyde for 70 eV electron impact. On top of the difference signals the derived uncertainty level is indicated.

C (100 – 125 K): Identification of $HCOOCH_3$ and CH_3CHO

Figure 5.11 presents the changes in mass spectra during the temperature increase from 100 to 125 K compared to the reference fragmentation patterns of $HCOOCH_3$, CH_3CHO, and CH_3OCH_3. An intensity decrease at m/z = 44, 45, 46, and 58 up to 63 is observed. Part of this decrease is explained by the desorption of methyl formate for m/z = 59, 60, and 61, in agreement with the reported desorption temperature. We tentatively assign the decrease at m/z = 44 to the desorption of acetaldehyde (CH_3CHO), although it is clear that only a minor amount of this species is formed, in agreement with Öberg et al. (2009). It should be noted that during this temperature increase, a phase change to crystalline CH_3OH occurs (Bolina et al., 2005; Isokoski et al., 2014). Owing to this local rearrangement of the ice structure, trapped species can be released to the gas phase (Maity

et al., 2015). The local density of different species in the plume changes, and this affects the intensities at m/z = 61 and 63 (not depicted). The decrease at m/z in the 44-46 range is attributed to remaining dimethyl ether, which is expected to be still present in the ice. The desorption profiles are typically wide and therefore can contribute in two different temperature regimes, determined by the boundary values chosen here.

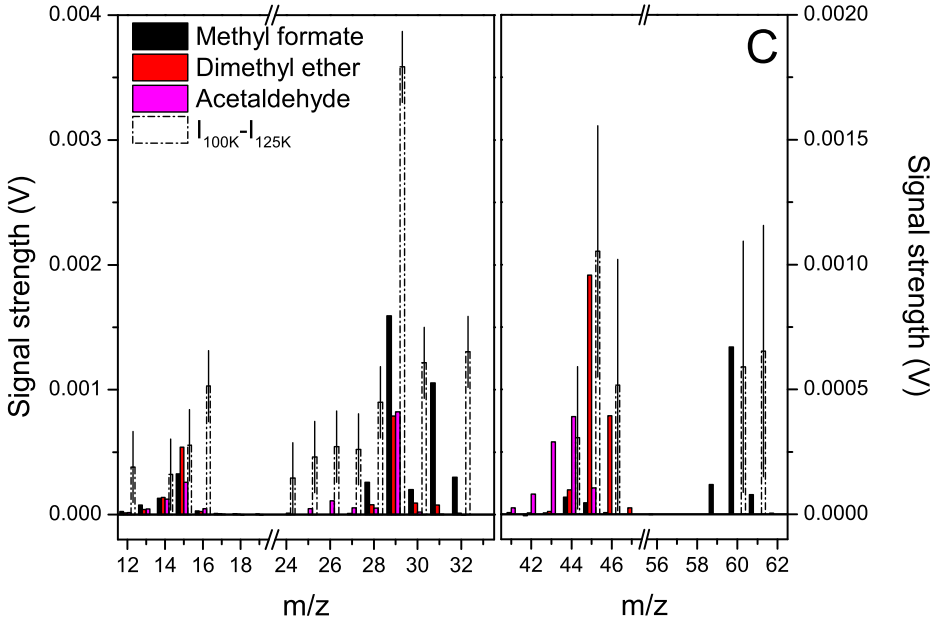

Figure 5.11: The ion mass fragmentation signals (black, red and magenta filled boxes) and integrated mass difference signal (open boxes) for T=100 and 125 K are shown for the m/z peaks that correspond to ion fragment masses of methyl formate, dimethyl ether and acetaldehyde for 70 eV electron impact. On top of the difference signals the derived uncertainty level is indicated.

D (125 − 150 K): Identification of CH_3OH, CH_3CH_2OH and HCOOH

After the temperature increase from 125 to 150 K, most of the methanol desorbs. As the ice is mainly made up of methanol, the remaining volatiles trapped in the matrix will desorb as well. The difference in intensity is depicted in figure 5.12 and is compared to the reference fragmentation patterns of methanol, ethanol, and formic acid. We observe a clear decrease for m/z = 45 and 46, the prominent peaks in the high-mass range of the fragmentation pattern of ethanol (CH_3CH_2OH). As expected, a decrease in intensity is observed for masses associated with methanol and the methanol clusters (see figure 5.7). A signal decrease at m/z = 47 is tentatively assigned as being due to a small desorbing portion of protonated formic acid. In the low-mass region, m/z = 12 to 18, a clear decrease is observed. Co-desorption of H_2O with the methanol matrix explains this.

E (150 − 175 K): Identification of H_2O, $HOCH_2CHO$, CH_3COOH and CH_3OCH_2OH

In figure 5.8, the fragmentation patterns of water, glycolaldehyde, and acetic acid are compared to the changes in the mass spectra after the temperature increase from 150 to 175 K. The formation of water upon energetic processing of methanol has been observed before

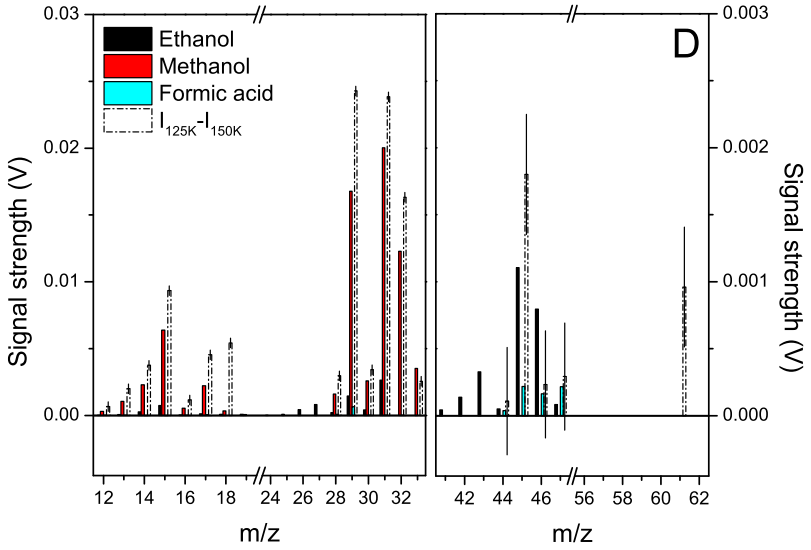

Figure 5.12: The ion mass fragmentation signals (black, red and cyan filled boxes) and integrated mass difference signal (open boxes) for T=125 and 150 K are shown for the m/z peaks that correspond to ion fragment masses of ethanol, methanol and formic acid for 70 eV electron impact. On top of the difference signals the derived uncertainty level is indicated.

(Henderson & Gudipati, 2015). Contributions from background deposition can be largely excluded, which has been confirmed by a background experiment. We assign the signal decrease at m/z = 42 and 56, 58, and 60 to the desorption of glycolaldehyde ($HOCH_2CHO$), and the decrease at m/z = 61, 60, 43, and 45 to the desorption of acetic acid (CH_3COOH). Reference spectra of acetic acid show the appearance at m/z = 61 assigned to protonated acetic acid $(CH_3COOH)H^+$. This mass peak has also been observed in VUV photoionisation studies of acetic acid clusters (Guan et al., 2012). An additional intensity decrease is observed at m/z = 45 and 46, which can be explained by the desorption of the remaining ethanol.

Efforts have been made to confirm the formation of methoxymethanol (CH_3OCH_2OH), which is expected to thermally desorb around 170 K. In previous studies (Boamah et al., 2014; Maity et al., 2015) a preliminary detection was claimed, following rather restricted literature information on the fragmentation pattern (Johnson & Stanley, 1991). The published mass spectrum shows intense peaks at m/z = 29, 30, 31, 33, 45, and 61, but has a low signal at the molecular ion mass, m/z = 62. In the 150 – 175 K temperature window, we do find a decrease in the dominant peaks consistent with methoxymethanol, indicating that it may be formed. However, we are cautious about this identification, since the published mass spectrum shows only a minor molecular ion peak and it is not possible to measure the full reference fragmentation pattern.

F (175 – 210 K): Identification of $(CH_2OH)_2$ and $HOCH_2CHOHCH_2OH$

During the temperature increase from 175 to 210 K, the amount of detected ions further decreases. The intensity decrease in the prominent m/z values is compared to the fragmentation pattern of ethylene glycol and acetic acid in figure 5.13. The decrease at m/z = 62 indicates that ethylene glycol, $(CH_2OH)_2$, has desorbed. Based on the desorption temper-

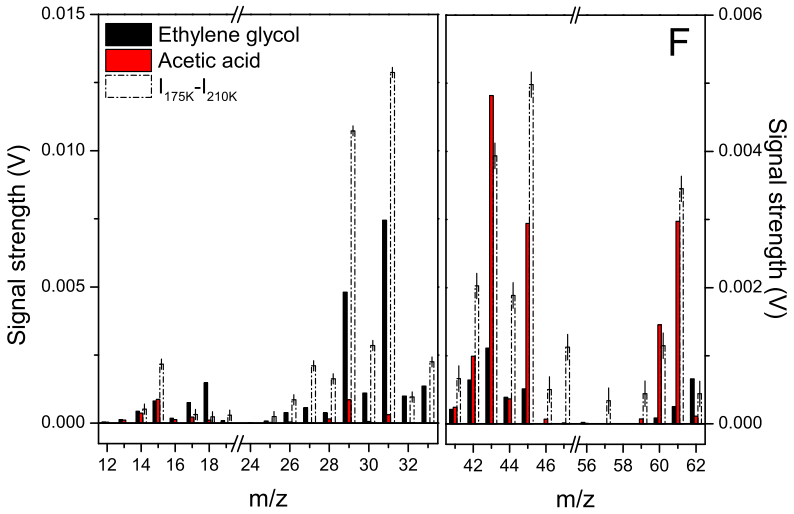

Figure 5.13: The ion mass fragmentation signals (black and red filled boxes) and integrated mass difference signal (open boxes) for T=175 and 210 K are shown for the m/z peaks that correspond to ion fragment masses of ethylene glycol and acetic acid for 70 eV electron impact. On top of the difference signals the derived uncertainty level is indicated.

atures of the molecules that we take explicitly into account, no decline for other species is expected. However, we do observe an intensity decrease for other masses, indicating that it is likely that more species are present. The observed decrease is in agreement with the fragmentation pattern of acetic acid, which thermally desorbs around 155 K (outside this range).

Since the substrate temperature is 210 K, all ethylene glycol has desorbed from the sample. This is confirmed by the absence of m/z = 62 in the mass spectrum at this temperature. As visible in figure 5.14, the mass spectrum obtained at 210 K still contains clear peaks at m/z = 43, 45, and 61, and traces at 42, 44 and 73, 74, 75. Owing to their high desorption temperature, COMs such as glycerin, glycolic acid, and glyceraldehyde could be the photo-products responsible for this observation. As previously mentioned, it is not possible with the current set-up to measure the fragmentation pattern of species with a negligible vapour pressure, such as glycerin and glycolic acid. Therefore, the interpretation of this mass spectrum has to be guided by the fragmentation standards that are available from the NIST database. Although the relative intensities differ, the fragmentation pattern matches the fragmentation pattern of glycerin ($HOCH_2CHOHCH_2OH$). The mass spectrum obtained at 210 K is compared with the fragmentation pattern of glycerin and glycolic acid in figure 5.14. We are unable to determine whether glycolic acid is present since the fragmentation pattern of glycolic acid strongly overlaps with the fragmentation pattern of glycerin, and both species have similar desorption temperatures.

It is important to note that ions at the same m/z values discussed here for very high temperatures are also observed at 20 K after 64 minutes of VUV irradiation, indicating that these species are also formed *at low temperature*. This shows that COMs with as many as six carbon/oxygen atoms (i.e. glycerin) form upon VUV photolysis of solid methanol for temperatures typical in dark interstellar clouds.

G: Non-detection of H_2CCO and $HOCH_2COOH$

We have tried to confirm the formation of ketene and/or glycolic acid. Ketene will thermally desorb at 123 K (Maity et al., 2014), but no unambiguous signals have been recorded. In the case of glycolic acid, the NIST database shows a relatively intense $m/z = 45$ value; unfortunately, this overlaps with the main fragments of glycerin, which desorbs at a similar temperature. Therefore, at this stage no unambiguous identifications can be made.

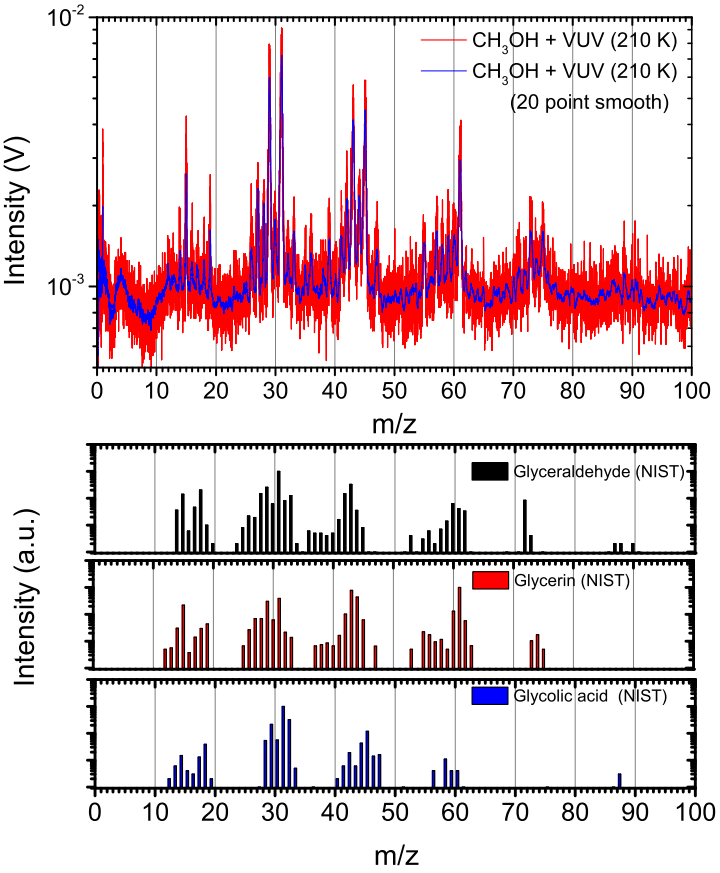

Figure 5.14: Mass spectrum of ~ 13.5 nm-thick methanol ice, deposited and VUV irradiated at 20 K for 64 minutes. The sample is heated up to 210 K before acquiring the mass spectrum, 70 eV electrons are used as an ionisation source. The experimental results are compared to the NIST fragmentation pattern of glyceraldehyde ($HOCH_2CHOHCHO$), glycerin ($HOCH_2CHOHCH_2OH$) and glycolic acid ($HOCH_2COOH$), for clarity plotted on logarithmic scale.

5.3.2.2 *Fitting library*

By fitting low-temperature data it is possible to obtain kinetic growth curves for individual species, which can aid in understanding the photo-chemistry at play. The selection of candidates for the fitting library is based on the experiments performed at elevated temperatures and is listed in Table 5.3. Since most of these molecules lead to identical

fragment ions, this fitting procedure is delicate and the output has to be interpreted with care. It should be noted that not all possible reaction products are included in the fit; it is likely that minor abundances of larger species are missed. Our approach is the following. We start with a selection of the fitting library, based on the species detected in RAIRS studies with a high abundance: $\geqslant 1\%$ (Öberg et al., 2009). Depending on the discrepancy between the fit and the data, additional species are selected to obtain a complete fit to all peaks.

Most species contain fragment ions below $m/z = 33$, while the larger fragment ions are strongly species dependent. By applying different weighting ratios to these m/z regions in the optimisation routine, it is guaranteed that the information provided by higher masses is taken into account appropriately. We increase the weighting of $m/z = 43, 58$ (glycolaldehyde), and 62 (ethylene glycol). Despite the rather large uncertainties, we have noticed in the fitting procedure anti-correlations between glycolaldehyde/methanol and between dimethyl ether/ethanol. The final fitting library is presented in Table 5.3 and does not contain acetaldehyde since the amounts detected are negligible. Methoxymethanol has also been excluded. The mass spectrum is first fitted using the library without glycolaldehyde. In a subsequent fit using a library containing glycolaldehyde, the methanol abundance is allowed to vary between 90% and 100%, while no further constraints are applied. Using this approach, the anti-correlation is prevented. Since dimethyl ether and ethanol have been detected using RAIRS (Öberg et al., 2009), their typical formation ratio is known.

Table 5.3: Electron-impact cross sections of species considered in the fitting routine.

Molecule	Chemical formula	σ_{70eV} (Å^2)	σ_{35eV} (Å^2)	Reference
Carbon monoxide	CO	2.44	1.43	Hudson et al. (2004)
Methane	CH_4	3.524	2.692	Kim et al. (1997)
Carbon dioxide	CO_2	3.15	1.41	Hudson et al. (2004)
Formaldehyde	H_2CO	4	3.2	Bhutadia et al. (2012)
Dimethyl Ether	CH_3OCH_3	8	4.2	Sugohara et al. (2013)
Methyl Formate	$HCOOCH_3$	6.9	4.6	Hudson et al. (2006)
Methanol	CH_3OH	4.44	2.98	Hudson et al. (2003)
Ethanol	CH_3CH_2OH	7.31	4.94	Hudson et al. (2003)
Water	H_2O	2.275	1.515	Kim & Rudd (1994)
Formic Acid	HCOOH	4.6	3.43	Bhutadia et al. (2012)
Acetic Acid	CH_3COOH	7.73	5.09	Bhutadia et al. (2012)
Glycolaldehyde	$HOCH_2CHO$	7.3	5.11	Bull & Harland (2008)
Ethylene Glycol	$(CH_2OH)_2$	6.17	4.15	Bhutadia et al. (2012)

5.3.2.3 *Fit*

Figure 5.15 shows the final fit of the mass spectrum of methanol after 64 minutes of VUV photolysis at 20 K, simultaneously fitted for two electron energies (35 and 70 eV) using equation 14. Mass spectra (A,B) were obtained using 35 eV electrons as an ionisation source, while mass spectra (C,D) were obtained using 70 eV electrons. The influence of changing the electron energy is clearly noticeable; 70 eV yields more severe fragmentation. The thin bars at different masses represent the integrated area of all individual mass peaks. Both spectra have been normalised to the mass peak with highest intensity. The different colours show the reference fragmentation pattern of different species and their contribution to the fit.

The final fit obtained is good, although isolated discrepancies exist. The m/z = 61 signal can only have a minor contribution from a cluster ion, so we expect that this discrepancy mainly originates from a photoproduct. One potential candidate is glycerin; the fragmentation pattern (Fig. 5.14) has a strong fragment ion at m/z = 61.

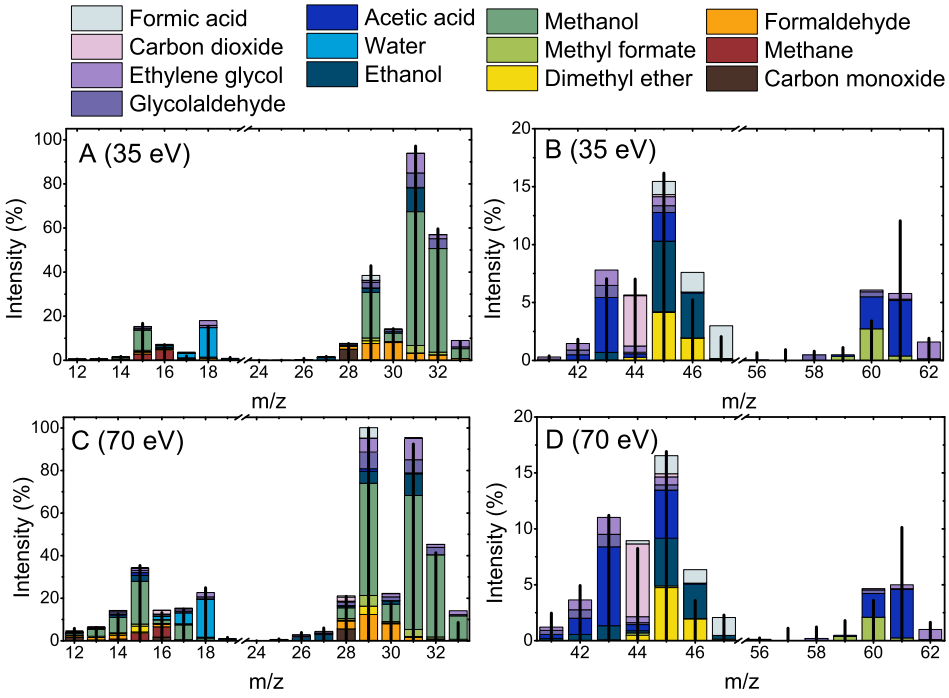

Figure 5.15: Fit of the different species contributing to the mass spectra obtained after 64 min VUV photolysis of CH_3OH at 20 K. The thin bars at different masses represent the integrated area of all individual mass peaks. The mass spectra are fitted simultaneously for two different electron-impact ionisation energies (35 eV, A+B and 70 eV, C+D). The fragmentation patterns of all individual species have been measured in reference experiments; see Table 5.3 for electron-impact ionisation cross sections.

5.3.2.4 *Kinetics*

Figure 5.16 presents the kinetic growth curve of new species that formed during the VUV photo-processing. The vertical scales are different for the four graphs shown here. As expected, methanol is consumed and leads to the formation of other species. Small species such as formaldehyde, methane, carbon monoxide, carbon dioxide, and water are formed. The amount of water detected is surprisingly high. We performed a reference experiment (no VUV processing) for 4 hours and we find that the amount of water deposition from background gas is negligible.

The formation of COMs such as methyl formate, ethylene glycol, dimethyl ether, and ethanol is shown in figure 5.16C. As mentioned in section 5.3.2.2, there is an anti-correlation when fitting contributions from dimethyl ether and ethanol. This is clearly visible in the graph, where also their combined intensity is depicted. Since these species are distinguishable with infrared spectroscopy (Öberg et al., 2009), the exact formation ratio can be

estimated. In figure 5.16D, the growth of glycolaldehyde, acetic acid, and formic acid is shown. Glycolaldehyde is detected, but the error bars are large owing to an increased uncertainty in the fit. Acetic acid and formic acid are better constrained and are clearly formed during the irradiation.

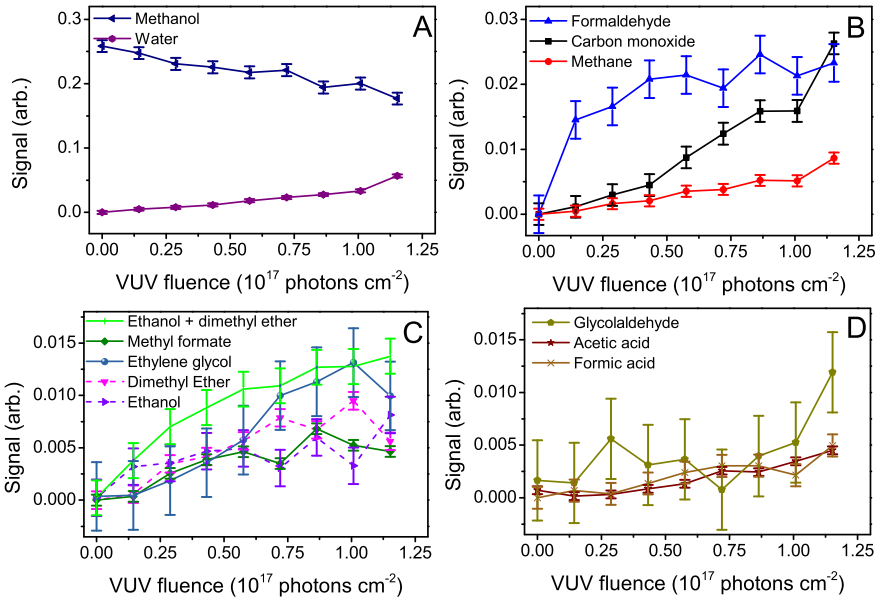

Figure 5.16: Formation efficiency of COMs as function of VUV photon fluence. The error bar is based on the standard deviation, determined using 8 measurements performed at 32 minutes of VUV photo-processing. Electron impact ionisation cross sections are taken into account which allows to compare the relative yields.

After the fitting procedure we would expect that at zero fluence the signal for all species except methanol should be zero. However, we note that the value relative to glycolaldehyde is different from zero before the photolysis starts. In fact, both methanol and glycolaldehyde have similar fragmentation patterns. In both cases the three most intense peaks are in m/z values of 29, 31, and 32. In the fitting routine we find that in some cases the glycolaldehyde fits part of the methanol mass data. It should be noted that IR spectroscopy suffers from the overlap of vibrational modes for these species and, consequently, it is hard to monitor the kinetics. This validates the efforts of employing different experimental techniques on the same systems.

5.4 DISCUSSION

5.4.1 *Comparison with previous experiments*

As stated in the introduction, the VUV processing of methanol ice has been studied using a variety of detection schemes over the last decades. IR spectroscopy (transmission and

RAIRS) have been used in combination with TPD/QMS. This has led to secure detections of small species, such as formaldehyde, carbon monoxide, carbon dioxide, and methane (Gerakines et al., 1996; Baratta et al., 2002; Bennett & Kaiser, 2007; Islam et al., 2014). This is in line with the results presented in this chapter.

Recent publications (Öberg et al., 2009; Boamah et al., 2014; Maity et al., 2014; Henderson & Gudipati, 2015; Mrad et al., 2016) on processing methanol ice using energetic electrons or photons have focused on detecting COMs. Sensitive detection schemes, such as TPD / SPI TOF-MS or two-step laser ablation and ionisation mass spectrometry, as well as TPD/QMS or GC-MS in conjunction with RAIRS have been applied. The detections reported in these studies are listed in Table 5.1. We did not include the long list of COMs detected in the GC-MS study by Mrad et al. (2016) as here the irradiation time of the methanol ice (3 days) is so much longer than in the present study that a direct comparison is not really possible. Nevertheless, many of their findings are fully in line with the data listed in the last column, which summarises the identifications in the present work. It is clear that COM formation starts with fluences comparable to those expected in the interstellar medium and the high sensitivity of MATRI^{2}CES allows them to be detected at an early stage in their solid state formation path. Many previous detections have now been confirmed with the guarantee that these form at low temperatures, and several tentative new detections have been reported as well. A straightforward comparison with results obtained by Öberg et al. (2009) is possible (Table 5.1, column 1). In that study RAIRS and TPD/QMS are used to study the photo-processing of methanol ice. There is a good overall qualitative agreement with the results presented here, but clearly some quantitative differences exist. In the case of small species such as CO, CO_2, and CH_4, we obtain different relative abundances because LDPI TOF-MS is less suitable for the quantification of these small species at low temperature than IR spectroscopy. On the contrary, LDPI TOF-MS allows the disentangling of the quantities of COMs that form at low temperature, providing greater insights into the photo-chemistry at play than IR spectroscopy.

The study of Boamah et al. (2014) uses low-energy electrons for processing (Table 5.1, column 2). A large number of COMs are detected, in agreement with the results presented in this paper. There is a qualitative difference for small species (CH_4, CO) owing to limitations in substrate temperature in that study.

Maity et al. (2014, 2015) has combined TPD with SPI TOF-MS (Table 5.1, column 3). This has lead to an extended list of COMs. Compared with the present study, some species, such as water, formic acid, and acetic acid, are likely to have formed during the ice processing. If present, these species will not have been detected, since their ionisation potential is higher than the photon energy used for ionisation.

Recently, Henderson & Gudipati (2015) have used two-step laser ablation and ionisation mass spectrometry on VUV and electron (2 keV) processed ices with the aim at detecting newly formed species. Comparing their results with those found here (Table 5.1, column 4), clear differences are found; the VUV experiments result in a higher level of molecular complexity, for which there may be different reasons. It is possible that the ice in the experiment of Henderson & Gudipati (2015) is too thick to be completely processed by the VUV photons. Another explanation is that the actual VUV flux reported in their study provides an upper limit as 10^{15} photons cm^{-2} s^{-1} is on the high side (Ligterink et al., 2015). It is also possible that the use of a UV laser as ionisation source – compared with electron impact that we use here – comes with a different efficiency. In particular the UV laser is expected to be more efficient in the ionisation of aromatic molecules than aliphatic ones.

It should be noted that even though the final products found in many of the studies listed here are comparable, the underlying processes are quite different. Photons with specific energies are expected to favour specific bond cleavage dissociation, whereas impacting elec-

trons will be less selective. On the other hand, the impact of a single high-energy electron can lead to a large number of secondary electrons, initiating a cascade of bond cleavages, forming radicals in the ice, which in turn can lead to the formation of new COMs.

5.4.2 *CH_3OH photo-dissocation branching ratio*

The formation of COMs depends on the abundance of radicals in the ice and their ability to meet and react. The fitted mass spectra contain information on the abundance of different photo-products. This provides information about the radicals that have successfully found a reaction partner Öberg et al. (see chemical network proposed by 2009)). Assuming that only one bond is broken the following radicals can be formed in the ice upon methanol photo-dissociation (Laas et al., 2011):

$$CH_3OH + h\nu \rightarrow CH_2OH + H \quad (16)$$
$$\rightarrow CH_3 + OH \quad (17)$$
$$\rightarrow OCH_3 + H \quad (18)$$

Since ethanol and dimethyl ether are strongly correlated in the fitting routine, as discussed in section 5.3.2.3, it is unreliable to directly use their abundance. Instead, we assume their formation ratio is the same as in the RAIRS study, (4 ± 2) (Öberg et al., 2009). Without a complete model, it is difficult to accurately determine the photo-dissociation branching ratio of CH_3OH. By tracing the abundance of different photoproducts, an estimate of the photo-dissociation branching ratio can be obtained. Based on the chemical network proposed by Öberg et al. (2009), the radicals of interest – hydroxymethyl, methyl, and methoxy – are traced. To form ethylene glycol, two hydroxymethyl radicals are necessary. To form glycolaldehyde, a formyl radical and a hydroxymethyl radical have to react. If we take into account the formation of ethylene glycol, glycolaldehyde, ethanol, methyl formate, and dimethyl ether, we obtain a branching ratio of $5:1$ between CH_2OH and OCH_3. The importance of the CH_3+OH branching is constrained by COMs that involve a methyl radical in their formation process. We opt for this approach rather than tracking OH-dependent species, since part of the observed water (an important sink for the OH radical) can be a contaminant. The methyl radical is involved in reactions towards methane, ethanol, and dimethyl ether. The hydroxymethyl and methoxy radical can both absorb another photon, which can lead to the formation of formaldehyde. As a first-order approximation, we assume that the formaldehyde is mainly formed through these two routes and that the formation efficiency for both radicals is the same. Since the CH_2OH and OCH_3 abundance is $5:1$, this indicates that 85% of the formaldehyde is formed from hydroxymethyl radicals and 15% from methoxy radicals. The final deduced branching ratio of methanol photodissociation into CH_2OH:CH_3+OH:OCH_3 amounts to 10:3:2.

So far in the analysis, the difference in mobility of radicals OCH_3, CH_3, and CH_2OH at 20 K has been neglected. Although diffusion of these radicals through a methanol matrix is difficult to assess, typically the order of the binding energy of the involved species is $CH_3 < OCH_3 < CH_2OH$ (Garrod et al., 2008; Öberg et al., 2009). This suggests that the CH_2OH+H branch may be underestimated and is even more dominant. The dominant branching channel found in this study is in agreement with Öberg et al. (2009). A more prominent CH_3 + OH branch is observed in this study, however.

5.4.3 *Glycerin formation mechanism*

The reaction between two hydroxymethyl radicals will lead to the formation of ethylene glycol. A subsequent absorption of a VUV photon can result in a dehydrogenation forming for example the $HOCHCH_2OH$ radical. If this radical reacts with another hydroxymethyl radical, this leads to the formation of glycerin (Kaiser et al., 2015). It is likely that for other reactions starting from solid ethylene glycol, more species with a complexity comparable to glycerin may form. This depends on local radical abundances and the exact position of the dehydrogenation event in ethylene glycol. One of the interesting species that can form through the recombination of $HOCHCH_2OH$ and HCO radicals is glyceraldehyde, a sugar of astrobiological importance. As stated above (Fig. 5.14), the mass spectrum contains peaks that would be consistent with the formation of this molecule, but given the lower intensity and overlapping features with other species this claim is preliminary. In the study by Mrad et al. (2016) where the long irradiation times result in a large variety of COMs, no proof for glycerin has been found.

5.5 ASTROPHYSICAL IMPLICATIONS AND CONCLUSIONS

Complex organic molecules have been detected in different environments in the interstellar medium, ranging from cold and hot cores to hot corinos and prestellar cores (Bacmann et al., 2012; Jørgensen et al., 2012; Coutens et al., 2015). With the Atacama Large Millimeter/submillimeter Array (ALMA) and Stratospheric Observatory for Infrared Astronomy (SOFIA) producing data and other facilities that will be online in the near future, it is expected that the number of identified COMs will steadily increase. The exact formation route of these molecules is still under debate, but it is generally accepted that COMs form on icy dust grains following thermal processing, irradiation by VUV light or X-rays, or bombardment by atoms, electrons, and cosmic rays.

One possible starting point is solid methanol formed by the hydrogenation of CO. Methanol is easily fragmented and recombination of the resulting radicals allows the formation of larger species. Indeed, methanol has been observed in the interstellar medium, both in the solid state and in the gas phase, and attempts have been made to link these abundances to those of COMs (Öberg et al., 2014). In the present study the VUV induced photochemistry of pure methanol ice has been studied in the laboratory with the goal of understanding which new molecules form and which processes are involved.

- Mass spectra obtained at different temperatures combined with in situ measured reference fragmentation patterns lead to unambiguous detection of the following species upon VUV photolysis of pure CH_3OH ice at 20 K:
  Carbon monoxide (CO), methane (CH_4), formaldehyde (H_2CO), carbon dioxide (CO_2), methyl formate ($HCOOCH_3$), acetaldehyde (CH_3CHO), dimethyl ether (CH_3OCH_3), ethanol (CH_3CH_2OH), water (H_2O), acetic acid (CH_3COOH), ethylene glycol ($(CH_2OH)_2$), formic acid (HCOOH-tentative), and glycolaldehyde ($HOCH_2CHO$). This is largely in line with Öberg et al. (2009); however, the present method extends the quantification of species that are indistinguishable using IR spectroscopy.

- Mass spectra obtained at high temperature (210 K) hint at the presence of glycerin ($HOCH_2CHOHCH_2OH$). This is the first possible experimental observation of glycerin in VUV processed methanol ice and suggests that molecular complexity in space may be beyond current astronomical detections.

- A qualitative analysis of the mass spectra obtained at low temperature indicates the detection of fragment ions originating from e.g. $(CO)_xH_y^+$, with $x = 3$ and $y < 3x-1$. This is the first detection of such species at low temperature. Large COMs such as $(CO)_xH_y^+$, with $x = 3$ and $y < 3x-1$, can be formed in the ice layers of interstellar dust grains.

- The study here also provides insight into the methanol branching ratios, at least for the applied experimental conditions. Based on our findings we estimate that the photodissociation branching ratio for methanol ice amounts to CH_2OH:CH_3+OH:OCH_3 = 10:3:2.

The experiments performed can be compared with corresponding processes in the interstellar medium by calculating the integrated energy deposited per methanol molecule. In dark clouds, the amount of energy deposited per water molecule has been estimated by Shen et al. (2004). It ranges from $\sim 1-100$ eV per water molecule after 10^7 years, depending on the assumed cosmic ray spectrum. Adapting recent measurements of solid state cross section values from Cruz-Diaz et al. (2014) for methanol $\sigma_{121.6nm} \approx 8.7 \cdot 10^{-18}$ cm^2, we calculate that the energy deposited per methanol molecule in a dark cloud is in the range $2.5-500$ eV after 10^7 years.

Using a similar approach, we can calculate the same quantity for experiments performed in the laboratory using equations 19 and 20:

$$A = 1 - e^{-\sigma_{av} \cdot N} \tag{19}$$

$$E_{abs} = \frac{A \cdot F \cdot E_{av} \cdot t}{N} \tag{20}$$

where A is the fraction of absorbed photons, σ_{av} the average cross section in cm^2, N the column density of absorbers in cm^{-2} determined using the thickness calibration, F the flux in photons cm^{-2} s^{-1}, E_{av} the average energy per photon in eV photon^{-1}, and t the time in seconds. Based on the emission profile of the lamp (Fig. 5.1), we can calculate the average photon energy E_{av} as 9 eV per photon. In addition, combining the emission profile with the reported methanol cross section (Cruz-Diaz et al., 2014) at multiple wavelengths (121.6, 157.8, and 160.8 nm), we estimate the average cross section (σ_{av}) of the methanol molecules to be $(3.7 \pm 0.4) \cdot 10^{-18}$ cm^2. These values are inserted into equation 20, which calculates the energy deposited per methanol molecule after 64 minutes of VUV irradiation and is in the range $2.3-4.6$ eV per methanol molecule. Compared to the energy deposit per methanol molecule in dark clouds ($2.5-500$ eV), the energy deposit in the laboratory experiments is at the low limit (Shen et al., 2004; Cruz-Diaz et al., 2014).

For higher fluences it is likely that the accessible complexity will increase further. This links the findings in the present work to the original studies in which long time irradiation of interstellar ice was performed by Bernstein et al. (2002); Muñoz Caro et al. (2002) and Mrad et al. (2016), illustrating the high sensitivity of LDPI TOF-MS as a technique to study COM formation in ice.

BIBLIOGRAPHY

Bacmann, A., Taquet, V., Faure, A., Kahane, C., & Ceccarelli, C. 2012, Astron. Astrophys., 541, L12
Baratta, G. A., Leto, G., & Palumbo, M. E. 2002, Astron. Astrophys., 384, 343
Baratta, G. A. & Palumbo, M. E. 1998, J. Opt. Soc. Am. A, 15, 3076
Bennett, C. J. & Kaiser, R. I. 2007, Astrophys. J., 661, 899
Bernstein, M. P., Dworkin, J. P., Sandford, S. A., Cooper, G. W., & Allamandola, L. J. 2002, Nature, 416, 401
Bhutadia, H., Vinodkumar, M., & Antony, B. 2012, J. Phys. Conf. Ser., 388, 052071
Boamah, M. D., Sullivan, K. K., Shulenberger, K. E., et al. 2014, Farad. Discuss., 168, 249
Bolina, A. S., Wolff, A. J., & Brown, W. A. 2005, J. Chem. Phys., 122, 044713
Boogert, A. C. A., Gerakines, P. A., & Whittet, D. C. B. 2015, Ann. Rev. Astron. Astrophys., 53, 541
Bossa, J.-B., Paardekooper, D. M., Isokoski, K., & Linnartz, H. 2015, Phys. Chem. Chem. Phys., 17, 17346
Briggs, R., Ertem, G., Ferris, J. P., et al. 1992, Origins. Life. Evol. B., 22, 287
Bull, J. N. & Harland, P. W. 2008, Int. J. Mass Spectrom., 273, 53
Chen, Y.-J., Chuang, K.-J., Muñoz Caro, G. M., et al. 2014, Astrophys. J., 781, 15
Chuang, K.-J., Fedoseev, G., Ioppolo, S., van Dishoeck, E. F., & Linnartz, H. 2016, Mon. Not. R. Astron. Soc., 455, 1702
Coutens, A., Persson, M. V., Jørgensen, J. K., Wampfler, S. F., & Lykke, J. M. 2015, Astron. Astrophys., 576, A5
Cruz-Diaz, G. A., Muñoz Caro, G. M., Chen, Y.-J., & Yih, T.-S. 2014, Astron. Astrophys., 562, A119
Cuppen, H. M., Penteado, E. M., Isokoski, K., van der Marel, N., & Linnartz, H. 2011, Mon. Not. R. Astron. Soc., 417, 2809
Es-sebbar, E.-t., Bénilan, Y., Fray, N., et al. 2015, Astrophys. J. Suppl. Ser., 218, 19
Focsa, F. & Destombes, J. 2001, Chem. Phys. Lett., 347, 390
Fuchs, G. W., Cuppen, H. M., Ioppolo, S., et al. 2009, Astron. Astrophys., 505, 629
Garrod, R. T., Weaver, S. L. W., & Herbst, E. 2008, Astrophys. J., 682, 283
Gerakines, P. A., Schutte, W. A., & Ehrenfreund, P. 1996, Astron. Astrophys., 312, 289
Guan, J., Hu, Y., Zou, H., et al. 2012, J. Chem. Phys., 137,
Hama, T. & Watanabe, N. 2013, Chem. Rev., 113, 8783
Henderson, B. L. & Gudipati, M. S. 2015, Astrophys. J., 800, 66
Hudson, J. E., Hamilton, M. L., Vallance, C., & Harland, P. W. 2003, Phys. Chem. Chem. Phys., 5, 3162
Hudson, J. E., Vallance, C., & Harland, P. W. 2004, J. Phys. B, 37, 445
Hudson, J. E., Weng, Z. F., Vallance, C., & Harland, P. W. 2006, Int. J. Mass Spectrom., 248, 42
Hudson, R. L. & Moore, M. H. 2000, Icarus, 145, 661
Hudson, R. L., Moore, M. H., & Cook, A. M. 2005, Adv. Space Res., 36, 184
Islam, F., Baratta, G. A., & Palumbo, M. E. 2014, Astron. Astrophys., 561, A73
Isokoski, K., Bossa, J.-B., Triemstra, T., & Linnartz, H. 2014, Phys. Chem. Chem. Phys., 16, 3456
Johnson, R. A. & Stanley, A. E. 1991, Appl. Spectrosc., 45, 218
Jørgensen, J. K., Favre, C., Bisschop, S. E., et al. 2012, Astrophys. J. Lett., 757, L4
Kaiser, R. I., Maity, S., & Jones, B. M. 2015, Angew. Chem., 127, 197
Kim, Y.-K., Hwang, W., Weinberger, N., Ali, M., & Rudd, M. 1997, J. Chem. Phys., 106, 1026
Kim, Y.-K. & Rudd, M. E. 1994, Phys. Rev. A, 50, 3954
Laas, J. C., Garrod, R. T., Herbst, E., & Widicus Weaver, S. L. 2011, Astrophys. J., 728, 71
Lagarias, J., Reeds, J., Wright, M., & Wright, P. 1998, SIAM. J. Optim., 9, 112
Ligterink, N. F. W., Paardekooper, D. M., Chuang, K.-J., et al. 2015, Astron. Astrophys., 584, A56
Linnartz, H., Ioppolo, S., & Fedoseev, G. 2015, Int. Rev. Phys. Chem., 34, 205
Maity, S., Kaiser, R. I., & Jones, B. M. 2014, Farad. Discuss., 168, 485
Maity, S., Kaiser, R. I., & Jones, B. M. 2015, Phys. Chem. Chem. Phys., 17, 3081
Moore, M. H. & Hudson, R. L. 2005, in IAU Symposium, Vol. 231, Astrochemistry: Recent Successes and Current Challenges, ed. D. C. Lis, G. A. Blake, & E. Herbst, 247–260
Mrad, N. A., Duvernay, F., Chiavassa, T., & Danger, G. 2016, Mon. Not. R. Astron. Soc.
Muñoz Caro, G. M., Meierhenrich, U. J., Schutte, W. A., et al. 2002, Nature, 416, 403

Öberg, K. I., Garrod, R. T., van Dishoeck, E. F., & Linnartz, H. 2009, Astron. Astrophys., 504, 891

Öberg, K. I., Lauck, T., & Graninger, D. 2014, Astrophys. J., 788, 68

Paardekooper, D. M., Bossa, J.-B., Isokoski, K., & Linnartz, H. 2014, Rev. Sci. Instrum., 85, 104501

Penteado, E. M., Boogert, A. C. A., Pontoppidan, K. M., et al. 2015, Mon. Not. R. Astron. Soc., 454, 531

Schwarz-Selinger, T., Preuss, R., Dose, V., & von der Linden, W. 2001, J. Mass Spectrom., 36, 866

Shen, C. J., Greenberg, J. M., Schutte, W. A., & van Dishoeck, E. F. 2004, Astron. Astrophys., 415, 203

Sugohara, R. T., Homem, M. G. P., Iga, I., et al. 2013, Phys. Rev. A, 88, 22709

van Dishoeck, E. F. 2014, Farad. Discuss., 168, 9

Watanabe, N. & Kouchi, A. 2002, Astrophys. J. Lett., 571, L173

Weast, R. 1972, Handbook of Chemistry and Physics 53rd Edition, Vol. E-207 (Chemical Rubber Pub.)

6

A NOVEL APPROACH TO MEASURE PHOTODESORPTION RATES OF INTERSTELLAR ICE ANALOGUES

Context. In recent years photodesorption rates have been determined in dedicated laboratory experiments for a number of different interstellar ice analogues. Such rates are important to model non-thermal desorption processes that, for example, affect gas-phase abundances of species and determine the position of snow lines in protoplanetary disks. However, different groups using similar experiments have found deviating photodesorption values.
Aims. Here a new measurement concept is introduced that allows to determine photodesorption rates following a different experimental approach. The potential of this method is demonstrated on the example of pure CO ice, the solid for which the discrepancies in the results are most striking.
Methods. The new experimental approach uses laser desorption electron impact ionisation time-of-flight mass spectrometry. It is based on the concept that the physical and geometrical properties of the plume obtained by laser induced desorption of the ice directly depend on the original ice thickness. This allows to determine the ice loss as function of Vacuum UltraViolet (VUV) fluence which results in a photodesorption rate. The method has the additional advantage that it records *all* desorbing species, i.e., including any resulting photoproducts. As a consequence, the method introduced here is also suited to determine the overall photodesorption rate of mixed ices.
Results. The photodesorption rate for CO ice at 20 K has been determined as $(1.4 \pm 0.7) \cdot 10^{-3}$ molecules per incident VUV photon. This result is compared to the existing experimental and theoretical values, reported so far, and the astronomical relevance is discussed.

D. M. Paardekooper, G. Fedoseev, A. Riedo and H. Linnartz, *A novel approach to measure photodesorption rates of interstellar ice analogues, the photodesorption rate of CO ice reinvestigated*, (submitted to Astron. Astrophys.)

6.1 INTRODUCTION

Astronomical surveys reveal the presence of gas phase molecules in dense and cold regions of the interstellar medium (ISM), where these are expected to be frozen out on top of submicron sized dust grains (Piétu et al., 2007; Caselli et al., 2012; Vastel et al., 2014). This observation indicates that there must exist an ongoing process that allows these species to form in the gas phase or that continuously replenishes them from a solid state reservoir. The latter is more likely, as for CH_3OH, for example, only efficient surface formation routes are known (Watanabe & Kouchi, 2002; Fuchs et al., 2009; Linnartz et al., 2015). Clearly, non-thermal desorption processes are at play. Various mechanisms have been proposed, including cosmic ray spot heating of the grains (Leger et al., 1985), chemical desorption, i.e., desorption due to excess energy of a surface reaction (Dulieu et al., 2013; Chang & Herbst, 2016) and Vacuum UltraViolet (VUV) induced photodesorption. Particularly, photo induced desorption processes have attracted considerable interest, starting in 1995 with the experimental measurement of the photodesorption rate of water ice (Westley et al., 1995a,b) and more recently (since 2007) for a large number of other ices (see for an overview: Ioppolo et al., 2014).

In cold and dense molecular clouds, the interstellar radiation field is strongly attenuated due to shielding by dust grains, but penetrating cosmic rays can excite H_2 and the resulting emission typically peaks at Ly-α wavelengths (Prasad & Tarafdar, 1983; Gredel et al., 1989; Shen et al., 2004). Molecules condensed on top of cold dust grains, or alternatively, formed in the ice layers, can photodesorp following VUV excitation, transfering solid state species into the gas phase. Later on in the star and planet formation sequence, also light from the young stellar object becomes important, determining for example the position of photo-induced snowlines (Öberg et al., 2015). Therefore, accurate photodesorption rates are needed to quantify the role (inter)stellar radiation has on abundances in the solid state and gas phase in different astronomical environments, varying from molecular clouds (Hollenbach et al., 2009) to protoplanetary disks (Willacy & Langer, 2000; Drozdovskaya et al., 2014; Walsh et al., 2015).

A large number of extensive laboratory studies has been reported on the photodesorption behavior of interstellar ices. Particularly pure carbon monoxide (CO) ice has been in the spotlights. The low accretion temperature of CO, effectively results in a CO coating on top of the ice covered dust grain. Using a H_2 microwave discharge lamp, emitting at Ly-α and around 160 nm, Öberg et al. (2007, 2009b) studied the (non-dissociative) photodesorption of CO ice. The resulting value, $(2.7 \pm 1.3) \cdot 10^{-3}$ molecules photon^{-1} measured at 15 K, was much higher than used at that moment in astrochemical models (Draine & Salpeter, 1979; Hartquist & Williams, 1990). Similar experiments by other groups (Muñoz Caro et al., 2010; Chen et al., 2014; Muñoz Caro et al., 2016), found deviating and even higher values, in the 10^{-2} to 10^{-1} molecules per photon range. A possible explanation for these deviations was searched for in the spectral emission pattern of the used broad band light sources that turned out to be more sensitive on the parameter settings than assumed (Chen et al., 2014; Es-sebbar et al., 2015; Ligterink et al., 2015). This assumption was in line with wavelength dependent CO photodesorption rates recorded at the DESIRS beamline of the SOLEIL synchrotron facility (Fayolle et al., 2011) that showed that the photodesorption of CO follows a wavelength dependent DIET (desorption induced by electronic transition) mechanism that is found to be more effective around 160 nm than at Ly-α. The CO photodesorption rate furthermore strongly depends on the deposition temperature as discussed by several groups (Öberg et al., 2009b; Muñoz Caro et al., 2010, 2016). In parallel, many more studies were performed, on other pure ices, including H_2O, N_2, CO_2, $O_2(O_3)$, and CH_3OH, as well as a few mixed ices, CO:N_2, CO:H_2O and CO:CH_3OH (Öberg et al., 2009a; Hama et al., 2010; Chen et al., 2011; Bahr & Baragiola,

2012; Bertin et al., 2012; Fayolle et al., 2013; Bertin et al., 2013; Yuan & Yates, 2013; Fillion et al., 2014; Zhen & Linnartz, 2014; Martín-Doménech et al., 2015; Bertin et al., 2016). In many of these studies it became clear that upon VUV photolysis, molecules not only photodesorb, but may also be involved in photo induced reactions (Öberg, 2016) substantially complicating the analysis, as photoproducts may photodesorb as well (see e.g., the discussion on O_2 and O_3 photodesorption upon VUV irradiation of O_2 ice in Zhen & Linnartz (2014)). A number of theoretical studies (Galloway & Herbst, 1994; Dzegilenko et al., 1995; Andersson et al., 2006; Andersson & van Dishoeck, 2008; Arasa et al., 2010, 2011; van Hemert et al., 2015; Arasa et al., 2015) focussed on the molecular processes at play, confirming the high level of complexity involved.

In the majority of the beforementioned laboratory studies, photodesorption rates have been obtained using two different methods, based on IR (transmission or reflection) spectroscopy or mass spectrometry (Ioppolo et al., 2014). In the first case a decreasing IR signal reflects the loss in surface abundance of molecules that is monitored as function of VUV fluence while in the latter case the gas-phase abundance of the desorbing species is measured. Both methods allow to derive quantitative values, as both IR and mass signals can be linked to absolute molecule numbers. IR spectroscopy only allows to monitor polar species directly. A decreasing IR spectrum with time reflects the loss rate of a specific molecule upon irradiation, but this does not allow to discriminate between a signal decrease because of a direct photodesorption process or because of a decrease in the precursor abundance due to a photochemical process. In this case photodepletion is a better way describing the processes taking place. Moreover, for larger molecules spectral congestion and spectral overlaps cause additional problems. Mass spectrometry overcomes many of these problems, however the conversion between gas phase mass signals and absolute photodesorption rates is challenging. In the present study, the photodesorption of pure CO ice is investigated using a different experimental concept. By means of laser desorption, complete desorption of the ice is realized at the laser spot. The resulting desorption plume is characterised for a series of different extraction times using electron impact ionisation in conjunction with time-of-flight mass spectrometry. The absolute intensity of specific mass to charge (m/z) signals provides information of the thickness of the ice at a specific time (read; for a specific fluence), while each time-of-flight spectrum contains information on the possible photoproducts. This measurement concept is explained in detail in the next section. The applications are illustrated in section 6.3 and discussed, along with the astronomical relevance, in section 6.4

6.2 EXPERIMENTAL METHODS

6.2.1 *Experimental setup*

The experiments have been carried out in our ultra-high vacuum setup MATRI^{2}CES, described in detail in Chapter 2 (Paardekooper et al., 2014). Briefly, MATRI^{2}CES consists of two different ultra-high vacuum (UHV) chambers, a main chamber and a time-of-flight chamber. The base pressure of these chambers is in the 10^{-10} mbar range. The main chamber hosts a gold-coated Cu substrate in thermal contact with a closed-cycle He cryostat, enabling substrate temperatures down to 20 K. The absolute temperature accuracy is better than ± 1 K, while the relative precision is ± 0.25 K. The cryostat is mounted on top of two translators (x,z) which enable to systematically probe different surface spots. The vertical (z) translation stage is fully motorised. Control of substrate temperature is achieved using a resistive heater element, a thermocouple and a Lakeshore temperature regulator. Ices can be grown on top of the cold substrate by leaking in gas-phase species through an all-metal needle valve attached to a capillary. CO gas has been used without

further purification (CO, 4.7 Praxair).

The deposition rate of the individual species is determined by HeNe laser interference measurements. Details of this procedure are provided in section 6.2.2. Photodesorption of the ice is induced using VUV photons produced by a microwave H_2 discharge lamp. The lamp (borosilicate) has a F-type design (Ligterink et al., 2015), and is evacuated using a scroll pump. The plasma is powered by a Sairem microwave generator using an Evenson cavity. The plasma is ignited using a high frequency generator. Typical settings amount to 0.85 mbar of H_2 and 80 W of applied microwave power. This lamp directly faces the ice sample through an UHV compatible MgF_2 window that is positioned 14 cm from the substrate. The VUV flux calibration procedure is described in section 6.2.3.

The used detection scheme is based on Laser Desorption Post-Ionization Time-Of-Flight Mass Spectrometry (LDPI TOF-MS). The desorption of the ice sample is induced using the unfocused, skimmed beam (~1 mm) of the third harmonic of a Nd:YAG laser (355 nm, 4-5 ns). The pulse power of the laser is reduced using an attenuator, resulting in a typical laser pulse energy of ~ 35 mJ cm^{-2}, ensuring full desorption of the ice at the impacting spot. Subsequently, the desorbed species are ionised by electrons with a mean energy of 70 eV using an electron impact ionisation source. The generated ions are extracted by ion optics, situated in close vicinity of the cold substrate and directed into the time-of-flight chamber. The ions drift and are separated based on their mass to charge (m/z) ratios, after which they are detected by a Micro Channel Plate (MCP) detector. The resulting signal is then digitized by a Data Acquisition (DAQ) card.

Complete desorption of the ice at the laser spot is needed to guarantee that the desorption plume contains all information about the original ice thickness of the sample. The detailed characterisation of the plume structure is performed in the following way. After each laser pulse, the extraction grid is triggered sequentially every 20 µs (pulse width = 1 µs) and a single time-of-flight spectrum is recorded. This single spectrum contains information of different parts of the desorption plume. By changing the relative timing between the first extraction trigger and the laser pulse from 0, 5, 10 to 15 µs, the complete plume structure with 5 µs resolution can be unravelled. The timing sequence is obtained using two coupled pulse generators (DG535, Stanford Research Systems), running at 10 Hz and 50 kHz. The lower frequency triggers the laser (flash lamp and Q-switch) and the acquisition of the DAQ card. The higher frequency triggers the extraction grid multiple times during every cycle of the lower frequency pulse generator. In parallel, the vertical translator moves down with constant velocity, while different spots of the sample are desorbed. A total of 44 time-of-flight traces are obtained for each extraction time (0, 5, 10 and 15 µs). Next to the multi extraction trigger TOF spectrum described above, TOF spectra with enhanced signal-to-noise ratio (SNR) can be obtained using a single extraction trigger. A custom-made LabVIEW routine controls the full experimental procedure including the data acquisition.

6.2.2 *Deposition rate calibration*

The deposition rate of CO has been determined using HeNe-laser interference measurements (Baratta & Palumbo, 1998; Bossa et al., 2015). An intensity stabilised HeNe-laser (Thorlabs HRS015) is used as a light source. The laser beam is polarised by means of a transmissive s-polariser and aimed at the sample with a 1.2° (θ_0) incident angle. The reflected beam is recorded by a photodiode (Thorlabs PDA36A), using an oscilloscope to digitize the signal (Tektronix 2022B). A custom-made LabVIEW program is used to record both time and photodiode signal.

The deposition rate (Γ in molecules cm^{-2} s^{-1}) is determined by combining equations 21 and 22.

$$d = \frac{\lambda}{2n_1/n_0 \cdot \cos(\theta_f)} \tag{21}$$

$$\Gamma = \frac{d \cdot \rho \cdot N_a}{M \cdot t} \tag{22}$$

where d corresponds to the thickness increase during subsequent interference maxima in nm, λ is the wavelength of the laser (632.8 nm), n_0 and n_1 are the refractive indices of vacuum and ice, θ_f is the angle of refraction in the ice in degree, ρ is the density in g cm^{-3}, N_a is Avogradro's constant ($6.022 \cdot 10^{23}$ mol^{-1}), M is the molar mass of the species and t is the time in seconds.

In this way, for carbon monoxide ice growing at 20 K, a deposition rate is obtained of $1.7 \cdot 10^{13}$ molecules cm^{-2} s^{-1} using a density of 0.80 g cm^{-3} and n_1=1.27 (Roux et al., 1980). It is important to note that throughout this article the ice thickness has been converted to the surface coverage, in molecules cm^{-2}, which has the same dimensions as a column density.

6.2.3 *Photon flux calibration*

As stated before CO has different photodesorption rates for these wavelengths and consequently it is important to know the SED characteristics of the lamp. Therefore, the spectral energy distribution (SED) of the microwave powered H_2-discharge lamp has been measured in advance using an absolute calibrated VUV spectrometer (Ligterink et al., 2015). The resulting spectrum has been presented in Chapter 5 Paardekooper et al. (2016). The emission profile predominately contains photons at Ly-α and additionally has contributions from molecular hydrogen at 160 nm. The photon flux at sample distance has been measured using a 1 cm^2 NIST calibrated AXUV-100 photodiode. The photocurrent is determined with a Keithley 485 picoammeter. It should be noted that not only the Ly-α and 160 nm emissions, but also visible photons can contribute to the observed photocurrent. In order to deconvolute the contribution of the latter, the emission of a sealed plasma lamp has been measured with the same plasma conditions. The sealed plasma lamp absorbs all VUV photons ($\lambda < 300$ nm), and has a transmittance of (90 ± 3)% in the visible regime.

Both the SED of the discharge lamp and quantum efficiencies at different wavelength of the NIST photodiode are known. Therefore, the effective quantum efficiency can be determined. The VUV photon flux is then derived using equation 23:

$$F(\lambda) = \frac{i(\lambda)}{e \cdot \epsilon(\lambda)} \tag{23}$$

with $i(\lambda)$ the photocurrent (resulting from VUV photons) in Ampere, e the electron charge ($1.602 \cdot 10^{-19}$ C) and $\epsilon(\lambda)$ the quantum efficiency, i.e., electron per exposed photon. At sample location, the VUV flux for the settings given before, is determined to be $(2.3 \pm 0.4) \cdot 10^{14}$ photons cm^{-2} s^{-1}.

6.2.4 *Detection scheme*

The plume structures are recorded using a multi trigger time-of-flight scheme for different surface coverages (e.g., different deposition times). These calibration measurements allow us to directly link plume structures to the surface coverage. In the case of CO, the plume

structures have been recorded for surface coverages ranging from $4 \cdot 10^{15}$ to $8 \cdot 10^{15}$ CO molecules cm^{-2}.

Subsequently, a fresh ice with a surface coverage of $8 \cdot 10^{15}$ CO molecules cm^{-2} ice is prepared and then processed using VUV photons produced by the H_2 discharge lamp. The VUV photons induce desorption following a constant parameter defined by the photodesorption rate. The plume structure resulting upon laser desorption, is measured after different times, i.e. at different VUV fluence, from which the surface coverage can be unravelled. After photo-processing of the ice, different column positions can be selected by shifting the horizontal translator (x). Between subsequent measurements, the sample is returned to the reference position, in order to guarantee full overlap between VUV photons and the ice sample. In an area where the ice growth is homogenous, 4 columns are selected for plume profile characterisation.

Combined with the VUV photon flux measurement, this allows to quantitatively determine the photodepletion rate. At this stage it is important to discriminate between photodesorption and photodepletion. Photodesorption is defined as the mechanism where molecules in the ice evaporate (in)directly upon absorption of a VUV photon, whereas photodepletion takes into account also the effect of photochemistry. In the case of CO the role of photochemistry will be limited, given the high binding energy. Even though negligible on the final photodesorption value, the process can be visualized with our new approach, as will be discussed later. Compared to regular photodesorption studies utilising IR spectroscopy and quadrupole mass spectrometry, this approach has the additional advantage that *all* ice constituents from the ice can be traced. The plume structure contains direct information of the surface coverage of the ice, while at the same time other products resulting from photochemistry are detected. This provides a generally applicable method

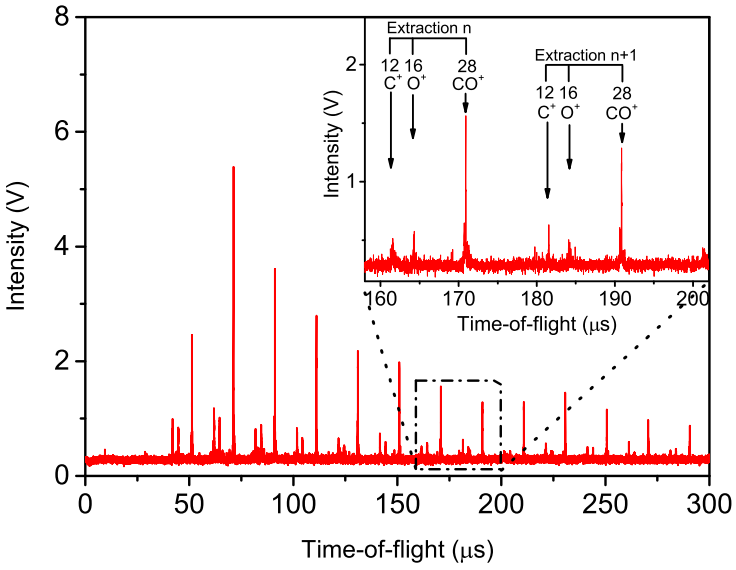

Figure 6.1: Time-of-flight spectrum of laser induced desorbed CO ice ($8 \cdot 10^{15}$ molecules cm^{-2}) using multiple extraction pulses with a time spacing of 20 μs. The inset shows two sequential extractions including the mass calibration. This spectrum is the sum of 44 individual spectra.

to determine also the photodesorption rate of (mixed) ices. This is not that relevant for CO, as pure CO ice is expected to exist, until it gets mixed with hydrogenation products such as H_2CO and CH_3OH (Fuchs et al., 2009; Cuppen et al., 2010). Many other species are expected to exist only in intimately mixed geometries.

6.3 RESULTS

6.3.1 *Plume characterisation of laser desorbed CO ice*

Figure 6.1 shows a typical time-of-flight trace obtained using multiple extraction pulses of a CO ice with a substrate coverage of $8 \cdot 10^{15}$ molecules cm^{-2}. Compared to previous measurements on MATRI^{2}CES the SNR for these spectra is lower; this is a direct result of the increased number of extraction pulses per time-of-flight spectrum combined with less averages per spectrum. Since the number of extraction pulses has increased, more ions are allowed to enter the time-of-flight chamber, leading to a higher noise level. The desorbed species are ionised using the electron impact ionisation source, which leads to both ionisation and dissociation of the species. In the case of CO, the number of resulting species is limited and this results into CO^+, C^+ and O^+. As shown in the inset of figure 6.1, all these ions are observed within each individual extraction pulse.

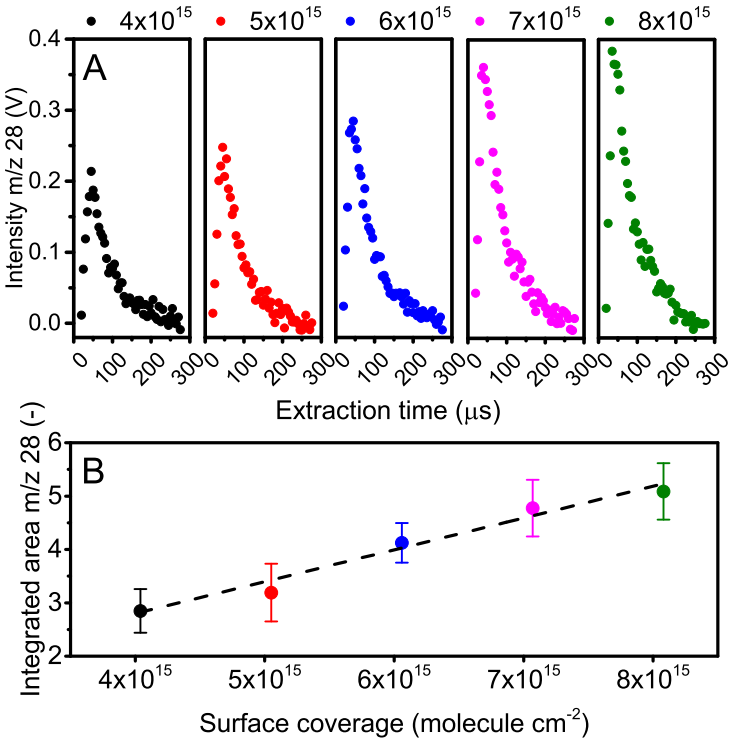

Figure 6.2: Upper panel (A): plume profiles observed for m/z=28 for different CO substrate coverages ranging from $4 \cdot 10^{15}$ molecules cm^{-2} to $8 \cdot 10^{15}$ molecules cm^{-2} upon laser induced desorption. Lower panel (B): integrated area of m/z = 28 of the complete plume profiles, for the corresponding surface coverages (same color coding).

By changing the relative timing of the laser and the extraction pulse, the complete desorption profile of the plume can be characterised. In figure 6.2A the plume profiles for different CO substrate coverages are depicted. The plume profiles are well described using a time dependent Boltzmann equation (equation 24).

$$S(t, T_{trans}) = A \cdot t^{-4} \cdot e^{\frac{-m \cdot r^2}{2 \cdot k_b \cdot t^2}} \tag{24}$$

Where A is a scaling factor, T_{trans} the translational energy, t the time, m the mass of the molecule, r is the distance travelled and k_b the boltzmann constant (DeSimone et al., 2013). Assuming that most ions originate from the center of the extraction optics ($\pm$ 2.5 mm), the translation energy ranges between $(2 \pm 1) \cdot 10^2$ K.

Using the calibration of the plume profiles for different CO surface coverages presented in figure 6.2B, it is now possible to track the surface coverage of CO ice for different VUV fluences.

6.3.2 *Photodesorption of CO ice at 20 K*

Figure 6.3 shows an overview of the experiments performed in order to derive with this method the CO photodepletion rate. Substrate coverages of CO molecules at different VUV fluences are shown. For clarity the experiments covering different thickness regimes are presented with a horizontal offset to be aligned. Previous studies reported that the top ~ 4 to 6 monolayers (1 ML = 10^{15} molecules cm^{-2}) (Muñoz Caro et al., 2010; Fayolle et al., 2011) play a role in the photodesorption process. Below this substrate coverage, the photodesorption rate drops, and therefore the main set of our experiments is performed in a range where the photodesorption rate is expected to be constant, i.e., for surface coverages above 4 ML.

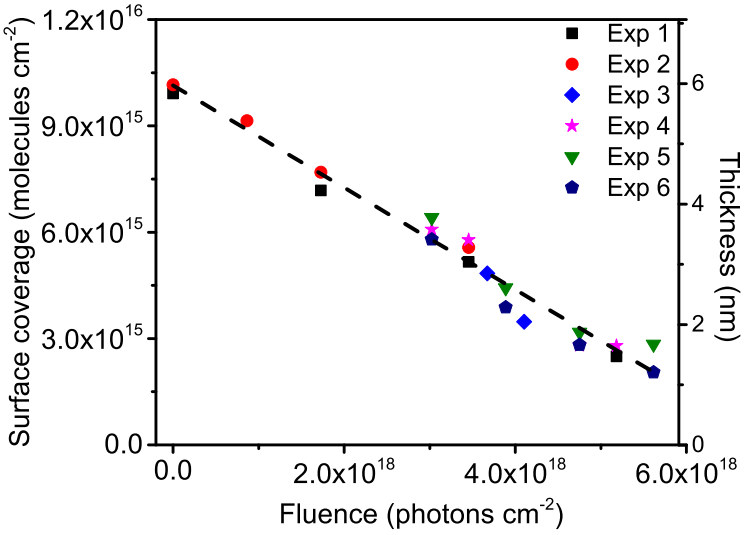

Figure 6.3: Substrate coverage of CO (left axis), thickness of the CO ice (right axis) as function of different VUV fluence. The results for five experiments, starting from different initial thicknesses are shown, and for clarity these have been horizontally shifted around the fitted line that is the resulting average of the photodesorption rates of these independent measurements. The photodepletion of CO ice at 20 K can be determined by a linear fit. Surface coverages have been determined with equations 21 and 22, with n = 1.27 and $\rho = 0.80$ g cm^{-3}.

The slope of figure 6.3 represents the CO photodepletion rate. Combining all experiments a photodepletion rate of $(1.4 \pm 0.7) \cdot 10^{-3}$ molecules photon^{-1} at 20 K is obtained. This includes other loss channels, such as photochemistry leading to the formation of CO_2. Following the mass spectra we can conclude that typically less than 2% of the initial CO is converted to CO_2 after being processed by a photon fluence of $5 \cdot 10^{18}$ photons cm^{-2}. This is a minor channel, and negligible given the large relative error (50%) in the final value.

6.4 DISCUSSION AND ASTROPHYSICAL IMPLICATIONS

A correct quantification of the photodesorption rate of species is important as it determines the balance between gas and solid phase molecular reservoirs in astronomical environments such as dense clouds. It is also needed for the interpretation of astronomical observations, such as the position of photon induced snow lines, as input for astrochemical modelling.

6.4.1 *Overview of the CO photodesorption rates*

With the use of IR spectroscopy and/or mass spectrometry the photodesorption rate for CO ice has been measured in a number of studies since 2007 yielding values from 10^{-1} to 10^{-3} molecules photon^{-1} (Öberg et al., 2007, 2009b; Muñoz Caro et al., 2010; Chen et al., 2014; Muñoz Caro et al., 2016). Wavelength dependent photodesorption studies of CO ice at 18 K using synchrotron radiation have unveiled more information about the underlying process, illustrating that it follows a DIET mechanism, and providing for a first time monochromatic photodesorption rates (Fayolle et al., 2011).

This has triggered the idea that it is important to monitor the MW discharge lamp spectral characteristics during a photodesorption experiment. Recently, photodesorption experiments have been performed with fully characterised SEDs of the VUV lamp (Chen et al., 2014), but still these could not explain the difference in reported photodesorption rates (Ligterink et al., 2015).

Several other causes for the observed deviations have been considered. Different studies have used different methods for the flux calibration, based on either actinometry or NIST calibrated photodiodes, and this may have lead to systematical offsets. It is possible that visible light from the H_2 plasma was not fully substracted, artificially increasing the VUV flux. In addition, it has been observed that the MgF windows that are commonly used as a vacuum seal between microwave discharge lamp and UHV setup, degrade with time, specifically blocking the Ly-α light. I.e., an older window may influence the SED impacting on the ice. Not only on the instrumental side issues exist, but also the interpretation of data is not straight forward, as photoexcitation by VUV photons can induce both photodesorption or photochemistry. For CO ice this effect is negligible, the photodepletion signal is very close to the photodesorption value, as discussed before. However, this does not apply to other species, as was illustrated recently for methanol ice (Bertin et al., 2016). The photodissociation of methanol yields radicals in the ice which can result in photochemistry or alternatively the fragments may photodesorb directly after their formation. Finally, also the exact ice conditions play a role; ice thickness, ice deposition temperature and ice morphology. For CO ice, Öberg et al. (2009b) observed an ice deposition temperature dependence, as recently confirmed and extended over a wider range (7 to 20 K) by others, who concluded that this can be linked to the level of CO dipole orientation within the amorphous state (Muñoz Caro et al., 2010, 2016).

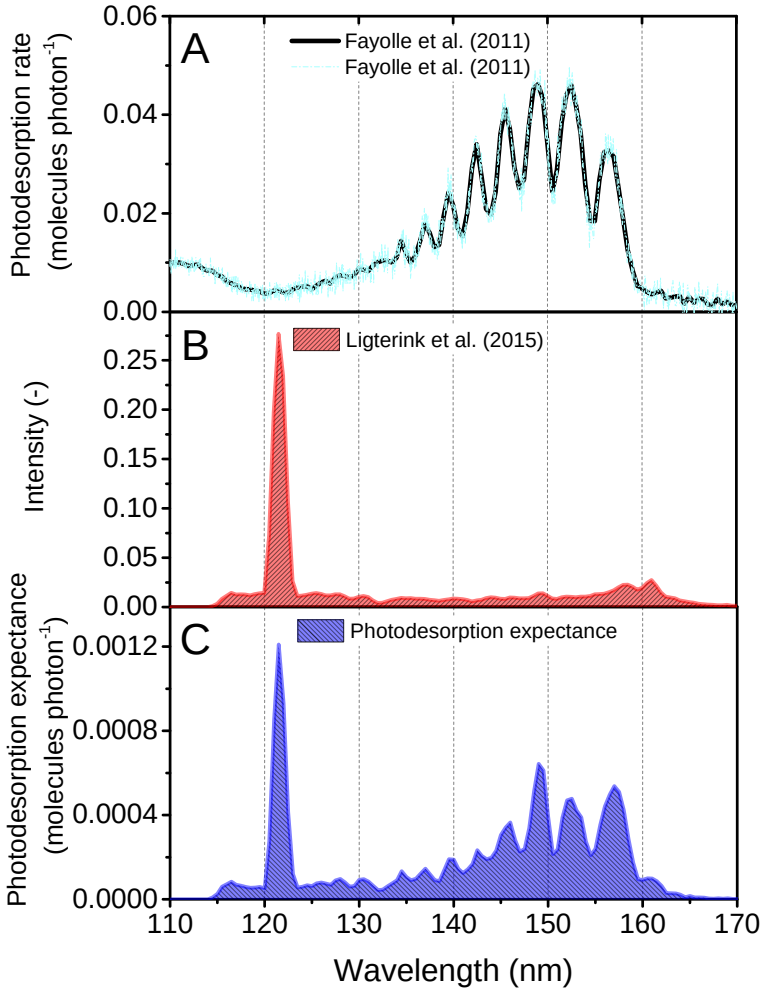

Figure 6.4: Panel A shows the wavelength dependent photodesorption of CO ice at 18 K (Fayolle et al., 2011), in panel B the normalised VUV spectrum (integrated area = 1) is depicted measured with the absolute VUV spectrometer described in Ligterink et al. (2015), and in panel C, the multiplication of panel A and B is shown, representing the photodesorption expectance based on the VUV spectrum of the H_2 lamp. Integration of the curve of panel C provides the estimate of the CO photodesorption rate at 18 K based on the spectral characteristic of applied VUV-lamp.

This all makes it hard to decide which photodesorption value is best to use in astrochemical models. This is already true in the case of the largely non-dissociative photodesorption of solid CO; for other species that dissociate upon VUV irradiation the analysis is even more complex.

Thus for these reasons it is interesting to look for possibilities to link different methods or to use alternative approaches like the one introduced here. In the first case, for example, the recently investigated spectral energy distribution of the MW H_2 lamps (Ligterink et al., 2015) can be linked with the wavelength dependent information obtained by Fayolle et al. (2011). By multiplying the CO photodesorption spectrum (Fig. 6.4A)

and the spectral energy distribution of the lamp used in present study (Fig. 6.4B), we find a wavelength dependent photodesorption expectance (Fig. 6.4C). Subsequent integration of this spectrum yields a photodesorption rate, based on the expected spectral energy distribution of the lamp. This results in a photodesorption rate of $(10 \pm 7) \cdot 10^{-3}$ molecules photon^{-1}. The error here is large, as this value is derived by combining the results from two stand-alone experiments. The application of the alternative experimental approach, as introduced in this paper, yields a photodesorption rate for CO ice at 20 K of $(1.4 \pm 0.7) \cdot 10^{-3}$ molecules photon^{-1}. This value is not too far off from earlier experiments (Öberg et al., 2007, 2009b) and it is in decent agreement with recent molecular dynamics simulations focussing on CO photodesorption, van Hemert et al. (2015) predicted a photodesorption probability of $4 \cdot 10^{-3}$ molecules photon^{-1}, but the value is about one decade off compared to rates reported earlier.

6.4.2 *Astrophysical implications*

In Fig. 6.5 all reported experimental CO photodesorption rates are summarized with the corresponding error margins. These vary between 10^{-3} and 10^{-1} molecules photon^{-1}, where one has to notice that not all experiments were performed for similar conditions. Compared to the astronomical photodesorption rates that were used in the 80's and 90's - roughly 10^{-5} to 10^{-8} molecules photon^{-1} - (Draine & Salpeter, 1979; Hartquist & Williams, 1990), the relevance of the recent laboratory values is clear; even with an existing discrepancy of roughly one decade, the laboratory values indicate that the CO photodesorption is up to six orders of magnitude more effective than assumed in the original models. From the listed experiments, the CO deposition temperature dependence is clearly visible. Relatively high photodesorption rates have been observed at low deposition temperature. Therefore, it is important to refer to experiments that are performed for an astronomically relevant temperature. Current studies show that the CO snow line shows up for temperatures between 17 and 19 K, i.e., CO photodesorption values recorded for 20 K are likely more representative than those recorded at 10 K. In astrochemical models, it is wise to consider the option of using a weighted average or working with two values, in between the existing experimental limits, so 10^{-2} and 10^{-3} molecules photon^{-1}. Furthermore, it is well possible that for 'real' interstellar ices other effects, such as impacting cosmic rays, may affect the CO ice matrix, also influencing the effective photodesorption rate. However, as experiments have shown, CO hydrogenation reactions transfer CO into H_2CO and CH_3OH (Fuchs et al., 2009; Linnartz et al., 2015) and their presence in the ice, likely, will affect the overall efficiency of a photodesorption event. The same will apply to the water photodesorption rate that will be affected by substantial amounts of CO_2 mixed into the H_2O matrix. It is clear that accurate modelling is needed to take all these effects into account. As discussed here, MATRI^{2}CES and the method described here are ideally suited to determine the photodesorption rates for these more complex ices.

6.5 CONCLUSION

This study characterises the photodesorption rate for CO ice at 20 K, using a new experimental concept. Compared to the established techniques, the method has the extra advantage that the complete ice composition and thickness of the original ice can be derived upon VUV irradiation. Hereby, both photodesorption and photochemical processes can be quantified.

We have demonstrated the feasibility of this concept on the example of CO ice at 20 K. We have observed that the CO_2 formation channel is minor to negligible. The photodesorption rate of CO ice at 20 K is determined as $(1.4 \pm 0.7) \cdot 10^{-3}$ molecules photon^{-1}.

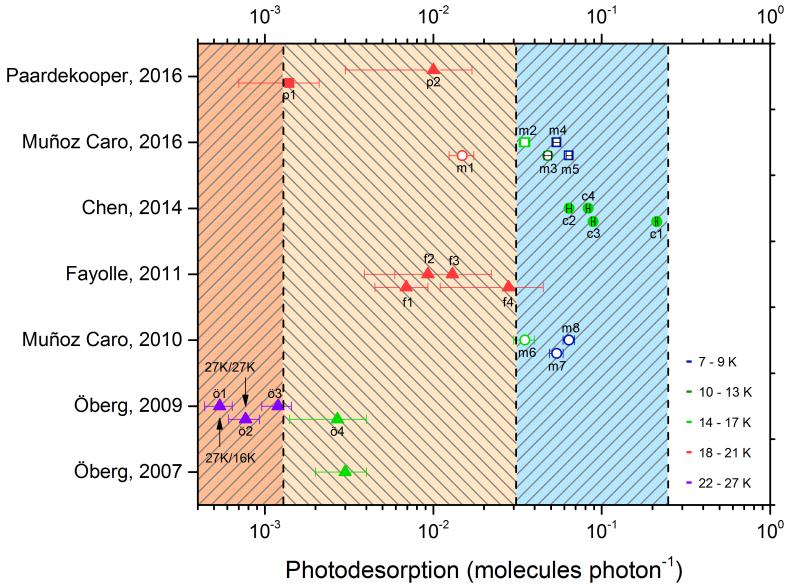

Figure 6.5: Overview of all the experimental CO photodesorption studies, the color coding refers to the deposition and photolysis temperature (with the exception of ö1, 27 K/ 16 K). Most studies have been performed with a discharge lamp, while Fayolle et al. (2011) used synchrotron irradiation as VUV source (f1=10.2 eV, f2=11.2 eV, f3=9.2 eV, f4=8.2 eV). The flux of the discharge lamps are obtained with a NIST calibrated photodiode (Öberg et al., 2007, 2009b; Chen et al., 2014) or using actinometry (Muñoz Caro et al., 2010, 2016). The labelling of Chen et al. (2014): c1, c2, c3 and c4 refers to different running conditions of the discharge lamp resulting in different SEDs, while the labelling of the present study refers to the direct measurement (p1) or the indirect measurement (p2) based on the SED of the lamp and wavelength dependence of CO photodesorption from Fayolle et al. (2011) (see Fig. 6.4).

The uncertainty in this value is rather high, as in most reported photodesorption studies, and in decent agreement with a number of previously obtained results. It is clear that for pure CO ice, photodesorption rates are in the 10^{-3} to 10^{-2} molecules photon^{-1} range and that at least part of the deviating results can be explained by different experimental settings. For astrochemical models it is particularly important to take into account the deposition temperature; several of the values reported in literature are measured for values that may be too low to be astrochemically relevant.

BIBLIOGRAPHY

Andersson, S., Al-Halabi, A., Kroes, G.-J., & van Dishoeck, E. F. 2006, J. Chem. Phys., 124, 64715
Andersson, S. & van Dishoeck, E. F. 2008, Astron. Astrophys., 491, 907
Arasa, C., Andersson, S., Cuppen, H. M., van Dishoeck, E. F., & Kroes, G.-J. 2010, J. Chem. Phys., 132, 184510
Arasa, C., Andersson, S., Cuppen, H. M., van Dishoeck, E. F., & Kroes, G. J. 2011, J. Chem. Phys., 134, 164503
Arasa, C., Koning, J., Kroes, G.-J., Walsh, C., & van Dishoeck, E. F. 2015, Astron. Astrophys., 575, A121
Bahr, D. A. & Baragiola, R. A. 2012, Astrophys. J., 761, 36
Baratta, G. A. & Palumbo, M. E. 1998, J. Opt. Soc. Am., 15, 3076
Bertin, M., Fayolle, E. C., Romanzin, C., et al. 2012, Phys. Chem. Chem. Phys., 14, 9929
Bertin, M., Fayolle, E. C., Romanzin, C., et al. 2013, Astrophys. J., 779, 120
Bertin, M., Romanzin, C., Doronin, M., et al. 2016, Astrophys. J. Lett., 817, L12
Bossa, J.-B., Paardekooper, D. M., Isokoski, K., & Linnartz, H. 2015, Phys. Chem. Chem. Phys., 17, 17346
Caselli, P., Keto, E., Bergin, E. A., et al. 2012, Astrophys. J. Lett., 759, L37
Chang, Q. & Herbst, E. 2016, Astrophys. J., 819, 145
Chen, Y.-J., Chuang, K.-J., Muñoz Caro, G. M., et al. 2014, Astrophys. J., 781, 15
Chen, Y.-J., Nuevo, M., Chu, C.-C., et al. 2011, Adv. Space Res., 47, 1633
Cuppen, H. M., Ioppolo, S., Romanzin, C., & Linnartz, H. 2010, Phys. Chem. Chem. Phys., 12, 12077
DeSimone, A. J., Crowell, V. D., Sherrill, C. D., & Orlando, T. M. 2013, J. Chem. Phys., 139, 164702
Draine, B. T. & Salpeter, E. E. 1979, Astrophys. J., 231, 438
Drozdovskaya, M. N., Walsh, C., Visser, R., Harsono, D., & van Dishoeck, E. F. 2014, Mon. Not. R. Astron. Soc., 445, 913
Dulieu, F., Congiu, E., Noble, J., et al. 2013, Sci. Rep., 3, 1338
Dzegilenko, F., Herbst, E., & Uzer, T. 1995, J. Chem. Phys., 102, 2593
Es-sebbar, E.-t., Bénilan, Y., Fray, N., et al. 2015, Astrophys. J. Suppl. Ser., 218, 19
Fayolle, E. C., Bertin, M., Romanzin, C., et al. 2011, Astrophys. J. Lett., 739, L36
Fayolle, E. C., Bertin, M., Romanzin, C., et al. 2013, Astron. Astrophys., 556, A122
Fillion, J.-H., Fayolle, E. C., Michaut, X., et al. 2014, Farad. Discuss., 168, 533
Fuchs, G. W., Cuppen, H. M., Ioppolo, S., et al. 2009, Astron. Astrophys., 505, 629
Galloway, E. T. & Herbst, E. 1994, Astron. Astrophys., 287, 633
Gredel, R., Lepp, S., Dalgarno, A., & Herbst, E. 1989, Astrophys. J., 347, 289
Hama, T., Yokoyama, M., Yabushita, A., et al. 2010, J. Chem. Phys., 132, 164508
Hartquist, T. W. & Williams, D. A. 1990, Mon. Not. R. Astron. Soc., 247, 343
Hollenbach, D., Kaufman, M. J., Bergin, E. A., & Melnick, G. J. 2009, Astrophys. J., 690, 1497
Ioppolo, S., Öberg, K., & Linnartz, H. 2014, Laboratory Astrophysics, ed. S. Schlemer, H. Mutschke, T. Giesen, & C. Jäger, pages 289 to 319 (Wiley-VCH Verlag GmbH & Co. KGaA)
Leger, A., Jura, M., & Omont, A. 1985, Astron. Astrophys., 144, 147
Ligterink, N., Paardekooper, D.M., Chuang, K.-J., et al. 2015, Astron. Astrophys., 584, A56
Linnartz, H., Ioppolo, S., & Fedoseev, G. 2015, Int. Rev. Phys. Chem., 34, 205
Martín-Doménech, R., Manzano-Santamaría, J., Muñoz Caro, G. M., et al. 2015, Astron. Astrophys., 584, A14
Muñoz Caro, G. M., Chen, Y.-J., Aparicio, S., et al. 2016, Astron. Astrophys., 589, A19
Muñoz Caro, G. M., Jiménez-Escobar, A., Martín-Gago, J. Á., et al. 2010, Astron. Astrophys., 522, A108
Öberg, K. I. 2016, Chem. Rev., DOI: http://dx.doi.org/10.1021/acs.chemrev.5b00694
Öberg, K. I., Fuchs, G. W., Awad, Z., et al. 2007, Astrophys. J. Lett., 662, L23
Öberg, K. I., Furuya, K., Loomis, R., et al. 2015, Astrophys. J., 810, 112
Öberg, K. I., Linnartz, H., Visser, R., & van Dishoeck, E. F. 2009a, Astrophys. J., 693, 1209
Öberg, K. I., van Dishoeck, E. F., & Linnartz, H. 2009b, Astron. Astrophys., 496, 281
Paardekooper, D. M., Bossa, J.-B., Isokoski, K., & Linnartz, H. 2014, Rev. Sci. Instrum., 85,
Paardekooper, D. M., Bossa, J.-B., & Linnartz, H. 2016, Astron. Astrophys., DOI: http://dx.doi.org/10.1051/0004-6361/201527937
Piétu, V., Dutrey, A., & Guilloteau, S. 2007, Astron. Astrophys., 467, 163
Prasad, S. S. & Tarafdar, S. P. 1983, Astrophys. J., 267, 603

Roux, J. A., Wood, B. E., Smith, A. M., & Plyer, R. R. 1980, Arnold Engineering Development Center Int. Rep. AEDC-TR-79,AAEDC, Arnold Air Force Base
Shen, C. J., Greenberg, J. M., Schutte, W. A., & van Dishoeck, E. F. 2004, Astron. Astrophys., 415, 203
van Hemert, M. C., Takahashi, J., & van Dishoeck, E. F. 2015, J. Phys. Chem. A, 119, 6354
Vastel, C., Ceccarelli, C., Lefloch, B., & Bachiller, R. 2014, Astrophys. J. Lett., 795, L2
Walsh, C., Nomura, H., & van Dishoeck, E. 2015, Astron. Astrophys., 582, A88
Watanabe, N. & Kouchi, A. 2002, Astrophys. J. Lett., 571, L173
Westley, M. S., Baragiola, R. A., Johnson, R. E., & Baratta, G. A. 1995a, Nature, 373, 405
Westley, M. S., Baragiola, R. A., Johnson, R. E., & Baratta, G. A. 1995b, Planet. Space Sci., 43, 1311
Willacy, K. & Langer, W. D. 2000, Astrophys. J., 544, 903
Yuan, C. & Yates, J. T. 2013, J. Chem. Phys., 138, 154302
Zhen, J. & Linnartz, H. 2014, Mon. Not. R. Astron. Soc., 437, 3190

7

QUADRUPOLE ION TRAP/TIME-OF-FLIGHT PHOTO-FRAGMENTATION SPECTROMETRY OF THE HEXA-PERI-HEXABENZOCORONENE (HBC) CATION

We have studied the photo-fragmentation of the hexa-peri-hexabenzocoronene (HBC) cation -$C_{42}H_{18}^{+}$- a large PAH cation of potential astrophysical interest. HBC cation photo-fragment patterns are measured upon irradiation by an unfocused Nd:YAG laser (532 nm) for different experimental conditions, using quadrupole ion trap, time-of-flight mass spectrometry. Both stepwise dehydrogenation of $C_{42}H_{18}^{+}$ and C_2/C_2H_2 loss pathways are identified as relevant photodissociation routes.

J. Zhen, D.M. Paardekooper, A. Candian, H. Linnartz and A.G.G.M. Tielens, *Quadrupole ion trap/time-of-flight photo-fragmentation spectrometry of the hexa-peri-hexabenzocoronene (HBC) cation*, Chem. Phys. Lett., 592, (2014) 211

7.1 INTRODUCTION

Polycyclic aromatic hydrocarbons, PAHs, both neutral and charged, are likely the molecular species responsible for the mid-IR emission features (strongest at 3.3, 6.2, 7.7, 8.6, and 11.2 μm) detected from a variety of astrophysical objects. These emissions are expected to occur following internal energy redistribution after UV excitation by photons arising from the interstellar radiation field (Allamandola et al., 1985; Leger & Puget, 1984; Sellgren, 1984; Tielens, 2008; Bregman & Temi, 2001; D'Hendecourt et al., 1986). PAHs in the interstellar medium (ISM) are expected to be large, with 30 up to 100 carbon atoms species responsible for most of the mid-IR emission, and carrying as much as 10-15% of the elemental carbon (Tielens, 2008). The observed spectra imply that a considerable fraction of interstellar PAHs are ionized (Le Page et al., 2003; Allamandola et al., 1999), consistent with the fact that their ionization potential is generally well below the energy of the available photons, and this photoionization plays a key role in the energy balance of gas in the ISM (Bakes & Tielens, 1994; Tielens, 2005).

Photo-fragmentation is one of the main destruction pathways for PAHs in space (Tielens, 2008). In order to understand PAH-cation dissociation dynamics, dedicated laboratory studies are needed that characterize fragmentation patterns upon photo-excitation, and their dependence on, e.g., wavelength and photon intensity. A number of experiments have studied the photo-chemistry of (small) PAHs (see for example Lifshitz, 1997; Dunbar, 2000). Experimental studies of species relevant to astronomy have generally used a time-of-flight, photoionization mass spectrometry (PIMS) technique, focusing on the appearance (internal) energy at which the dissociation rate is approximately 10^4 s^{-1} (e.g., an experimental timescale of 10^4 s Jochims et al., 1994, 1999). In these studies, loss channel(s) mainly involve (sequential) hydrogen loss but C_2H_2 (and C_2H_3) loss is also observed at higher internal energies. In the ISM, however, different molecular dynamical timescales are at play. Fragmentation has to compete with relaxation through IR emission that occurs on time scales of the order of $\sim 0.01 - 1$ s, depending on the size of the species (Tielens, 2005; Dunbar & Lifshitz, 1991). In addition, since PAHs typically absorb $\sim 10^8$ UV photons over their lifetime - some 100 Myr - even dissociation channels with a low probability are relevant (Tielens, 2005). Moreover, astrochemically related studies focus on the smaller PAHs (Naphthalene to Coronene with 10-24 C-atoms) (Tielens, 2008; Jochims et al., 1994; Ekern et al., 1998) that may be less abundant in space.

We have studied the long time-scale, i.e., multi-second photo-stability of the large PAH cation hexa-peri-hexabenzocoronene (HBC) cation. HBC ($C_{42}H_{18}$) is a large all-benzenoid PAH which has been suggested to be present in space (Rouillé et al., 2009; Kokkin et al., 2008; Hendel et al., 1986) and that is taken here as a prototypical example for large(r) PAHs.

7.2 EXPERIMENT

The experiments are performed on the 'instrument for Photodynamics of PAHs' (i-PoP; Fig. 7.1), consisting of two differentially pumped chambers. The source chamber (QIT chamber) comprises a commercially available quadrupole ion trap (Jordan C-1251) that is connected via a 2 mm skimmer to the detection chamber (TOF chamber) with a time-of flight mass spectrometer (Jordan D-850). The base pressure of the two chambers is $\sim 5.0 \cdot 10^{-8}$ mbar (QIT) and $\sim 2.0 \cdot 10^{-8}$ mbar (TOF). HBC is evaporated in the source chamber by heating the powder (Kentax) with purity better than 99.5% in an oven (Heat Wave Labs) at a temperature of 570 K. Subsequently, evaporated molecules are ionized by an electron gun (EGUN, Jordan C-950) and transported into the ion trap via an ion gate. The method follows standard (gating) procedures, using plates on different potentials and

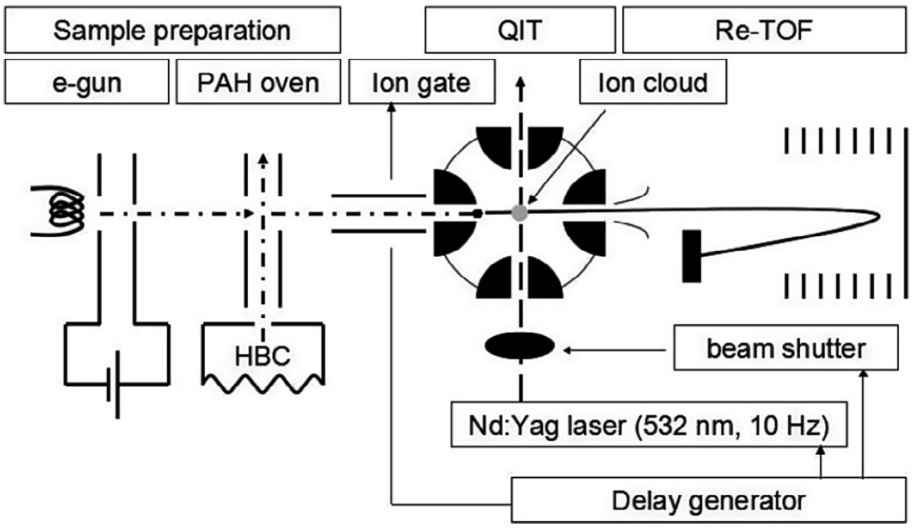

Figure 7.1: A schematic of the i-PoP setup.

a split Einzel lens. A DC voltage pulser (Jordan D-1040) controls the opening and closing of the gate and typical ramp times in the trap amount to 10 ns rise time.

Prior to ion injection, He buffer gas is introduced into the trap via a leak valve. The buffer gas pressure inside the trap is higher than the background pressure of the QIT chamber because of the conductance-limited pumping efficiency of gas out of the trap. The conductance through all the apertures of the QIT is determined as 8.34 L/s from other reported trap conductance measurements (Sassin et al., 2008). The conductance of the turbo pump for the QIT chamber is 230 L/s, so we estimate that the buffer gas pressure in the ion trap is $\sim 7 \cdot 10^6$ mbar, with an estimated absolute uncertainty of 50%. As a result of thermalization, the PAH ions will concentrate in the center of the trap (Sassin et al., 2008; Gulyuz et al., 2011). The ion cloud is expected to remain at a constant diameter (about 0.5 mm) in the center of the trap throughout the irradiation period. The working pressures in QIT and TOF chamber are $\sim 3.0 \cdot 10^{-7}$ and $\sim 3.0 \cdot 10^{-8}$ mbar, respectively, corresponding to a mean free path of ~ 300 and ~ 3000 m, and to ~ 1 and ~ 10 s between collisions.

The second harmonic of a Nd:YAG laser (DCR-3, Spectra-Physics) - 532 nm, ~ 6 ns - operated at 10 Hz is used to irradiate the trapped ions. The spatial profile of the laser beam is nearly gaussian with low intensity modulation and harmonic conversion efficiencies are high while retaining good spatial mode. The beam diameter is 7 mm; the beam divergence is 0.5 mrad, and the laser beam has a high on-axis energy density at long distance from the laser. Optical access to the QIT is realized through a 2.4 mm aperture in the ring electrode. In our experiment, the laser beam is guided horizontally through the ion trap. In addition, the intensity of the fragments of HBC cations is used in helping to align the laser beam. The laser pulse energy is measured by a power meter (Vector, H310) before the beam enters the vacuum chamber and is typically up to 18 mJ/pulse with an average power values that range up to $3.0 \cdot 10^6$ W. i-PoP operates at a typical frequency of 0.2 Hz, i.e., one full measuring cycle lasts 5 s. It is possible to accumulate photo-fragmentation products of multiple laser shots, thereby increasing the fragmentation yield. Experiments are usually performed during a 1.8 s slot using 18 laser shots. A beam shutter acts as a physical shield and determines the interaction time of the light with the trapped ions. The electromechanical shutter (Thorlabs SC05) is externally triggered to guarantee that the

ion cloud is irradiated only for a specified amount of time during each scan cycle. The QIT rf power supply (Jordan D-1203) maintained at 3250 V_{p-p} is capable of switches off the rf amplitude within two cycles. Following a ring-down of this voltage, the fragments remain in the QIT until extraction into the TOF drift tube. During ion extraction from the trap, pulsed voltages from ground to +800 V and from ground to −800V (5 ns rise time, 10 μs width) are put onto the two end caps (Jordan D-1050) to empty the trap and transfer the ion cloud into the TOF mass spectrometer for mass analysis. The ion cloud passes a 2 mm skimmer and is then uniformly accelerated into the field-free region by a mesh at the entrance of the TOF chamber. The TOF ion signal is detected by a multichannel plate (Jordan, C-701). The estimated total signal gain through the acquisition electronics is 2×10^8. The TOF mass spectrometer allows for simultaneous detection of the parent ion and the fragment ion signals.

A high precision delay generator (SRS DG535) controls the full timing sequence. Each scan cycle begins with an empty ion trap. At the leading edge of the master trigger the ion gate opens, allow- ing the ion trap to fill for a certain amount of time (typically ~ 3 s) with PAH ions. After a short time delay (typically ~ 0.2 s), the ion cloud thermalizes to room temperature (~ 298 K) by collisions with the He buffer gas, and as a direct consequence the diameter of the cloud shrinks (Sassin et al., 2008; Gulyuz et al., 2011). The laser beam shutter opens and the ion cloud is irradiated. During each cycle, the laser irradiation time is changed to one of the preprogrammed time periods. At the end of the irradiation, a negative square pulse is applied to the end cap, accelerating the ions out of the trap and into the field-free TOF region the resulting mass fragments are measured. The full data-acquisition is controlled by LabVIEW routines.

In all experiments, uncertainties include the total number of ions in the trap which we estimated from the repeated blank shots, (~ 4%), the laser pulse energy (estimated at ~ 2-5% at different laser pulse energies), and the local baseline determination that results in relative abundance uncertainties of up to ~ 2%. Thus, the formation yield of products has a total estimated uncertainty of ~ 6%.

7.3 RESULTS AND DISCUSSION

The application of i-PoP to astrophysically relevant large PAHs is illustrated by the trapping efficiency and photo-dynamics of hexa-peri-hexabenzocoronene (HBC) cations (the m/z of $^{12}C_{42}H_{18}^+$ = 522.141) following unfocused 532 nm laser irradiation. In Figure 7.2A a typical TOF mass spectrum is shown for a 3.0 s long filling of the trap with HBC cations. The isotopologues and HBC fragments are labeled in the inset mass spectra that are illustrative for the level of accuracy that can be achieved. In order to obtain this signal-to-noise ratio, mass-spectra are averaged 150 times. The mass resolution of the spectrometer is determined at around 1500. The measured mass spectra in the range m/z, 522-526, corresponding to isotopologues $^{12}C_{42}H_{18}^+$ (62.67%), $^{12}C_{41}{}^{13}CH_{18}^+$ (29.45%), $^{12}C_{40}{}^{13}C_2H_{18}^+$ (6.75%) and $^{12}C_{39}{}^{13}C_3H_{18}^+$ (1.01%), scale well with their natural abundances. Due to the electron impact ionization, partially H-stripped HBC ions (e.g., $C_{42}H_{16}^+$) are present as well. Peaks at about m/z = 519.2 and 521.3 could in principle also be due to $^{12}C_{42}H_{15}^+$ and $^{12}C_{42}H_{17}^+$. However, as the mass signal ratios are in good agreement with the expected isotopologue values for $^{12}C_{41}{}^{13}CH_{14}^+$ and $^{12}C_{41}{}^{13}CH_{16}^+$, a pure ^{12}C-based solution is less likely. Hence, in agreement with the laser irradiation experiments to be described below, electron impact ionization leads preferentially to fragmentation losses of 2H (or H_2). Also visible in Figure 7.2A (around m/z = 261) is the doubly-ionized HBC cation $(C_{42}H_{18})^{2+}$. Figure 7.2A confirms that trapping time and trapping efficiency of i-PoP are very good.

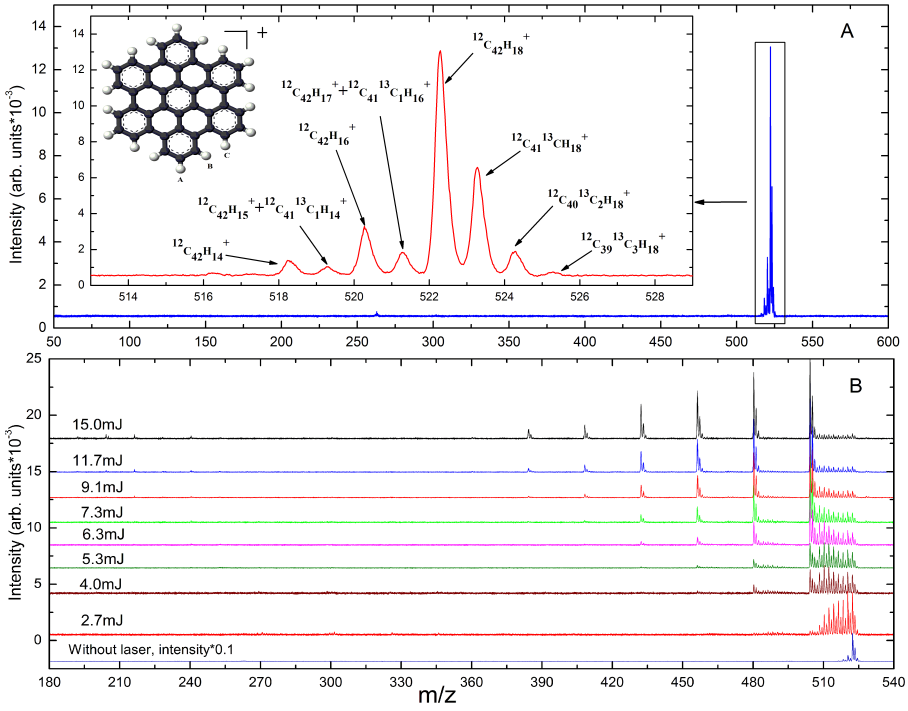

Figure 7.2: Upper panel (A): time-of-flight mass spectrum of the HBC radical cations trapped after evaporation and electron impact ionization. The inset is a zoom-in around m/ z = 522 revealing the presence of isotopic distribution and dehydrogenated of HBC cations, specifically including ^{13}C-containing species. Lower panel (B): time-of-flight mass spectrum of HBC radical cations irradiated with 532 nm at different laser pulse energies. Note that these mass spectra have been taken after 18 laser pulses and therefore include the effects of irradiation of HBC as well as HBC daughter products during the full measurement cycle.

Figure 7.2B shows the resulting mass spectrum of trapped HBC cations upon 532 nm irradiation at different laser pulse energies where a laser energy of 2.7 mJ corresponds to an average power of 4.5×10^5 W in the beam. All experiments have the same ion filling time of 3 s and trapped HBC cations are irradiated for similar periods (1.8 s). A wide range of fragment ions are evident in these mass spectra that are attributed to multiple, successive absorption/ fragmentation events during the 1.8 s period, as will be discussed in detail below. Figure 7.2B shows that the terminal photo-fragment pattern clearly depends directly on the incident radiation flux. The general trend that can be observed is that HBC cations dehydrogenate and with increasing laser pulse energy multiple fragmentation steps become more prominent. In addition, other fragmentation channels become accessible at higher laser pulse energy. For laser pulse energies in the range 2.0-5.0 mJ the photodissociation of HBC mainly follows sequential 2H (or H_2) separations, leading to the predominance of even-mass species $^{12}CH_{2n}{}^+$ with n = [0-9]. Masses corresponding to $C_{30+2\times m}H_{2n}{}^+$ with m = [0-5] and n = [0-8] appear as well, following a C_2/C_2H_2-loss channel that has been identified previously as a major fragmentation channel in the dissociation of PAH cations (Lifshitz, 1997; Jochims et al., 1994). At very high laser pulse energy, the HBC cation can undergo many, many sequential absorption/fragmentation events and it may even lose all of its hydrogen atoms (sequentially) to leave a bare carbon cluster containing

42 carbon atoms. Similar complete dehydrogenation behavior upon laser irradiation has been observed for the small, 24 C-atom coronene and naphtho[2,3-a]pyrene cations (Joblin, 2003; Ekern et al., 1997). Subsequently, C_{42}^+ can fragment to smaller pure carbon clusters. This will be discussed later.

More details on the laser pulse energy dependent dissociation behavior are illustrated in Figure 7.3, in panel A for a lower value and in panel B for a higher value of the laser pulse energy. In panel A, $C_{40}H_{2n}^+$ fragments with $n = [0\text{-}8]$ are shown. We corrected the odd H-peak for the ^{13}C isotope, taking natural abundances and assuming that the fragmentation pattern is not C-isotope dependent. The dissociation pattern of HBC cation follows the reaction pathways:

$C_{42}H_{18}^+ \xrightarrow{-nH_2/n(2H)} C_{42}H_{18-2n}^+ \xrightarrow{-mC_2} C_{42-2m}H_{18-2n}^+$ or:

$C_{42}H_{18}^+ \xrightarrow{-nC_2H_2} C_{42-2n}H_{18-2n}^+$. The fragment $C_{40}H_4^+$, for example, acts as an intermediate in the dissociation network, as shown in Figure 7.3A: the production reaction pathways of:

$C_{40}H_4^+$ are $C_{42}H_6^+ \xrightarrow{-H_2/2H} C_{42}H_4^+ \xrightarrow{-C_2} C_{40}H_4^+$ or:

$C_{42}H_6^+ \xrightarrow{-C_2H_2} C_{40}H_4^+$ and the dissociation pathways of $C_{40}H_4^+$ are:

$C_{40}H_4^+ \xrightarrow{-H_2/2H} C_{40}H_2^+ \xrightarrow{-C_2} C_{38}H_2^+$ or $C_{40}H_4^+ \xrightarrow{-C_2H_2} C_{38}H_2^+$.

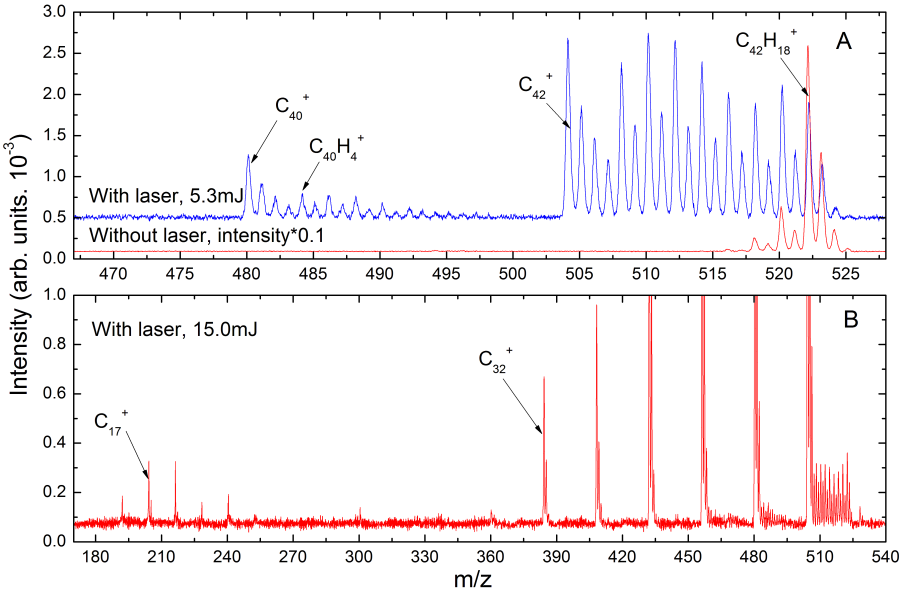

Figure 7.3: Time-of-flight mass spectrum of HBC radical cations: the upper panel (A) is without laser and with 5.3 mJ laser pulse energy; the lower panel (B) is with 15.0 mJ laser pulse energy.

In the 15.0 mJ set of measurements as shown in Figure 7.3B, all ions are almost completely dehydrogenated, resulting in mass spectra dominated by species with masses in the range of C_{30}-C_{42}, and leaving only traces of hydrogenated species, e.g., $C_{42}H_2{}^{n+}$. The bare carbon clusters that are found mainly originate from C_{42}^+ losing C_2 fragments. This loss pattern has been observed also for fullerenes (Berné & Tielens, 2012; Lifshitz, 2000). However, as we also observe low concentrations of intermediates that have lost one or more C_2H_2 groups, as outline above, acetylene-loss with subsequent dehydrogenation

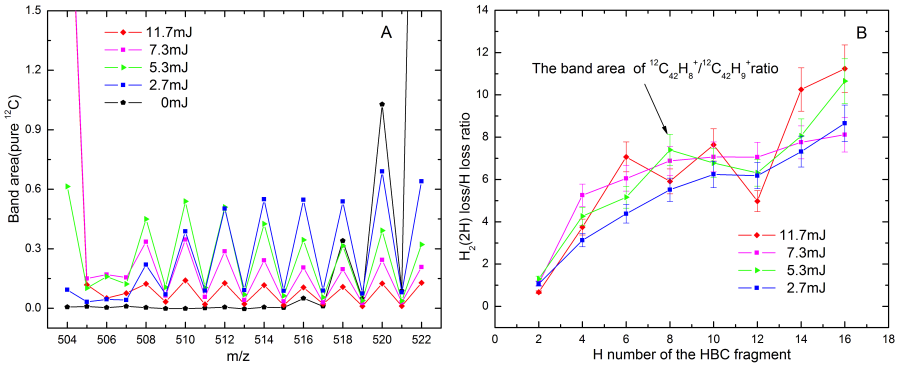

Figure 7.4: The left panel (A) is the calculated value of the integrated signals for the $^{12}C_{42}H_n^+$ (with n = [0-18]) mass peaks, for different laser pulse energies and corrected for the isotope contamination; the right panel (B) shows the ratio of the calculated value of the integrated signals for $^{12}C_{42}H_{2n}^+/^{12}C_{42}H2n+1^+$ with n = [1-8].

may provide an alternative but obviously less important channel for C_{30}-C_{42} formation. Figure 7.3B also shows low mass fragments in the range m/z = 180-250. These peaks may represent the doubly ionized, bare $C_{2n}{}^{2+}$ clusters with n = 16-20. As doubly charged HBC has a very low initial abundance in these experiments (Figure 7.3A), any doubly charged cation clusters would involve an additional ionization step. However, thermoionic emission is only observed for systems where the dissociation energy is larger than the ionization potential (Campbell & Levine, 2000), and with ionization potentials in the range of 10-12 eV and cohesive energies of 6-7 eV for (Seifert et al., 1996; Jones, 1999), depending on cluster size, we consider doubly charged pure carbon clusters highly unlikely candidates for these mass peaks. Rather, as in photo-fragmentation experiments for fullerenes, we recognize the presence of two separate populations of carbon clusters: The first group of pure carbon clusters, $C_n{}^+$, $n \geqslant 32$, is separated by 2 C-atoms. The second population, $C_n{}^+$, $n \leqslant 20$, differs by 1 C-atom. In analogy with the fullerenes, it is possible that the first group is carbon cages while the second group may correspond to rings (Lifshitz, 2000). Follow up studies will have to address the relative importance of fragmentation and isomerization for highly excited, large PAH species.

Given the relatively high abundances of several ^{13}C containing HBC isotopologues, the mass spectra should be interpreted with care. Integration and calculations are necessary to obtain the abundances of the pure ^{12}C containing species. Starting from the pure $^{12}C_{42}{}^+$peak, at m/z = 504, higher lying peaks can be corrected for the isotope contaminant using natural abundance values. So, the m/z = 505 peak is corrected for the $^{12}C_{41}{}^{13}C^+$ to derive the abundance of $^{12}C_{42}H^+$. Likewise, mass peak m/z = 506 is corrected for the $^{12}C_{40}{}^{13}C_2{}^+$ and $^{12}C_{41}{}^{13}CH^+$ to derive the abundance of $^{12}C_{42}H_2{}^+$, etc. Figure 7.4A shows the measured values of the integrated signals for $^{12}C_{42}H_n{}^+$ mass peaks with n = [0-18], for different laser pulse energy and for pure ^{12}C. This analysis reveals that the even-H/odd-H abundance ratio is very large, and we conclude that mainly cations are produced that have been stripped by one or more H_2/(2H)-units. The ratio of $^{12}C_{42}H_{2n}{}^+/^{12}C_{42}H_{2n+1}{}^+$ with n = [1-8] (Figure 7.4B) does not change with laser pulse energy, and this also points towards a common underlying mechanism. The ratio decreases with the number of H left on the HBC fragment. Hence, it seems likely that the internal energy threshold for the loss channel and H_2/(2H) loss channel becomes more comparable when the number of H left on the HBC fragment decreases. This behavior of the band

ratios may reflect the importance of H_2 loss or may imply - given the alternating intensity ratio shown in Figure 7.4 - that loss of the second, sequential H has a substantially lower barrier compared to the loss of the first H.

We have performed complementary DFT calculations (B3LYP/6-31G**), quantitatively characterizing potential fragmentation channels of the HBC cation for different H positions as labeled in the inset of Figure 7.2A. These results will be described in detail in a separate study (Candian, 2014), but the main findings are mentioned here in support of the interpretation of our measurements. These show an activation energy barrier of 5.89 eV for H_2 loss in a bay region (H_{loc-B} and H_{loc-C} neighbours in Figure 7.2A) as compared to 4.72 eV for the first H loss (H_{loc-B} (in bay H) in Figure 7.2A) and 3.90 eV for the second H loss (H_{loc-A} (off bay H, but a direct neigbour of H_{loc-B}) in Figure 7.2A) that corresponds to the most energetic favorable sequence. The alternative 2H channel loss sequence yields 4.85 eV for the first H loss (H_{loc-A} in Figure 7.2A) and 3.77 eV for the second H loss (H_{loc-B} (in bay H) in Figure 7.2A). Because of the high symmetry of HBC these processes can take place at different sites. In agreement with earlier DFT calculations for small PAHs, H-loss is governed almost entirely by steric factors and the hydrogens from congested regions of the PAHs are removed preferentially (Cioslowski et al., 1996). An experimental study of H-loss for the pyrene cation, ($C_{16}H_{10}^+$) (Ling et al., 1995) identified separate channels H_2 and sequential loss of 2H. At low internal energies, H_2 loss dominated despite the higher (derived) Arrhenius energy due to the larger pre-exponential factor reflecting a favorable change in entropy. At high internal energies, loss of 2H dominated. We intend to address the relative importance of these two channels in a future Letter using tunable vacuum UV light as available from synchrotron facilities. For this reason i-PoP has been constructed as a fully mobile system.

In our experiments, HBC becomes highly excited through absorption of multiple photons and Internal Conversion (IC) leaves the molecule highly vibrationally excited in the ground electronic state, typically on a timescale of the order of 50 fs (Tielens, 2005, 2008). Intramolecular vibrational redistribution (IVR) then quickly equilibrates the excess energy among all available vibrational modes, leaving the cation amenable to renewed excitation through the same electronic system and relaxation sequence. Figure 7.5 shows the calculated value of the integrated signals for the $^{12}C_{42}H_{18}^+$ radical cations as function of the laser energy in the experiments, the errors of the band area and the laser pulse energy are shown in this figure. During a single pulse multiple photons may be absorbed. For an internal energy of 7.5 eV, corresponding to a microcanonical temperature of ≈ 1000 K, the cooling between pulses (0.1 s) is approximately 2.3 eV (*e.g.*, the equivalent of one absorbed photon) (Tielens, 2008; Boissel et al., 1997; Klots, 1989). As the internal energy required for fragmentation for HBC is well in excess of this (see below), we will - for simplicity - assume that radiative cooling is unimportant and that HBC cations that have absorbed at least a critical number of photons, n_{crit}, will fragment. The fraction of HBC cations surviving is then given by Poisson statistics and is controlled by the average number of photons absorbed. Adopting the theoretical absorption cross section at 532 nm (3×10^{-17} cm^2/molecule) for the HBC cation independent of internal excitation (Malloci, G. et al., 2007), the average number of photons absorbed in a single pulse is equal to (0.30 ± 0.02) photons at a laser pulse energy of 5.0 mJ or 5.4 photons over the experiment. Following Van-Oanh et al. (2006), this critical number of photons can then be estimated from the experiments by comparing the measured decay curve as a function of laser pulse energy to this simple theoretical model, resulting in $n_{crit} = 4$. The deviation between experiments and the theoretical fit at higher laser pulse energy may reflect the neglect of radiative cooling effects or that the absorption cross section decreases with increasing internal excitation (Van-Oanh et al., 2006). As an HBC cation starts with ≈ 0.4 eV of internal energy at 300

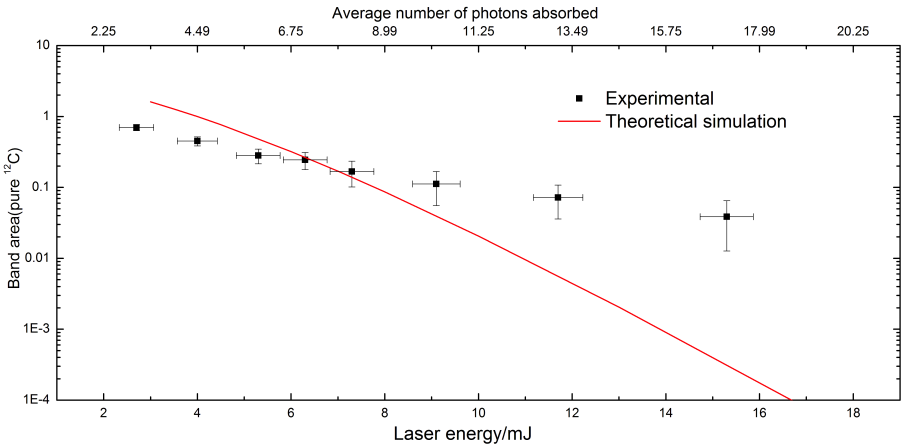

Figure 7.5: The calculated value of the integrated signals for the $^{12}C_{42}H_{18}^{+}$ radical cations as function of the laser energy in the experiments.

K (Tielens, 2005), 4 photons corresponds to an internal energy of E = 9.5 eV. Following (Tielens, 2008; Klots, 1989) we write the dissociation rate in Arrhenius form as,

$$k = k_0 e^{-E_0/k_B \cdot T_e} \tag{25}$$

where the effective temperature, T_e, is corrected for the finite heat bath and, to a good approximation, can be written for PAHs as (Tielens, 2008),

$$T_e = 2000\left(\frac{E(eV)}{N_C}\right)^{0.4}(1 - 0.2(E_0(eV)/E(eV))) \tag{26}$$

Assuming that fragmentation in the experiments implies $k \approx 10 s^{-1}$ - corresponding to the pulse frequency of 10 Hz - and adopting a pre-exponential factor typical for H-loss from PAHs of 3×10^{16} s^{-1} (Jochims et al., 1994; Le Page et al., 2001), we arrive at an Arrhenius energy of 3.2 eV, which is then strictly speaking an upper limit. However, a factor 10 higher rate corresponds to an uncertainty of only 0.2 eV in the Arrhenius energy. The derived Arrhenius energy is in good agreement with the results (3.3 eV) (Tielens, 2005) derived from an analysis of experiments on H-loss from small PAHs (Jochims et al., 1994). This is much less than the dissociation energy calculated with DFT (4.72 eV) (Candian, 2014). Indeed, we note that a barrier of 4.72 eV, would require an internal energy of ≈ 25 eV for fragmentation on a timescale of 0.1 s, equivalent to $n_{crit} > 10$, and this is clearly excluded by our experiments. This difference is a well-known characteristic when comparing experiments and statistical unimolecular dissociation theories and points towards limitations of unimolecular theory (Tielens, 2008).

7.4 ASTROPHYSICAL RELEVANCE

These results and analysis demonstrate that PAH cations offer a molecular reservoir that, upon irradiation, yields a large number of smaller but still complex species. In the ISM, PAHs may form from 'sooting' stars (Frenklach & Feigelson, 1989; Cherchneff, I., 2011) and whereas many species discovered in space have been explained as the outcome of reactions involving smaller species, the present Letter is indicative of the importance of a

top-down scenario in which molecular transients are due to fragmentation of larger species, specifically PAHs (Tielens, 2008; Berné & Tielens, 2012). The 'H-atom driven striptease of PAHs' may result in a variety of carbon structures, including carbon sheets, cages, fullerenes, as well as carbon rings and chains (Berné & Tielens, 2012; Lifshitz, 2000; Rolland et al., 2003). Given the high radiation fields in the diffuse interstellar medium, it may be interesting to include such species in the discussion of potential carriers of the Diffuse Interstellar Bands (Tielens, 2013; Steglich et al., 2011), a family of absorption features generally attributed to large interstellar molecules but whose specific identification has eluded generations of astronomers and spectroscopists (Cami & Cox, 2014).

In the ISM, the absorption time-scale is very long and only single photon excitation is generally relevant. The photon energies are limited to 13.6 eV, but higher energy photons are available in regions (e. g., in hot gas, or near O stars). Very close to the star, multiple photons events may also become important. Furthermore, we recognize that even if the probability for fragmentation in any single event is small, some hundred million absorption events may occur over the lifetime of a PAH molecule in space (Tielens, 2008). Hence, in order to translate the experimental results to conditions relevant to space, the kinetic parameters and the branching ratios involved in the fragmentation steps have to be determined. The present experimental setup, connected to a synchrotron source is well suited to such a systematic study as the energy of the exciting photon can be tuned to 'force' fragmentation of large PAHs (>24 C-atoms) in the 100 µs-100 ms range accessible with our apparatus. Time-resolved fragmentation kinetics would then allow transition state characteristics to be determined (Lifshitz, 1997; Ling et al., 1995; Gotkis et al., 1993).

7.5 CONCLUSION

We have studied the photo-fragmentation of the HBC cation, $C_{42}H_{18}{}^{+}$, as the prototypical example of an astrophysically relevant large PAH. Applying 532 nm photolysis, the main fragmentation channels of HBC cations are found for low laser pulse energy to exhibit sequential dehydrogenation followed by C_2 (C_2H_2) loss. The present data support the idea of a top-down molecular formation scheme in space, starting from PAHs and resulting in a variety of carbon structures, possibly even including graphene (Berné & Tielens, 2012; Ekern et al., 1997).

BIBLIOGRAPHY

Allamandola, L. J., Hudgins, D. M., & Sandford, S. A. 1999, Astrophys. J. Lett., 511, L115
Allamandola, L. J., Tielens, A. G. G. M., & Barker, J. R. 1985, Astrophys. J. Lett., 290, L25
Bakes, E. L. O. & Tielens, A. G. G. M. 1994, Astrophys. J., 427, 822
Berné, O. & Tielens, A. G. G. M. 2012, Proc. Natl. Acad. Sci., 109, 401
Boissel, P., de Parseval, P., Marty, P., & Lefèvre, G. 1997, J. Chem. Phys., 106, 4973
Bregman, J. D. & Temi, P. 2001, Astrophys. J., 554, 126
Cami, J. & Cox, N. L. J., eds. 2014, IAU Symposium, Vol. 297, The Diffuse Interstellar Bands
Campbell, E. E. B. & Levine, R. D. 2000, Annu. Rev. Phys. Chem., 51, 65
Candian, A. 2014, et al. (in preparation).
Cherchneff, I. 2011, EAS Publications Series, 46, 177
Cioslowski, J., Liu, G., Martinov, M., Piskorz, P., & Moncrieff, D. 1996, J. Am. Chem. Soc., 118, 5261
D'Hendecourt, L. B., Leger, A., Olofsson, G., & Schmidt, W. 1986, Astron. Astrophys., 170, 91
Dunbar, R. 2000, Int. J. Mass Spectrom., 200, 571
Dunbar, R. & Lifshitz, C. 1991, J. Chem. Phys., 94, 3542
Ekern, S., Marshall, A., Szczepanski, J., & Vala, M. 1998, J. Phys. Chem. A, 102, 3498
Ekern, S. P., Marshall, A. G., Szczepanski, J., & Vala, M. 1997, Astrophys. J. Lett., 488, L39
Frenklach, M. & Feigelson, E. D. 1989, Astrophys. J., 341, 372
Gotkis, Y., Oleinikova, M., Naor, M., & Lifshitz, C. 1993, J. Phys. Chem., 97, 12282
Gulyuz, K., Stedwell, C. N., Wang, D., & Polfer, N. C. 2011, Rev. Sci. Instrum., 82
Hendel, W., Khan, Z., & Schmidt, W. 1986, Tetrahedron, 42, 1127
Joblin, C. 2003, in SF2A-2003: Semaine de l'Astrophysique Francaise, ed. F. Combes, D. Barret, T. Contini, & L. Pagani, 175
Jochims, H. W., Baumgartel, H., & Leach, S. 1999, Astrophys. J., 512, 500
Jochims, H. W., Ruhl, E., Baumgartel, H., Tobita, S., & Leach, S. 1994, Astrophys. J., 420, 307
Jones, R. O. 1999, J. Chem. Phys., 110, 5189
Klots, C. E. 1989, J. Chem. Phys., 90, 4470
Kokkin, D., Troy, T., Nakajima, M., et al. 2008, Astrophys. J. Lett., 681, L49
Le Page, V., Snow, T. P., & Bierbaum, V. M. 2001, Astrophys. J. Suppl. Ser., 132, 233
Le Page, V., Snow, T. P., & Bierbaum, V. M. 2003, Astrophys. J., 584, 316
Leger, A. & Puget, J. L. 1984, Astron. Astrophys., 137, L5
Lifshitz, C. 1997, Int. Rev. Phys. Chem., 16, 113
Lifshitz, C. 2000, Int. J. Mass Spectrom., 200, 423
Ling, Y., Gotkis, Y., & Lifshitz, C. 1995, Eur. J. Mass, 1, 41
Malloci, G., Joblin, C., & Mulas, G. 2007, Astronom. and Astrophys, 462, 627
Rolland, D., Specht, A. A., Blades, M. W., & Hepburn, J. W. 2003, Chem. Phys. Lett., 373, 292
Rouillé, G., Steglich, M., Huisken, F., Henning, T., & Müllen, K. 2009, J. Chem. Phys., 131
Sassin, N. A., Everhart, S. C., Cline, J. I., & Ervin, K. M. 2008, J. Chem. Phys., 128
Seifert, G., Vietze, K., & Schmidt, R. 1996, J. Phys. B, 29, 5183
Sellgren, K. 1984, Astrophys. J., 277, 623
Steglich, M., Bouwman, J., Huisken, F., & Henning, T. 2011, Astrophys. J., 742, 2
Tielens, A. 2008, Ann. Rev. Astron. Astrophys., 46, 289
Tielens, A. G. G. M. 2005, The Physics and Chemistry of the Interstellar Medium (UK: Cambridge University Press)
Tielens, A. G. G. M. 2013, Rev. Mod. Phys., 85, 1021
Van-Oanh, N.-T., Désesquelles, P., Douin, S., & Bréchignac, P. 2006, J. Phys. Chem. A, 110, 5592

SAMENVATTING

INLEIDING

De ruimte tussen de sterren, het zogenaamde InterStellaire Medium (ISM), is inhomogeen gevuld met gas (99%) en stof (1%). Er zijn plekken in deze ruimte die een dusdanig hoge dichtheid hebben dat zichtbaar licht hier niet doorheen kan komen. Zulke plekken noemen astronomen daarom ook 'donkere wolken'. Deze moleculaire wolken kunnen zeer koud zijn, 10 tot 20 (Kelvin) graden boven het absolute nulpunt (-263 tot -253 graden Celsius). De dichtheden in zulke wolken zijn in verhouding tot de dichtheden van lucht op Aarde nog steeds extreem laag, ze verschillen 14 tot 15 ordes van grootte (een één met wel 14 of 15 nullen erachter). Op Aarde (bij zeeniveau) is de typische dichtheid: 2.7×10^{19} cm^{-3}, terwijl in een donkere wolk in het ISM dichtheden worden aangetroffen van 10^4-10^5 cm^{-3}. Door deze extreem lage dichtheid is de kans dat twee deeltjes elkaar tegenkomen in de gasfase erg klein; een atoom of molecuul botst typisch een keer per twee weken met een ander deeltje. Daardoor is de kans dat twee deeltjes chemisch reageren, wanneer ze met elkaar botsen minimaal, omdat er meestal geen derde deeltje in de buurt is om overgebleven reactie-energie weg te nemen. Op Aarde vinden zulke reacties wel plaats, door de hoge dichtheden. De gasfase chemie in het ISM is daardoor beperkt. Toch weten we dat er in de ruimte veel verschillende chemische reacties moeten plaatsvinden, omdat er een groot aantal verschillende moleculen is waargenomen met radio telescopen en andere waarneemfaciliteiten. Het ligt dus voor de hand dat er processen zijn waarbij moleculen effectief worden gevormd. En dat is niet iets wat a priori verwacht mag worden.

Allereerst zijn moleculen onderhevig aan bestraling van fotonen uit het interstellair stralingsveld. Sommige van de fotonen van dit stralingsveld dragen dusdanig veel energie dat ze moleculen effectief uit elkaar kunnen laten vallen. De randen van de donkere wolken beschermen de dieper naar binnen gelegen delen tegen dit sterke stralingsveld. Dit zou een verklaring kunnen zijn, waarom in donkere wolken moleculen kunnen overleven. Echter overal in het ISM, zelfs binnenin de donkere wolken is er kosmische straling. Kosmische straling bestaat uit (geladen) deeltjes en fotonen die zich met hoge snelheid door de ruimte bewegen. Deze straling kan een wisselwerking aangaan met materie, waaruit secondaire deeltjes zoals electronen of fotonen kunnen ontstaan, die op hun beurt wisselwerken met moleculen in de omgeving, hetgeen kan leiden tot fragmentatie van die deeltjes.

Ook het aantal elementen dat in voldoende abundantie ter beschikking staat voor chemische reacties is in het interstellaire medium beperkt. Vooral waterstof en helium zijn voorhanden, terwijl andere elementen, zoals koolstof (C), zuurstof (O), stikstof (N) en zwavel (S) niet veel voor lijken te komen. Met name deze laatste elementen zijn interessant, omdat dit de onderdelen zijn waaruit de moleculaire bouwstenen van het leven, water, suikers, vetten en aminozuren zijn opgebouwd.

Donkere wolken kunnen later in hun levenscyclus ineenstorten onder hun eigen zwaartekracht, hetgeen uiteindelijk kan resulteren in de geboorte van een nieuwe ster. Op deze manier is onze zon ook ontstaan. De overblijfselen van de donkere wolk bevinden zich daarna in een schijf die om deze ster aanwezig is. In deze schijf kunnen planeten zoals de Aarde zich vormen, en mogelijk is dit ook het moment dat onder andere water en aminozuren op een planeet terecht komen. Mocht deze planeet zich dan ook nog in de bewoonbare

zone bevinden, op de afstand van de ster waarbij vloeibaar water kan bestaan, dan zijn in principe alle ingrediënten aanwezig voor het ontstaan van leven. De vraag blijft echter, hoe moleculen, biologisch relevante species in het bijzonder, kunnen ontstaan.

COMPLEXE MOLECULEN IN DE RUIMTE

Ondanks de extreme condities en suboptimale verhoudingen van de elementen, vinden astronomen ieder jaar weer nieuwe complexe moleculen in de ruimte. Op het moment van schrijven zijn dit er al meer dan 185, en de verwachting is dat dit aantal door de jaren heen verder stijgt[1]. Gasfase chemie alleen, kan de waargenomen hoeveelheden van veel van deze moleculen niet verklaren. Het is gebleken dat het stof in het ISM een essentiële rol speelt. De stofdeeltjes zijn niet groter dan een tiende micrometer, en bestaan uit silicaten, oxides en koolstofrijk materiaal. Het stof is even koud als de omgeving waarin het zich bevindt, zo'n 10 tot 20 graden boven het absolute nulpunt in donkere wolken. Doordat het stof zo'n extreem lage temperatuur heeft, kunnen atomen of moleculen die ertegenaan botsen, blijven plakken. Er ontstaan ijslaagjes op deze stofdeeltjes. Zo'n ijzig stofdeeltje vormt een reservoir van moleculen waardoor de kans dat deeltjes elkaar tegenkomen veel groter wordt. Bovendien kan energie die vrijkomt bij een reactie worden geabsorbeerd, waardoor het ijs ook een catalytische werking heeft. Daarbij kunnen reacties in gang gezet worden door de inslag van atomen of electronen, door fotonen of kosmische straling.

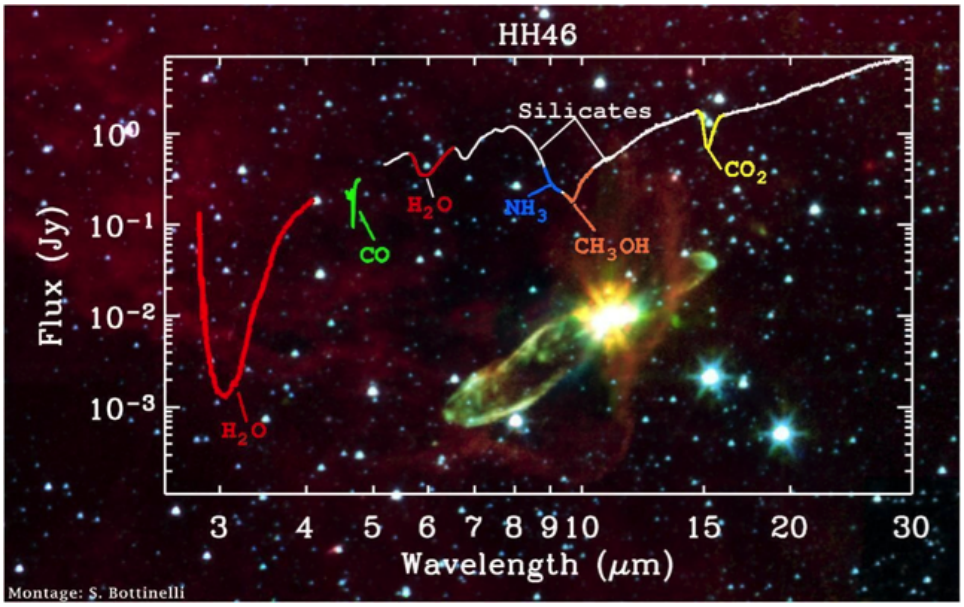

Figuur 1: Infrarood spectrum van HH46, een jonge ster. De absorptiebanden van de verschillende ijscomponenten zijn duidelijk te zien. Op de achtergrond is de Spitzer infrarode opname van deze ster afgebeeld, figuur van S. Bottinelli.

Met behulp van ruimtetelescopen zijn verschillende moleculen waargenomen in het interstellaire ijs. Infrarood observatie's (figuur 1) laten zien dat het ijs met name bestaat uit water (H_2O), methanol (CH_3OH), koolmonoxide (CO), kooldioxide (CO_2) en ammoniak

1 https://en.wikipedia.org/wiki/List_of_interstellar_and_circumstellar_molecules

(NH_3). De brede en ongestructureerde spectra zijn typisch voor moleculen vastgevroren in een ijs; in de gasfase zouden ze meer bewegingsvrijheid hebben en zouden de spectra er anders uit zien.

COMPLEXE MOLECULEN IN HET LABORATORIUM

De processen die plaatsvinden op en in interstellair ijs, kunnen worden nagebootst in experimentele opstellingen in laboratoria. Een van deze laboratoria is het Sackler Laboratorium voor Astrofysica aan de Universiteit Leiden. Een gedeelte van de experimentele opstellingen hier aanwezig, is gewijd aan het bestuderen van interstellaire ijsanalogen onder volledig gecontroleerde omstandigheden. Met behulp van turbomoleculaire pompen worden vacuümkamers ontdaan van lucht, ze worden dusdanig leeg gemaakt dat de kamers tot een van de leegste plekken in Nederland behoren. Nog steeds zijn de dichtheden die dan in de opstelling worden bereikt 1000 maal hoger dan wat wordt aangetroffen in de donkere wolken in de ruimte. Een cryostaat (een speciale koelkast gevuld met helium) koelt een gouden substraat in de vacuümkamer af tot een temperatuur van 10 tot 20 graden boven het absolute nulpunt. Op gecontroleerde wijze wordt vervolgens daarop een laag ijs aangegroeid. Dit ijs kan daarna worden blootgesteld aan fotonen of atomen, vergelijkbaar met de processen die plaatsvinden in donkere wolken. Ondertussen wordt het ijs bestudeerd met infrarood spectroscopie, eventuele reactieproducten die het ijs verlaten kunnen gedetecteerd worden met massaspectrometrie. Naderhand wordt het substraat met daarop het ijs gecontroleerd opgewarmd. Dit leidt ertoe dat het ijs langzaam verdampt. Nieuw gevormde reactieproducten kunnen op dat moment gedetecteerd worden met een massaspectrometer. Op deze manier is het mogelijk om in het laboratorium te achterhalen welke moleculen kunnen ontstaan in interstellair ijs, evenals hoe dat in zijn werk gaat. Dit resulteert in reactienetwerken en geeft ook aan hoe effectief de verschillende reacties zijn.

DIT PROEFSCHRIFT

Zoals de titel al beschrijft, ligt het zwaartepunt van dit proefschrift op het bestuderen van de interactie van licht met interstellaire materie. Om dit doel te verwezenlijken, is een nieuwe experimentele opstelling ontworpen en gebouwd in het Sackler Laboratorium voor Astrofysica. Een foto van de opstelling is te zien in figuur 2, deze opstelling is in detail beschreven in hoofdstuk 2.

Deze opstelling, genaamd MATRI^{2}CES, wat staat voor 'Mass Analytical Tool to study Reactions in Interstellar ICES', maakt gebruik van een compleet nieuw meetprincipe voor dit onderzoeksveld, namelijk: 'laser desorption post ionization time-of-flight mass spectrometry'. De samenstelling van het ijs wordt als volgt vastgesteld: nadat het ijs is bestraald met ultraviolette (UV) fotonen wordt een laserpuls gebruikt om lokaal het substraat onder het ijs dusdanig kort te verwarmen, dat dit alleen verdampt, maar niet reageert. Het gevolg hiervan is dat er een klein gedeelte van het ijs de gasfase in gaat. Met behulp van een elektronenbron krijgen deze moleculen vervolgens een lading: ze worden geïoniseerd. Een elektrisch veld geeft daarna deze ionen een gelijke hoeveelheid energie mee. De ionen zweven vervolgens door een kamer waar geen elektrisch veld heerst en aan het einde van deze kamer bevindt zich een detector. Doordat zware ionen langer over deze afstand doen dan lichte ionen, kan de massa bepaald worden op basis van de aankomsttijd, de 'time-of-flight'. Op deze manier kan de samenstelling van het ijs in situ bepaald worden, d.w.z. zonder dat het voor een chemische analyse moet worden opgewarmd.

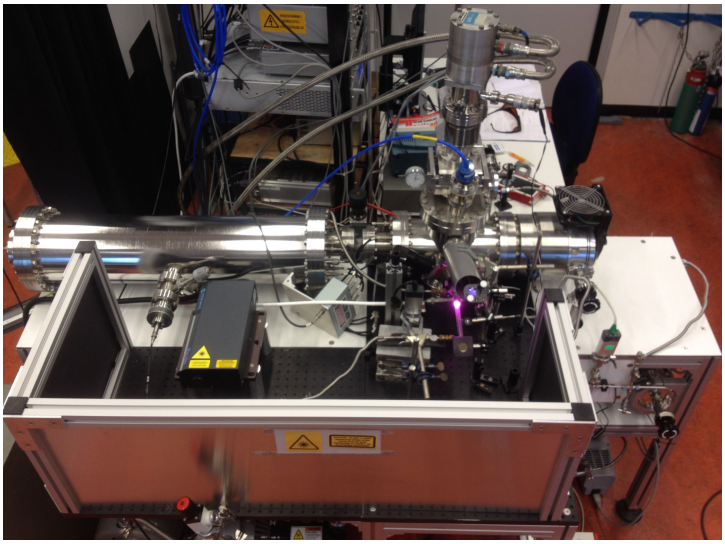

Figuur 2: Foto van de experimentele opstelling MATRI^{2}CES, wat staat voor 'Mass Analytical Tool to study Reactions in Interstellar ICES'. De opstelling is beschreven in hoofdstuk 2.

Met behulp van een speciale waterstof plasma lamp, die dezelfde kleur licht maakt als in donkere wolken, kan het ijs bestraald worden. Naast het sterke UV licht dat deze lamp produceert, maakt deze lamp ook licht in het zichtbare gebied (zie de paarse gloed in figuur 2). De intensiteit van de verschillende kleuren licht die de plasma lamp produceert hangt af van de omstandigheden waaronder deze lamp draait. Dat is dus ook de reden waarom deze lamp in detail is gekarakteriseerd in hoofdstuk 3. Het sterke licht geproduceerd door deze plasma lamp kan verschillende processen teweeg brengen in het ijs, waaronder 'fotochemie' en 'fotodesorptie'.

FOTOCHEMIE

Het uitgezonden plasmalicht is dusdanig hoog-energetisch, dat de absorptie van een foton er toe kan leiden dat een molecuul uiteenvalt in kleinere delen, zogenaamde radicalen. Deze radicalen kunnen een reactie aangaan met andere radicalen in het ijs, wat er voor kan zorgen dat er nieuwe moleculen in het ijs ontstaan. Dit gehele proces valt onder de noemer 'fotochemie'. De absorptie van fotonen kan dus op termijn leiden tot het ontstaan van nieuwe moleculen in het ijs. In hoofdstuk 2, 4 en 5 is MATRI^{2}CES gebruikt om de fotochemie van methaan-ijs (CH_4) en methanol-ijs (CH_3OH) ijs te bestuderen. Als startpunt van dit onderzoek is gekozen voor methaan-ijs. Hiervan is bekend dat de fotochemie langere koolwaterstofketens oplevert. Na een relatief korte tijd (corresponderend met een miljoen jaar in het ISM) bestraling detecteren we ionen in de massaspectra die komen van moleculen met tot wel zes koolstofatomen. Daarnaast detecteren we het ontstaan van verschillende korte koolwaterstofketens, zoals bijvoorbeeld ethaan, ethyleen en acetyleen. Gedetailleerd modelleren van de resultaten geeft inzicht in de verhouding van radicalen die gevormd worden in het ijs na de absorptie van het foton. Hieruit blijkt dat de chemie in de vaste stof heel anders is als in de gasfase en dat met name het CH_3-radicaal een belangrijke rol speelt; dit is beschreven in hoofdstuk 4.

In hoofdstuk 5 wordt de fotochemie van methanol-ijs bestudeerd. Methanol (CH_3OH) is waargenomen in interstellair ijs, en van methanol wordt verwacht dat het een startpunt is richting complexere moleculen. Onze experimenten bevestigen inderdaad een complexe fotochemie. Met behulp van onze gevoelige meetmethode hebben we de fotochemie van methanol-ijs in detail gekwantificeerd, en voor de eerste keer de vorming aangetoond van grote moleculen met tot wel zes koolstof/zuurstof atomen. Dit resultaat is belangrijk, omdat het aangeeft, dat zeer waarschijnlijk nog aanzienlijk complexere moleculen in de ruimte worden gevormd, dan tot nu toe kon worden bevestigd m.b.v. astronomische waarnemingen.

FOTODESORPTIE

Naast fotochemie kan de absorptie van een foton resulteren in 'fotodesorptie'. Het foton wordt geabsorbeerd door een molecuul en zorgt er voor dat het molecuul het ijs verlaat en de gasfase ingaat. In het ISM kan dit proces de hoeveelheden moleculen in het ijs en het gas beïnvloeden. Correcte kwantificatie van dit proces is belangrijk voor de interpretatie van waarnemingen en als invoer voor astrochemische modellen. Dit onderzoek is vooral erg belangrijk, omdat duidelijk is dat fotodesorptie mede bepalend is voor de positie van zogenaamde 'snowlines' rond jonge sterren, zeg maar de overgang van de plek waar moleculen in de gasfase voorkomen naar de plek waar ze nog in de vaste stof verkeren. Op dit moment is de fotodesorptie van koolstofmonoxide (CO) ijs een punt van discussie tussen verschillende laboratoria. Experimentele opstellingen in verschillende laboratoria, die gebruik maken van dezelfde technieken geven namelijk resultaten die tot wel een factor honderd van elkaar afwijken. Met behulp van MATRI^{2}CES, hebben we een alternatieve meettechniek ontwikkeld, om onafhankelijk de fotodesorptie van CO ijs te bestuderen. De resultaten zijn vergeleken met de literatuur, en in hoofdstuk 6 is een duidelijke richtlijn voor de implementatie van de CO-fotodesorptiewaarde gegeven, voor zowel de interpretatie van waarnemingen, als voor de invoer in astrochemische modellen.

FOTOFRAGMENTATIE

Naast processen die in het ijs door licht teweeg worden gebracht, is in hoofdstuk 7 de interactie van licht met moleculen in de gasfase bestudeerd. Dit is gedaan met behulp van een andere laboratorium opstelling. Hierbij is met name gekeken naar zeer grote aromatische koolwaterstoffen, opgebouwd uit meerdere benzeen ringen. Uit astronomische waarnemingen is bekend dat deze reeks moleculen in het ISM aanwezig is. Ze worden zeer waarschijnlijk gevormd wanneer een ster aan het eind van zijn cyclus het ISM met grote hoeveelheden materie verrijkt. Doordat deze moleculen zeer stabiel zijn, kunnen ze in het ISM overleven. In deze studie hebben we bekeken hoe een groot aromatisch koolwaterstof-ion ($C_{42}H_{18}^+$) reageert als het meerdere fotonen absorbeert. Aan de hand van massaspectra kunnen we bepalen wat de belangrijke fragmentatiekanalen zijn. Als het ion een aantal fotonen absorbeert observeren we het verlies van waterstof (2H of H_2), en wanneer het ion veel meer fotonen absorbeert zien we ook het verschijnen van het verlieskanaal met C_2/C_2H_2. Waar in de ijsstudies dus vooral wordt gekeken naar hoe grotere moleculen ontstaan door kleinere bij elkaar te voegen, gaat deze studie net van het tegenovergestelde effect uit.

LIST OF PUBLICATIONS

1. *A novel approach to measure photodesorption rates of interstellar ice analogues, the photodesorption rate of CO ice reinvestigated*
   D.M. Paardekooper, G. Fedoseev, A. Riedo and H. Linnartz
   Astron. Astrophys., submitted. (Chapter 6)

2. *Vibrational spectrum of cationic (doubly dehydrogenated) pyrene*
   P. Castellanos, J. Bouwman, A. Candian, **D.M. Paardekooper**, H. Alvaro Galué, A. Petrignani, J. Oomens, H. Linnartz and A.G.G.M. Tielens
   J. Phys. Chem. A, submitted.

3. *Laser desorption time-of-flight mass spectrometry of UV photo-processed methanol ice*
   D.M. Paardekooper, J.-B. Bossa and H. Linnartz
   Astron. Astrophys., in press. (Chapter 5)
   (DOI: http://dx.doi.org/10.1051/0004-6361/201527937)

4. *Controlling the emission profile of a MW driven H_2 discharge lamp to simulate interstellar radiation fields*
   N.F.W. Ligterink[1], **D.M. Paardekooper**[1], K.-J. Chuang, M.L. Both, G. A. Cruz-Diaz, J.H. van Helden and H. Linnartz
   Astron. Astrophys., 584 (2015) A56. (Chapter 3)

5. *Laboratory photo-chemistry of PAHs: ionization versus fragmentation*
   J. Zhen, P. Castellanos, **D.M. Paardekooper**, N. Ligterink, H. Linnartz, L. Nahon, C. Joblin and A.G.G.M. Tielens
   Astrophys. J. Lett., 804, (2015) L7.

6. *Methane ice photochemistry and kinetic study using laser desorption time-of-flight mass spectrometry at 20 K*
   J.-B. Bossa, **D.M. Paardekooper**, K. Isokoski and H. Linnartz
   Phys. Chem. Chem. Phys., 17, (2015) 17346. (Chapter 4)

7. *Laser desorption time-of-flight mass spectrometry of UV photo-processed ices*
   D.M. Paardekooper, J.-B. Bossa, K. Isokoski and H. Linnartz
   Rev. Sci. Instrum., 85, (2014) 104501. (Chapter 2)

8. *Laboratory formation of fullerenes from PAHs: Top-down interstellar chemistry*
   J. Zhen, P. Castellanos, **D.M. Paardekooper**, H. Linnartz and A.G.G.M.Tielens
   Astrophys. J., 797, (2014) L30.

9. *Quadrupole ion trap/time-of-flight photo-fragmentation spectrometry of the hexa-peri-hexabenzocoronene (HBC) cation*
   J. Zhen, **D.M. Paardekooper**, A. Candian, H. Linnartz and A.G.G.M. Tielens
   Chem. Phys. Lett., 592, (2014) 211-216. (Chapter 7)

10. *Porosity measurements of interstellar ice mixtures using optical laser interference and extended effective medium approximations*
    J.-B. Bossa, K. Isokoski, **D.M. Paardekooper**, M. Bonnin, E. P. van der Linden, T. Triemstra, S. Cazaux, A. G. G. M. Tielens and H. Linnartz
    Astron. Astrophys., 561, (2014) A136.

1 *Both authors contributed equally to this work*

11. *UV spectral filtering by surface structured multilayer mirrors*
Q. Huang, **D.M. Paardekooper**, E. Zoethout, V.V. Medvedev, R. van de Kruijs, J. Bosgra, E. Louis and F. Bijkerk
Opt. Lett., 39, (2014) 118.

12. *Real-time optical spectroscopy of VUV irradiated pyrene:H_2O interstellar ice*
J. Bouwman, **D.M. Paardekooper**, H. Linnartz and L.J. Allamandola
Astrophys. J., 700, (2009) 56-62.

ABOUT THE AUTHOR

Born on the 26th of November 1986 in Schiedam, Daniël moved together with his parents to Leiden, just 10 weeks old. He spent most of his youth in the area around this beautiful city. After receiving his high school diploma from the 'Bonaventura College' in Leiden, he pursued to study Applied Physics at the Technische Hogeschool Rijswijk. In 2008 he obtained his Bachelor degree, graduating with excellence (cum laude), on a thesis entitled 'pyrene in water ice, a laboratory study'. This project was performed in the Sackler Laboratory for Astrophysics at Leiden University. After spending half a year abroad, exploring Japan, Australia and New Zealand, he continued his studies at Utrecht University. In 2011, he graduated and obtained his M.Sc. in Nanomaterials: Chemistry and Physics. Subsequently, he accepted a PhD position in the Sackler Laboratory for Astrophysics returning back to Leiden, under supervision of Prof. dr. H.V.J. Linnartz. The research project focused on developing a novel technique to extend the knowledge of processes occurring in interstellar ice analogues. The results of the work performed during this PhD research project are presented in this thesis. In his free time, Daniël enjoys travelling, playing basketball and running. Over the timeframe of the work leading to the present thesis, he successfully completed three 1/2 marathons and one full marathon.

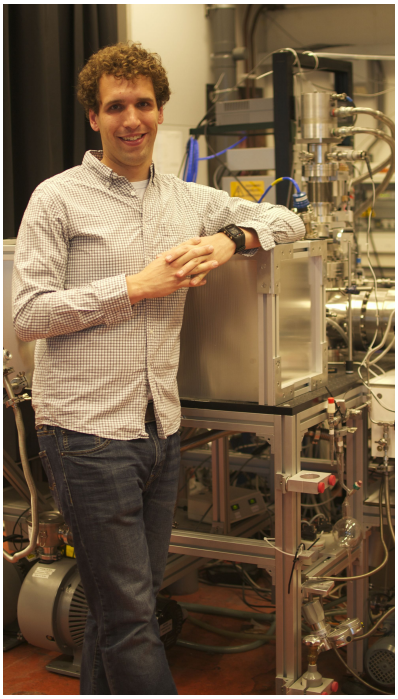

ACKNOWLEDGEMENT

A bit more than four years ago, I accepted a PhD-position in the Sackler Laboratory for Astrophysics, in the group led by Harold Linnartz. Although the decision to pursue a doctorate degree was well-considered, it turned out to be a period with many extremes. Looking back on my time as a PhD-student, I can definitely say that it has led to personal growth in various aspects. The following quote nicely summarises the various phases encountered by a PhD-student:

> *Being a graduate student is like becoming all of the Seven Dwarves. In the beginning you're Dopey and Bashful. In the middle, you are usually sick (Sneezy), tired (Sleepy), and irritable (Grumpy). But at the end, they call you Doc, and then you're Happy.*
> -Ronald Azuma

Although my name is on the cover of this thesis, it would not have been completed without the support of many people, here in Leiden. First of all, I would like to thank the support staff (Evelijn, Yvonne, Anita, Jeanne, Liesbeth and Debbie) and the guys from the computer group (Eric, David and Aart). Problems are quickly resolved, creating an ideal environment to explore, perform research, and for science to happen. HL504 has been a fantastic office during my time in Leiden, thanks for the perfect mix of quiet and animated, Joseph, Maria, Dongfeng, Sierk and Alan! Alan, thank you for all stimulating discussions we have had, and for sharing your knowledge of youtube-music, in particular the multi-hour whale sound-scape.

Redesigning a complete experimental set-up in the laboratory, is not a task which you can do by yourself. Karoliina and Jean-Baptiste, you both have had an important role in the initial period of my research, thank you both for your involvement. I have learned a lot about time-of-flight mass spectrometry and this has initiated the updated design. Without the help of the Fine Mechanical Department (FMD) and the Electronics Department (ELD), the redesign of the system would not have been possible. In particular, I would like to thank Peter, Raymond and Martijn. Martijn, bedankt voor je humor en betrokkenheid met de groep en opstelling, en voor de ontelbare keren dat ik met je mee heb kunnen rijden van Amsterdam naar Leiden!

I would like to thank the members of the Sackler laboratory: Joseph, Karoliina, Anton, Dongfeng, Edith, Thanja, Gleb, Steven, Gustavo, Hèctor, JB, Kirsten, Ko-Ju, Pablo, Vincent, Junfeng, Niels, Martijn, Aart, Euan, Andreas, Xavier, Cornelia, Aart and Martijn. Without these people, the lab and Leiden would have been a different place. Thank you for your involvement, scientific discussions and nice atmosphere. Aart, thanks for making the lab a cleaner and safer place! Andreas, thank you for your involvement with MATRI^{2}CES, I am convinced you will take good care of the system. The students throughout the years: Ellen, Thomas, Julia, Coen, Miriam, Jeroen, Patrick, Marin, Alba and Dieudonné; thank you for your questions and curiosity.

As a physicist trying to increase my understanding of astrochemistry, I would like to thank the members of the Astrochem group, in particular Catherine, Maria, Alan, Merel, Mikhel, Magnus have been always nearby for easy questions or detailed discussions. Sergio, thanks for showing me around at Caltech! I always enjoyed our discussions whenever we met each other on meetings. Heather, Emanuele, Christian, the observatory would have been a way to quiet place without you.

During my PhD-research, I've had the pleasure to go to several facilities, in Nijmegen, Paris and Greifswald. Beamtime runs are both special and intense, and would not have

been the same without you guys: Niels, Martijn, Junfeng, Pablo and Jordy, thanks! Jordy, goed om je regelmatig gezien te hebben de afgelopen vier jaar, bedankt voor je gezelligheid en je advies omtrent mijn onderzoek en toekomst.

Arianne en José, de LappTop cursus organiseren was altijd super gezellig, bedankt hiervoor!

Daan, onze loop/fiets/auto/bus lunches zal ik nooit vergeten, bedankt voor je luisterend oor en je advies omtrent mijn onderzoek. Bedankt voor het ontwerpen van de cover, hij is super geworden!

The Crew; Ashgard, Gerdien, Jelle, Daan, Thanja, Vincent, Caroline en Nikki. We zien elkaar steeds onregelmatiger doordat we ons over meer landen aan het verspreiden zijn. Bedankt voor jullie steun en afleiding tijdens de gezellige etentjes als we elkaar zien.

Twee avonden per week en op zaterdag heb ik met veel plezier doorgebracht bij LUSV. Lekker basketballen met heren 2&1 (en Klaas), bedankt dat ik met jullie deze avonden kon delen. Het was een belangrijke uitlaatklep voor mij, veel plezier gehad en energie van gekregen!

Derek en Josine, grote broer en kleine zus. Jullie zijn allebei een voorbeeld voor mij, een oase van rust in deze intense periode. Bedankt hiervoor.

Daarnaast wil ik graag mijn ouders bedanken voor hun onvoorwaardelijke steun en vertrouwen. En als allerlaatste Nikki, lieverd; bedankt voor je geduld. Zonder jou had dit boekje er nooit gelegen, bedankt dat je ervoor zorgde dat ik met beide benen op de grond bleef, en niet vergat waar alles uiteindelijk om draait.

Daniel Paardekooper